EVALUATION OF ZINC OXIDE: GALLIUM FOR HIGH-SPEED THERMOGRAPHIC PHOSPHORESCENCE DURING IMPACT STUDIES

by

Patrick Moore

A Thesis

Submitted to the Faculty of Purdue University

In Partial Fulfillment of the Requirements for the degree of

Master of Science in Mechanical Engineering

School of Mechanical Engineering

West Lafayette, Indiana

May 2021

THE PURDUE UNIVERSITY GRADUATE SCHOOL
STATEMENT OF COMMITTEE APPROVAL

Dr. Terrence Meyer, Co-Chair

School of Mechanical Engineering

Dr. Steven Son, Co-Chair

School of Mechanical Engineering

Dr. Christopher Goldenstein

School of Mechanical Engineering

Approved by:

Dr. Nicole L. Key

ACKNOWLEDGEMENTS

This research would not have been possible without the assistance of several people. First, I would like to thank my advisors, Dr. Terrence Meyer and Dr. Steve Son, whose professional and constant feedback was helpful towards research progress. I would also like to thank Dr. Christopher Goldenstein for serving on my committee. During this process, I also found that my colleagues in Zucrow Laboratories would provide valuable assistance whenever needed in the lab, especially Alex Brown and Zach Ayers. Lastly, none of this would have been possible without funding from the Air Force Office of Scientific Research (AFOSR) and Task 10.

TABLE OF CONTENTS

LIST OF TABLES

LIST OF FIGURES

ABSTRACT

Thermographic phosphors are useful compounds to determine temperature, due to their luminescence characteristics being a function of temperature. In this research, Zinc Oxide: Gallium was evaluated for its ability to measure the temperature of an impact event in a drop weight apparatus. Different solids loadings of the phosphor were placed in a sylgard binder and these samples were then excited by a 355 nm laser as they were impacted. Images of the event were captured through two separate filters with a high-speed camera, from which intensity ratios were formed. These intensity ratios correlated to a temperature, revealing the change in temperature of the sample throughout the impact. Initial testing at a repetition rate of 500 kHz provided insignificant data, due to difficulties with timing. The whole impact event was not able to be captured, and the imprecise timing of the drop did not allow for imaging of a specific area of the impact. Moving to a slower repetition rate of 50 kHz, the entire impact was captured on the high-speed camera, showing three separate areas of interest. The first section of this area was where the impact was first initiated, resulting in a temperature increase. Next, there was a temperature decrease, where the energy from the drop weight transitioned to deforming, rather than heating the sample. Lastly, there was a final temperature rise when the sample was fully compressed, but the impact was still occurring. This trend presented itself in all of the samples, supporting the idea that when combined with the intensity ratio method, ZnO:Ga embedded in a sylgard binder is an appropriate method to determine the temperature changes in a high-speed impact event.

1. INTRODUCTION

Results of an impact event can present in various ways, but often the result is some type of heat release. The degree to which an object is heated depends on a variety of factors within the impact itself, but it is always of interest to measure the degree of heating. Many different methods and devices have been used to create impacts and measure the associated heat release. In this section, prior research will be discussed involving adiabatic shear banding from impact. Within this prior research, the methods used to create the impact and extrapolate the temperature will be introduced and discussed. Additionally, the challenges of such research will be presented, along with ways to potentially address such problems. Finally, the current objectives and research approach taken in this paper will be developed.

1.1 Adiabatic Shear Banding

While adiabatic shear banding was not of interest in this current research, it was the topic of focus for the past research that inspired the approach in this paper. In his research, Yizhou Nie was investigating temperature changes during metallic deformation [1]. To do this, a Split Hopkinson (Kolsky) Bar was used to create a localized shear deformation in a material. From this deformation, a temperature reading was produced through the use of thermographic phosphors. All samples were coated with a thin layer of $BaMgAl_{10}O_{17}:Eu^{2+}$ (BAM:Eu) that was 7 microns thick [1]. During the impact from the Kolsky Bar, a 355 nm burst from Q-switched Nd:YAG burst-mode laser at 100 kHz was used to excite the BAM:Eu. Due to this phosphor experiencing a known emission spectrum shift, the temperature was able to be extracted from high-speed camera imaging using the intensity ratio method. This method takes advantage of the intensity ratio change of the phosphor emission from two separate emission bands. Different phosphors require different filters to isolate the most sensitive emission bands and, in this case, 400+/-25 nm and 450+/-5 nm were the two bandwidths chosen from which to obtain the intensity ratio [1]. With this method, the intensity ratio was able to be correlated back to temperature, but initial correlations were lower than expected for adiabatic shear banding. During the tests, the phosphor coating either chipped off or the thermal conductivity of the phosphor did not allow for the external surface of the sample to reach the same temperature as the metal [1]. Using transient heat conduction, a corrected

temperature was able to be produced. While this was the best method of determining the temperature of the surface for this experiment, ideally a temperature would be able to be drawn directly from the thermographic phosphor. Based on further investigation, it was determined that a thinner phosphor layer was necessary to be able to determine actual temperatures from the phosphor intensity ratio method. Once again, using the transient heat conduction equation, Figure 1.1 was produced, showing the temperature change over time for different phosphor layer thicknesses.

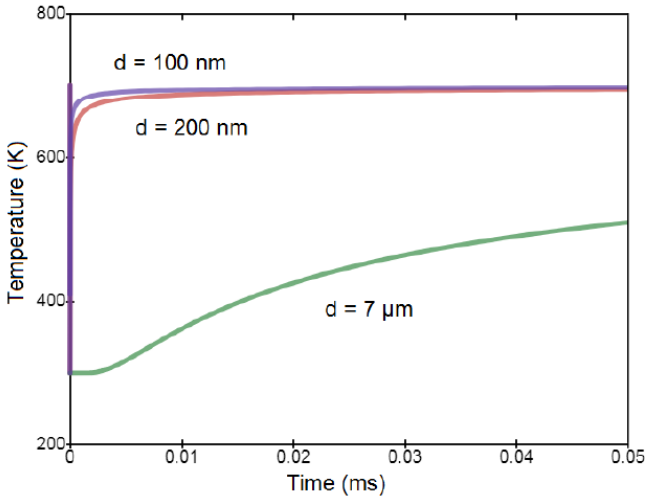

Figure 1.1 Temperature change with time on the outside of a BAM:Eu phosphor layer for different layer thicknesses with an inside surface temperature of 700 K [1]

From this figure, it was determined that a layer coating thickness of 200 nm or thinner showed much less temporal delay for the temperature measurement than a 7 micron thick coating. Therefore, the use of nanophosphors was suggested to develop a thinner coating thus improving temperature measurement from the phosphor layer. With the basis of this research described, the specific details of the individual parts will now be discussed, starting with thermographic phosphors, then moving into nanophosphors, and finishing with different impact devices.

1.2 Thermographic Phosphors

In general, thermographic phosphors (from now on referred to as phosphors) are often inorganic compounds, usually ceramic materials, called hosts, doped with rare-earth or transition

metals, called luminescent centers or activators [2-5]. The doping concentration is usually kept low, around 1%, to ensure activator atoms are isolated from each other in the host matrix. Since these activators absorb and emit radiation, their concentration can influence decay time and spectral properties of the material [3, 4]. These phosphors are useful because when excited by some type of light source, often a pulsed laser, they emit temperature-dependent luminescence. Pulsed or continuous lasers are frequently used because phosphors exhibit a broadband absorption in the UV region. When excited, electrons in the material jump to higher electron states and this absorbed energy must also be released. During the return to ground state, the temperature dependence of the phosphor stems from the non-radiative energy transfer process being a function of temperature [3, 5]. As temperature increases, the energy that is absorbed has a higher probability of non-radiative transitions when returning to the ground state. In relation to this idea, the activator concentration is normally kept low because when it gets too high, de-excitation can also occur by non-radiative means to a neighboring dopant ion because they are not isolated from each other [5]. This behavior would quench the emission of the phosphor even more, making it important to keep the dopant concentration low. Regardless of the activator concentration, non-radiative processes cause the luminescent intensity of the excited ions to decrease in most phosphors, as temperature increases [4]. Due to the fact that their luminescence is temperature dependent, phosphors can be used for semi-invasive surface thermometry, enabling remote temperature diagnostics with a high sensitivity and accuracy. One negative aspect of detecting a temperature in this way is the necessity of the phosphor to be bonded to the surface of a material. If the phosphor possesses sufficient heat capacity and thermal conductivity, then it could possibly alter the thermal behavior of the material, decreasing the accuracy of the temperature reading [4]. However, to obtain accurate temperatures from their luminescence, the response of phosphors require calibration against some type of known temperature standard, which is usually a thermocouple [2, 5]. Each thermographic phosphor has a specific range of temperature sensitivity, therefore, it is important to check that the specific phosphor employed in an experiment is sensitive over the desired range of temperatures. The main two methods that take advantage of a phosphor's temperature dependence are the time-resolved (lifetime) method and the time-integrated (intensity ratio) method [2-5].

Phosphors used to take advantage of the lifetime method exhibit a luminescence whose lifetime depends on the rate of non-radiative energy transfer [2, 4]. At higher temperatures, non-radiative decay rate increases, thus the lifetime of the phosphor decreases. This behavior tends to

exhibit an exponential relationship, which in the most basic cases is a single exponential and can be fit to Equation 1 [2, 3]. Within this equation, I is the current luminescent intensity, I_o is the initial luminescent intensity, t is time, and τ is the time constant, which is determined by the time it takes for the luminescence to decrease to 1/e of the initial luminescence.

$$I = I_o \exp\left(-\frac{t}{\tau}\right) \tag{1}$$

Using the above exponential decay relationship between non-radiative transitions and temperature, a phosphor's lifetime can be correlated back to a temperature. The only constraint on this process is that the persistence of luminescence must be longer than the length of the pulse used to excite the phosphor [5]. If this criteria is not met, then the lifetime method cannot be used due to inability to measure decay. One benefit of the lifetime method is that it generally tends to be more accurate than the ratio method when determining temperature with the exception of zinc oxide phosphors [3]. Additionally, there are more phosphors to choose from to fit a desired temperature range. Figure 1.2 shows the decay in luminescent lifetime as temperature increases for different thermographic phosphors.

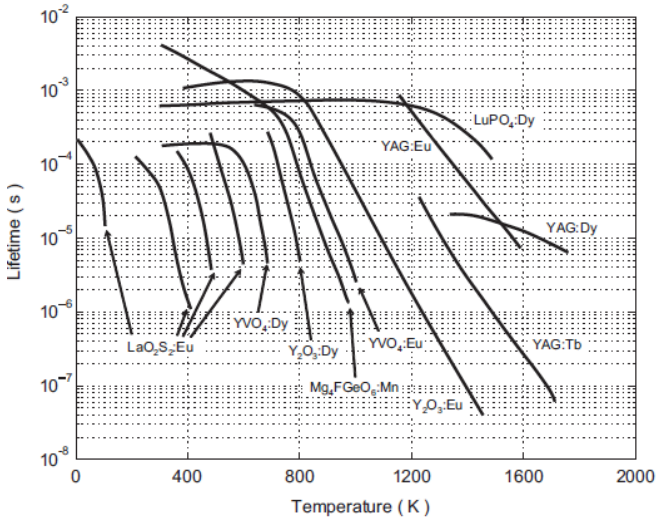

Figure 1.2 Lifetime decay of a variety of thermographic phosphors [2]

Other than lifetime, the intensity ratio method is the other way to take advantage of the temperature dependence of thermographic phosphors. This method utilizes a temperature-

dependent spectral shift of a phosphor's luminescent emission bands based on the knowledge that certain emission bands tend to become weaker with temperature [5]. However, this requires a more in-depth calibration process because the absolute intensity collected can depend on factors like excitation energy, homogeneity of the phosphor layer, and quality of alignment [2, 3]. These factors are minimized or eliminated through the division of one emission band by another. Emission bands are isolated with the implementation of different filters centered on a specific wavelength. When the intensity is collected for two or more emission bands they are divided by one another, resulting in the formation of an intensity ratio. Ideally, one of the emission lines collected is insensitive to temperature, while the other exhibits a temperature dependence [4]. Phosphors able to capitalize on this method are fewer in number than the lifetime method, but they also cover a much larger temperature sensitivity range than phosphors used for lifetime.

An example of the intensity ratio method being used can be found in Abram's research [6]. In this paper, BAM:Eu phosphor particles were seeded into a gas flow for measurements of the gas temperature. While in the flow, a laser sheet produced by the third harmonic (355 nm) of an Nd:YAG laser at 3 kHz was used to excite the phosphor. Subsequent luminescent emission from the phosphor was isolated by two filters, centered at 466 nm and 420 nm [6]. Using these two emission lines, a ratio was then determined from which temperature was correlated. A thermocouple was used to calibrate the ratio response. From this method, a maximum deviation of the mean measured temperatures, using the phosphor, to the flow temperature of the thermocouple was 5 K [6]. Based on this outcome, the precision of the intensity ratio method was demonstrated.

1.2.1 Zinc Oxide: Gallium (ZnO:Ga)

While the specific reasons ZnO:Ga was chosen for this experimental setup will be expanded upon later, its general behavior and use will be discussed below. When excited by 355 nm, ZnO:Ga produces an emission peak at 386 nm when at room temperature [3, 7]. It also exhibits a short lifetime of below 2 ns, making its lifetime too short to be useful for the lifetime methos. However, ZnO:Ga experiences a strong spectral sensitivity to temperature, as demonstrated through its decrease in signal strength with temperature [7]. These decreases in signal strength can be capitalized on by the intensity ratio method to create a high sensitivity correlation that can be related back to temperature. Figure 1.3 shows how the ZnO:Ga spectrum shifts towards longer wavelengths with temperature.

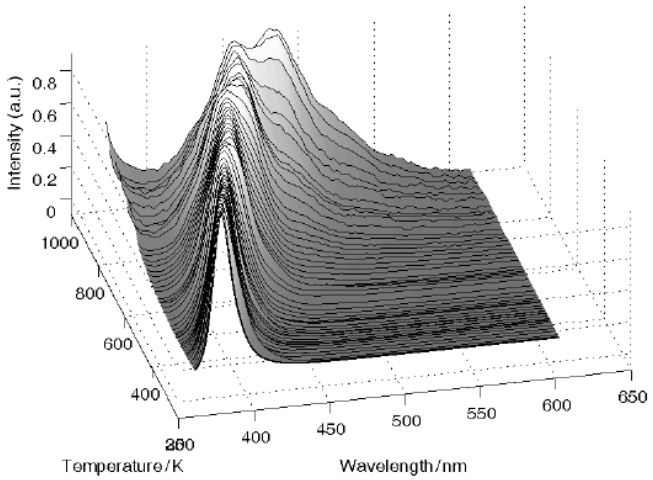

Figure 1.3 ZnO:Ga emission spectrum shift as temperature increases [7]

No matter what phosphor is used in an experiment, one of the problems mentioned above was the creation of thermal gradients from thermal conduction through the phosphor layer. Nanophosphors were mentioned as a potential solution this issue because of the ability to create a thinner phosphor layer. These types of phosphors will be discussed next.

1.3 Nanophosphors

Nanoparticles are useful materials because their size allows for high sensitivity and high spatial resolution, which is useful to determine localized temperatures. In luminescent thermometry, the luminescent particle size is the limiting factor in regards to spatial resolution [8]. Therefore, smaller particles allow for enhanced spatial resolution. Due to developments in nanoparticle synthesis, it is possible to create highly efficient nanoparticles to deploy into various systems. Among these nanoparticles, nanophosphors exists that have similar properties to their micron counterparts. As with micron phosphors, when these nanophosphors are excited, there exists a relationship between temperature and luminescence that can be exploited for temperature measurements [8]. Not only would these nanophosphors provide enhanced spatial resolution, but they have also been found to be more durable than thick films in some cases. In a study, thin film coatings were able to survive for a longer duration at elevated temperatures without a degradation in the luminescent signal [9]. Thin films were also found to have a luminescent intensity equivalent to that of thick films, meaning special instrumentation is not required to detect their luminescence

[9]. This luminescence, combined with the decreased influence of thermal conduction would allow a nanophosphor coating to produce a temperature measurement with less error. While the ability to conduct intensity ratio measurements still exists at the nanoscale, the lifetime method has been more frequently used to demonstrate phosphor potential to detect localized temperature increases, which will be expanded upon below.

Before talking about the lifetime method, and while it is not a nanophosphor itself, the Eu ion has demonstrated its usefulness in a nanothermometry system. Based on the intensity of the emission of Eu, intracellular temperature changes as small as 1 °C were able to be detected within a living cell [8]. Therefore, the intensity ratio method could be viable with Eu doped nanophosphors. However, the lifetime method has been employed on several occasions in the field of nanothermometry. In one study, YAG:Ce found application when decreased to the nanoscale. While the lifetime of its micron equivalent was temperature independent near room temperature, when deceased to the nanoscale it showed a strong temperature dependence. The micron phosphors did not demonstrate any lifetime decay until reaching temperatures of 150 °C [8, 10]. These YAG:Ce nanoparticles were around 30 nm in size and experienced a lifetime variation of around 33% from 7 °C to 77 °C, making it applicable for measurements in the room temperature range [10]. It also exhibited a lifetime on the order of tens of nanoseconds, increasing the available repetition rates used to excite the phosphor. Another nanophosphor that has exhibited usefulness in relation to the lifetime method is $ZnGa_2O_4$ doped with Cr^{3+} or Bi^{3+}. These particles were smaller than 10 nm in diameter and showed significant lifetime decay in the range of 30 °C to 200 °C [11]. A minimal change in temperature lead to a noticeable lifetime decay, demonstrating this nanophosphor's ability to be used for localized temperature measurements.

Based on the research discussed above, nanophosphors do show significant ability to be used to measure temperature, but the main problem is their availability. Most phosphors are commercially available in micron sizes and not on the order of nanometers, so these types of phosphors require synthesis. Different methods can be used to create these nanophosphors, such as co-precipitation [12, 13], combustion synthesis [14], or a sol-gel method [15]. Other methods even involve using a ball milling technique to decrease the size of a phosphor's particles [16, 17]. Regardless of the method used, all of them resulted in particles that were below 100 nm, making them effective methods of synthesis. It was also mentioned that for the sol-gel method the resulting

particles were stable with particle size remaining constant and luminescent properties not degrading with time [15].

1.4 Embedded Phosphors

Besides coating samples, another method used with phosphor temperature measurements is to insert the phosphors into a binder. In his research, Alex Casey formed a mock plastic bonded explosive sample through placing HMX crystals into a Sylgard 184 binder [18]. Within the sylgard binder, there was a 30 micron thick layer of ZnO:Ga on which the HMX crystals were placed. The sample was then covered in Sylgard 184 to complete the mock PBX sample. This type of sample was created to be able to visualize the hot spots creation from HMX crystals when exposed to ultrasonic mechanical excitation [18]. Sylgard 184 was chosen in the experiment as it did not absorb any luminescence emitted from the ZnO:Ga, allowing the use of the intensity ratio method for temperature determination. Using this setup, a temperature rise was seen in the area surrounding the HMX crystals [18]. Through this research, Casey demonstrated another form in which phosphors could be used to determine the localized temperature rise within a sample.

1.5 Impact Devices

In order to obtain a proper temperature measurement, there must first be a temperature change from which temperature can be extracted. One such way to create a temperature rise is through impacting the sample, which can be done through the use of a Split Hopkinson (Kolsky) Bar or a drop weight. Both of which are described below.

1.5.1 Kolsky Bar

A conventional Kolsky bar is used as a material characterization tool to obtain stress-strain curves of materials under high strain rates [19, 20]. Below in Figure 1.4 the conventional setup of a Kolsky bar is shown.

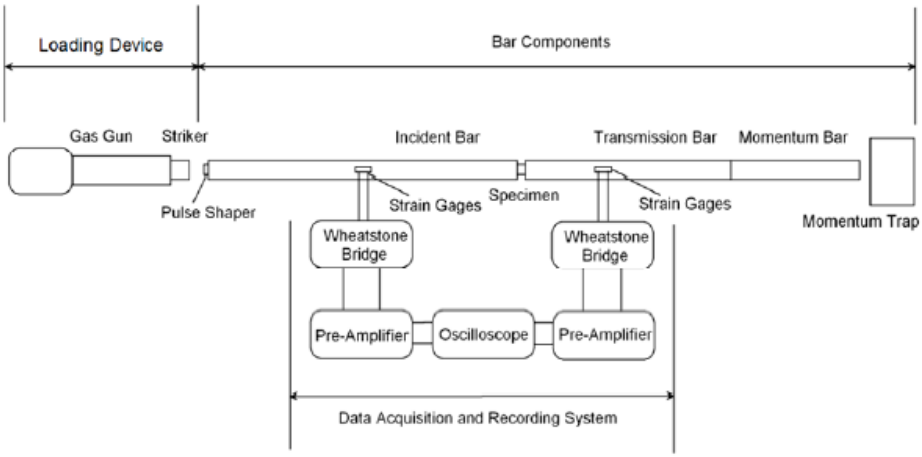

Figure 1.4 A conventional Kolsky bar apparatus containing the loading device, bar components, and data acquisition system [19]

Within this setup, three major components are shown: the loading device, the bar components, and the data acquisition system. Starting with the loading device, this must be a controllable, stable, and repeatable system that is used contact the incident bar [19]. While this system is usually dynamic, a static system can also be implemented. In a dynamic system, a striker resides in a long gun barrel and is launched into the incident bar with the striker speed being controllable. Compressed air is usually chosen to launch the striker, but anything can be used as long as it is easily controlled. Connected to the loading device are the bar components, consisting of an incident bar, transmission bar, optional extension bar, and a momentum trap [19]. Within this system, the bars are usually the same material with the same diameter, but the main requirement is that they are all straight and aligned along a common axis. In the middle of this system, the specimen is sandwiched between the incident and transmission bars. The final part of the Kolsky bar is the data acquisition system. This system begins with the strain gages attached to the surface of the incident and transmission bars [19, 20]. These strain gages are then connected to a Wheatstone bridge, which is in turn connected to an oscilloscope. Between the oscilloscope and the Wheatstone bridge, a signal amplifier can be placed to increase the signal recorded from the strain gages. With this whole system in place, the oscilloscope is able to properly record the voltage from the strain gages and thus gather information from the Kolsky bar.

When the system is fired, the striker accelerates forward and impacts the incident bar. This impact generates a stress wave, which propagates forward in the incident bar as a compression

wave (incident wave). Once this wave reaches the specimen, part of it reflects back into the incident bar (reflected wave) with the rest of it transmitting to the specimen, compressing the specimen [19, 20]. Additionally, the initial impact of the striker on the incident bar generates a compression wave in the striker itself, which reflects back and transmits a second wave into the incident bar. Once again, when this wave travels through the incident bar and reaches the specimen, part of it reflects back and the rest is transmitted to the specimen, continuing the compression. Part of the waves that are transmitted to the specimen travel through it where they reach the transmission bar. The waves that are transmitted into this bar (transmission waves) eventually terminate at the momentum trap [19, 20]. Incident and reflected waves are measured by the strain gage on the incident bar and the transmitted wave is measured by the strain gage on the transmission bar.

In general, the conventional Kolsky bar is used for metallic samples with high strength, stiffness, and wave speeds. Soft materials are less often used in Kolsky bars because of the experimental uncertainties and challenges caused by the sample's difference in material properties [19, 20]. With the low strength, stiffness, and wave speeds of soft materials the stress-strain response of the material becomes harder to collect. Low wave speeds cause problems attaining dynamic stress equilibrium and these non-equilibrium stresses cause non-uniform deformation [19, 20]. To even achieve dynamic stress equilibrium, the reflected wave must be maintained at a constant value, which is not achieved in a conventional Kolsky bar. Additionally, the low strengths cause a weaker transmitted pulse, making it harder to collect [19, 20]. Overall, the experimental results collected from the use of a conventional Kolsky bar on a soft material would be inaccurate.

Attempts have been made to address these problems and there are modifications that can be made to a conventional experimental setup to accommodate a soft material. Adjustments can be made to the specimen design, the shape of the pulse (profile of the incident pulse), and to the sensitivity of the force sensing components of the Kolsky bar [19]. To address the problem of a weak transmitted signal, the bar material itself can be changed to one that allows for more wave transmission. If that is not able to be performed, then highly sensitive strain gages can be used to detect the wave signals [20]. As for the issues concerning achieving dynamic stress equilibrium, the specimen can be made thinner to allow it to come to equilibrium faster. Otherwise, pulse shaping is required to enable the adjustment of loading rates and ensure constant strain rate

deformation [20]. When these adjustments are made the Kolsky bar can accommodate soft materials and accurate material information can be collected.

1.5.2 Drop Weight

Besides the Kolsky Bar, another apparatus that can be used for impacting a sample is a drop weight. This machine is much simpler than the Kolsky bar, as it consists of a vertically-oriented mass connected to rails. The height of the mass can be changed to alter the impact speed. At its peak position, the mass is magnetically attached to its holding device to keep it stationary. In order to impact the sample, this mass has a flat bottom, except for the area of impact. This area is circular and extruded from the rest of the bottom face. During impact, the impact area is the first and only part of the mass to contact the sample. To initiate the decent of the mass, the magnets are turned off and the mass is allowed to slide down the rails, until it reaches the bottom of the apparatus. At the bottom, the sample is waiting for impact on top of a sapphire window. This window rests on the base of the apparatus and has a designated area for its placement. When in its position, the sapphire window extends slightly above the rest of the base of the apparatus to ensure the only area of impact occurs between the sample and the mass that is sliding down. The sapphire window is necessary to allow for optical access from beneath the apparatus by both the camera and the excitation source.

1.6 Objectives and Approach

When determining the approach taken in this paper, it initially began with the idea of coating a metallic sample with nanophosphors and placing it in a Kolsky bar to measure its temperature rise when impacted. However, as previously mentioned, nanophosphors require synthesis. BAM:Eu was used to coat samples in prior experiments, so BAM:Eu nanophosphors needed to be formed [1]. There was a method for the complete synthesis of BAM:Eu nanophosphors in Sharma's research [15], however, after looking into the method it was beyond the scope of this research because it involved complete synthesis of the phosphor. Attempts were also made to use a ball mill technique as some prior research had performed, but when the phosphor was milled it was never able to reach nanometer levels. Therefore, the idea of creating nanophosphors was abandoned and samples similar to those used in Casey's work [18] were

adopted. Unlike Casey's samples where a thin plane of phosphor was used, the whole sample of sylgard had phosphor embedded in it. ZnO:Ga was also chosen as it had shown to be useful when combined with the intensity ratio method. It also had high sensitivity near room temperature, which was needed for this testing. As no energetic materials were going to be used in the samples, the temperature rise would not be drastic, so a phosphor sensitive near room temperature was ideal. Lastly, ZnO:Ga would allow for fast measurements due to its short lifetime [7]. Once the choice to swap to a sylgard sample was made, the drop weight was also chosen. This was due to the necessity of needing to alter the Kolsky bar for a softer material, like the sylgard samples. The drop weight offered a simple way to determine the feasibility of making high-speed temperature measurements during impact without the need of complete alteration to the setup.

Overall, the objective of this research was to evaluate if ZnO:Ga would be a useful thermographic phosphor for measuring the temperature of a high-speed impact when embedded in sylgard. While it had shown to be useful when inserted as a micron plane in the middle of a sample, embedding it into a binder would allow creation of samples with phosphor already included. Therefore, the rest of the sample would not need to be transparent in order to gather temperature readings and there would not be a need to insert a phosphor plane, making samples easier to create. In order to accomplish this objective, temperature measurements were to be taken of the sylgard and phosphor samples during drop weight impact. Additionally, the solids loading of phosphor in the sylgard was of interest in relation to how it impacted the ratio measurements and signal obtained from the drop weight apparatus.

2. METHODS

2.1 Embedded Phosphor Creation

In order to perform the desired high-speed impact studies, the first step was to create the embedded phosphors themselves. As a starting point, samples were made in a similar manner to those found in Casey's work [18]. In this paper, Sylgard 184 (10:1 base to curative) was used as a binder with the phosphor mixed into the binder (1:15 phosphor to sylgard by weight). Therefore, to create samples for the impact studies, a Sylgard 184 base was used in the same 10:1 base to curative ratio. Once mixed, this sylgard was placed in a vacuum chamber to remove any air bubbles. With the air bubbles removed, the ZnO:Ga was then added to the sylgard. Since solids loading was varied during these impact tests, three different sample were prepared. The initial samples contained ZnO:Ga in the same weight ratio as Casey's experiments (1:15 by weight), but the next two contained double and half that amount. Therefore, the final three samples contained 1:15, 1:30, and 1:7.5 ZnO:Ga to sylgard, by weight. These samples were referred to as normal, half, and double loading, respectively, through the duration of the testing. The ZnO:Ga added to the samples had a median particle size of 5 microns. After the phosphor addition, the samples were then cured in an oven for 24 hours. In the end, the sample thickness was around 2.7 mm. Before each test, the samples were sliced by hand into roughly 12.7 mm by 12.7 mm squares for placement into the testing apparatus.

2.2 ZnO:Ga Characterization and Filter Selection

An important aspect to the accuracy and sensitivity of thermographic phosphorescence, in relation to the ratio method, was the bandwidths chosen from which the ratio was obtained. Due to different phosphors experiencing varying spectral shifts due to temperature, specific filters must be chosen that capitalize on the current phosphor's spectral shift. In order to determine the filters that were best suited for ZnO:Ga, a normal loading sample was placed in a temperature-controlled oven. A thermocouple was also inserted into the oven and positioned near the sample to monitor the oven temperature and the temperature of the sample. This oven was optically accessible through two small windows on two different sides. One window was used to allow excitement of the phosphor sample using a laser burst and the other window was used to collect the spectrum of

the sample at different temperatures. A 355 nm beam from a Q-switched Nd:YAG burst-mode laser (QuasiModo) was used to excite the sample. In order to properly collect the spectrum of the sample an Ocean Optics spectrometer was used, which was able to record through the duration of the laser burst. Before any type of data collection occurred, a collimating and focusing lens were placed between the sample and the spectrometer. This was used to focus the spectrometer on the surface of the sample to improve the quality and intensity of the spectrum collected. Once the spectrometer was focused, data collection began. Due to the prolonged period over which the spectrometer collected data, it was able to be manually triggered just before the laser was triggered, allowing the spectrum to be recorded over the entire laser burst. After the initial sample at room temperature, the oven was allowed to slowly rise to its next temperature and stabilize before the next data point was taken. This was done to ensure the sample was heating up with the oven. Data was collected from room temperature (around 25 °C) to 300 °C. Then, once the data was collected, five different filters were artificially applied to the spectrum to determine the filter set that would provide the most sensitive ratio over the specified range. The filters applied were as follows: A (373-387 nm), B (398-504 nm), C (372-398 nm), D (415-455 nm), and E (394-406 nm).

2.3 Infrared Camera Drop

At the same time as the calibrations, but before the drop weight testing, some initial data was taken with an infrared (IR) camera. With the camera operating at 23635.07 Hz, a similar setup was used to what was going to be implemented during actual drop weight testing, however, instead of a high-speed camera, an IR camera was used. This step was useful because it helped determine what type of signal was expected from the drop weight when actual testing occurred. To emulate the testing conditions used in the future drop tests, the drop weight was placed at a height of around 0.7 meters from the sample and the IR camera was placed on a rail on the ground that had optical access to the sample through a mirror mounted in front of the camera. The mirror reflected the surface of the sample that was placed against the sapphire window. Therefore, when the drop occurred, the IR camera would have a clear image of the bottom of the sample. Beyond just the drop weight apparatus and the IR camera, this testing required a photodiode and a laser pointer. The laser pointer was directed across the center of the drop weight apparatus, just above the phosphor surface, into the photodiode. When the drop weight mass was magnetically disengaged from its peak position, it began its downward movement. At a point just before contact with the

phosphor surface, the mass cut off the signal from the laser pointer to the photodiode. Once this photodiode lost its signal, it triggered the IR camera, which then started recording. Therefore, the IR camera was able to capture the entire duration of the impact on the sample. While the speed of the IR camera was slower than what was going to be used during the actual testing, it was a useful preliminary test to determine the intensity of the impact event.

2.4 Calibration and Ratio Analysis

When the calibrations were conducted, QuasiModo was used to produce a 355 nm laser burst that would excite the sample. A similar setup was implemented as when the spectrum of the sample was collected. Samples were placed in a temperature-controlled oven with optical access through two windows on two separate sides of the oven. The laser was directed through one window, but the main difference was that, instead of a spectrometer, a high-speed camera was now used. As opposed to when the spectrometer was used, the high-speed camera required more precise synchronization with the laser. Therefore, an oscilloscope was used to find the proper delay so that the camera was triggered as the laser was firing. Once the proper delay was found for each calibration, the laser was used to trigger the camera and the camera collected images during laser excitation of the sample. Attached to the high-speed camera was a 105 mm UV lens, which was focused on the sample. An image doubler was placed in front of the lens that was capable of holding the selected filters for the tests. For each test, the oven was allowed to slowly increase to the desired temperature and stabilize. The temperature was once again monitored by a thermocouple that was placed in the oven and near the sample. Once the oven temperature began to stabilize, the data collection occurred.

2.4.1 500 kHz Calibration

For the initial phosphor calibrations, due to QuasiModo operating at 500 kHz with a 1.5 ms burst, the Shimadzu high-speed camera was used with a HiCatt intensifier attached to improve the amount of signal collected from the sample. While the Shimadzu was capable of operating at such high repetition rates, it was only able to collect 256 frames (0.512 ms) because of its storage ability. Therefore, timing was important for this aspect of the testing. With the laser set to 500 kHz with a 1.5 ms burst, it produced 750 pulses, as opposed to 256 frames collected by the camera. To

capture the best signal from the laser, the camera needed to record data somewhere in the middle of the 750 pulses. So, the camera was still triggered off of the laser, but would only begin collecting data after a certain delay. Once the camera and laser were properly timed, the laser power was taken over the entire burst to determine an estimate of the power that was going to be used during the data collection. At its initial settings, the laser power was 3.11 mJ/burst, giving it a power of around 0.00415 mJ/pulse. Over the rest of the experiments, the power settings were kept the same, but the HiCatt gain was adjusted to obtain enough signal from the samples. This way a similar power was expected for the duration of the tests. When it came to collecting the proper calibration data, even though three different samples were created, the testing began with a focus on the normal loading sample. Once data was collected for its calibration and impact, the other solids loadings would then be tested. However, data was to be collected for both of the chosen filter sets (A/D and E/D) to determine if one had a distinct advantage over the other. To achieve a proper calibration for the sample and both filter sets, data was to be taken from room temperature (25 °C) to 250 °C, every 10 °C. Despite this calibration plan, on one of the testing days the temperature-controlled oven was not functioning properly, so data was not able to be collected all the way down at room temperature. Instead, data began at 70 °C for one filter set and 25 °C for the other. At the time of the calibration, this was not an issue because the exact temperatures necessary were unknown, but if the impact exceeded 70 °C, then the calibration covered those values. It was also planned to redo this calibration all the way to room temperature, if necessary.

2.4.2 50 kHz Calibrations

After the 500 kHz tests, further research was conducted, but at slower repetition rates. To ensure the entirety of the drop was collected, 50 kHz was the new repetition rate chosen. At this rate, QuasiModo was able to burst for 10.5 ms, producing 525 pulses. Additionally, since a slower repetition rate was implemented, the Shimadzu was no longer necessary to use. Instead a Phantom v2012 was employed, which was synchronized to the laser and was able to store more than the 525 pulses from the laser. Since the Phantom had more storage potential at this repetition rate, the timing was different than what was used prior for the Shimadzu. Instead of having to time the Phantom to collect the middle of the laser burst, it was able to be triggered at the same time as the laser and could capture the entirety of the laser burst. A total of three different setups were used throughout the 50 kHz calibrations and all of them are described below.

Initially, the 50 kHz calibration had a similar structure to those conducted at 500 kHz. It consisted of the Phantom and an intensifier synchronized to the laser. The setup still included an image doubler with filters and 105 mm UV camera lens. The only difference from the 500 kHz test to this test was the addition of a focusing optic to try and minimize the presence of rings produced by the laser onto the sample. These rings were noticed before, but their influence was unknown on the 500 kHz calibrations. Therefore, to take out this potential source of error, the laser was focused onto the sample with one focusing optic. It was not so focused as to cause the surface of the sample to potentially burn, but it was focused down enough to where the rings that had been seen prior were no longer noticeable. The data collection itself was to consist of a more specific calibration from 25 °C to 120 °C, but with a data point every 5 °C. This was done as opposed to from 25 °C to 300 °C because the temperature rise was not expected to reach such high degrees. Furthermore, based on information gathered from the 500 kHz tests, data was to be collected for only one filter set (E/D), but all solids loadings for a more complete calibration. With this plan in mind, due to some preliminary analysis that occurred, only the normal and half loading samples were calibrated for the filter set. Therefore, this calibration setup led to the conduction of only two tests and the reasons for this are discussed later. The subsequent calibrations were more holistic to get a better understanding of the overall characteristics of the samples.

After the initial 50 kHz calibration talked about above, another setup was devised to reduce the number of variables that would be able to influence the calibration. To do this, the intensifier was removed and a UV fused silica diffuser (1 degree divergence angle) and an additional focusing optic was added. The intensifier was removed to minimize any test-to-test intensity variation inherent to its use. This way the only possible intensity variation would be from the camera alone, reducing the possible error. A power reading was also taken along with every shot to determine if changing power would have any influence on the samples. Due to the removal of the intensifier, the power would have to be increased to increase the signal. To track the power, a beam sampler was placed in the path of the laser that was able to split off a percentage of the laser with each test. The sampler was first tested to make sure it was able to obtain similar readings regardless of its position in the beam path. To test this, the sampler was placed at two different locations in the path, one close to where the beam began and one close to the sample. Regardless of where the sampler was located, it was able to obtain similar readings of beam power, meaning the placement of the sampler was not a vital component to its readings. Before every test, an average power

reading was taken for the part of the laser reflected into the sampler and the other that was transmitted through it. With this percentage known, the power readings from the sampled beam were recorded with every burst of the laser. Using this reading, an estimation of the power transmitted to the sample was determined. During the testing, power was only increased as needed to gain enough signal from the samples. In general, the power began around 240 mJ/burst (0.457 mJ/pulse) and was increased from that point, as needed. Additional changes included the use of a diffuser and two focusing optics to increase laser uniformity. Before, the one focusing optic seemed to create a uniform laser profile, but it the use of an addition focusing optic with a diffuser would ensure the most uniform profile. For this setup, the laser initially passed through one focusing optic, which was able to focus the laser down to a spot on the diffuser. This step was only necessary because the diffuser was slightly damaged and the focusing optic allowed for utilization of an area of the diffuser that was free of damage. Once the laser passed through the diffuser, it began to expand, requiring the use of another focusing optic that was able to concentrate the laser on the sample. With this setup, an entire calibration was conducted to test the repeatability of the ratio tests over a larger range of temperatures. The calibration included both filter sets, with all solids loadings tested for each filter set. For each test, five data points were taken every 20 °C, from room temperature (25 °C) to 300 °C. This type of calibration would give the best overall picture of the action of the samples with temperature for both filter sets, along with how repeatable each ratio was for all temperatures.

Despite the prior calibration being rather complete for the samples, after that calibration and before the drop tests, the laser underwent unscheduled maintenance, giving the laser a better profile and more signal for the same conditions used prior. Not knowing what impact this would have on the calibration, another was conducted. The exact same setup was used as in the prior calibration, but because of the information gathered during the prior calibration, the data collected during this one was able to be slightly decreased. Instead of recollecting all of the data from room temperature to 300 °C for both filter sets, the prior calibration was used to choose the more sensitive filter set (A/D) and then calibrate over the temperature that were best fit for that filter set. Therefore, five data points were collected every 20 °C, but the temperatures only spanned from room temperature to 180 °C. All three samples were still calibrated, but only for one filter set. As before, the power was collected for every data point and only increased as needed to produce enough signal. The same method, using the beam sampler, was implemented to determine the

power with each test. During this calibration the power generally began at 125 mJ/burst (0.238 mJ/pulse) and increased from that point. This test was not only performed to ensure that the temperature correlation was accurate, but it also provided some information into the importance of the laser profile and certain sample characteristics to the ratios obtained. With this calibration finished, the samples would have a proper temperature correlation when moving to the drop weight. The final calibration setup is shown below in Figure 2.1 and 2.2 with 2.1 showing the first leg of the laser path and 2.2 showing the last leg.

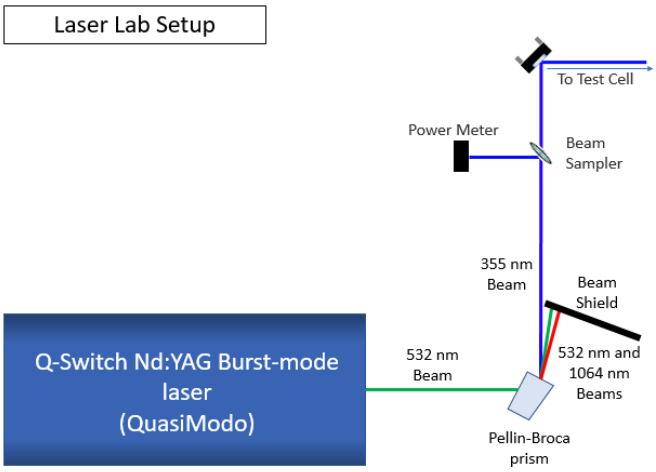

Figure 2.1 Final setup for the beginning of the laser path

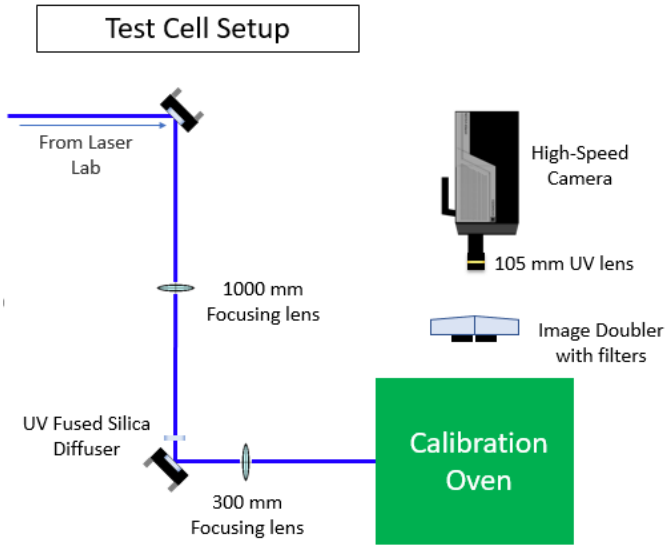

Figure 2.2 Final setup for the 50 kHz calibrations

2.4.3 Ratio Analysis

Once all of the data, both the calibrations and the drop weight tests, was collected, processing of the images was the next important step in the process. The code was made and edited during the calibration stages because that was the first data collected and then the same code was applied to the drop weight images. Due to the application of the image doubler, every frame collected in testing consisted of two images of the laser pulse as seen through the two individual filters. These images needed to be split into two parts to be able to overlap them and find the intensity ratio produced over the entire laser burst. To find the proper image translation to overlap the images, a registration image was taken before every test. This image was vital to the code because it determined the how one image would overlap onto the other. Based on the image, a function was then created for the image overlap that was applied to all the subsequent data. An example registration image, with its applied translation can be seen below in Figure 2.3.

Figure 2.3 Example registration image with the applicable overlay applied

Once the image translation was determined, that overlay was then applied to one of the laser pulse images to check the translation on an actual test. This also allowed the image to be further cropped to cut out some of the dead space located further away from the laser pulse. With the image properly overlaid and cropped, the rest of the analysis was able to be conducted. Before the left and right images were overlaid, a minimum intensity threshold was then applied to each image to get rid of any data that was in the background of the image and held no usable information. The analysis was then conducted, consisting of the application of the previously determined crop and overlay to all the images collected in each test. When the overlay occurred,

it was important to remain consistent with which filter side was divided by which because swapping this would result in a ratio that was the inverse of what was expected. After the overlay was completed, a single matrix of ratios over the laser pulse was determined for every image. With this matrix determined, further thresholds were applied to limit the data to only those pixels that contained useful ratio information. Three different thresholds were applied, a low signal threshold to eliminate any division resulting in a zero ratio, a high signal threshold to eliminate any division that resulted in infinity, and a not a number threshold to eliminate any division that resulted in NaN. After these final limitations were applied to the single matrix, the average of all the leftover ratios was taken. This resulted in an average ratio for each frame collected. This data was useful to see how the ratio changed over the laser pulse, but to obtain the final ratio for each test the average of all of the images was taken. This analysis description was the first edition of the code used with some edits being made throughout testing. The important editions and tests performed for the code analysis are described below.

An initial test performed on the code analysis was to determine what impact the minimum intensity threshold had on the final ratios. To test this, the threshold intensity was varied from zero to ten during the analysis of the 500 kHz calibration. Ten was chosen as the max because making this threshold too high would threaten to eliminate some of the useful data from the images. The results of such testing can be seen below in Figure 2.4. This figure shows how the final ratio plot changed for each threshold.

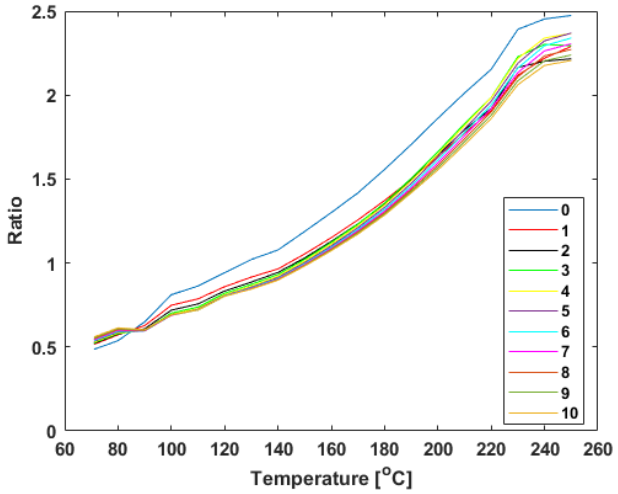

Figure 2.4 Final ratio plot for the 500 kHz calibration with the minimum intensity threshold varied

From this test, it was determined that there was little difference once the threshold was increased above zero. Therefore, a final threshold of five was applied to all tests as the center value between one and ten.

Additionally, during the analysis of the data, it was noticed that on some cases the amount of dead space around the image could alter the ratios slightly if the pixels were not properly eliminated by the prior mentioned constrains. Therefore, the cropping of the images was important to obtaining a proper final ratio. This cropping was initially attempted manually, as mentioned above, but this manual method required a rather arbitrary choice of the crop. To remedy this, a method was devised that automatically analyzed all the images in a test and cropped the image down to a spot where the laser pulse overlaps. This way the images were cropped only to where usable data was held in the image. Everything stayed the same in the analysis, but before the final image overlay and ratio determination, an additional crop was added. This part of the code searched all the images in a test and applied a contour was created around the laser profile in the left and right images. From these contours, the maximum and minimum location for the x and y pixels were determined for the entire test and those locations were used to crop the image further. Another benefit of this contour method was that any image without a clear contour was able to be eliminated and was not included in the final ratio analysis. These eliminated images were at the beginning and end of the laser burst, which was either before the laser arrived at the sample, as it was ramping up or down, or after it had finished its burst. Figure 2.5 shows an example of the additional crop with the left image being the initial manual crop and the right image showing the crop after the additional contour crop had been applied.

(a) (b)

Figure 2.5 Example of the additional contour crop used to further edit the images for analysis with (a) being the manual crop and (b) being the crop after the contour code was applied

From this addition it was seen that the application of this contour crop method performed its proper function of achieving the tightest crop possible without cutting out any useful data. With

this part of the code added and the thresholds applied, the final ratios were not going to be thrown off by any random background noise.

Once the entire analysis had been conducted for the calibrations, some larger variations in final ratio were noticed in some of the tests at the same temperature. To ensure that this was a result of the sample, rather than the analysis, the final addition to the code was to minimize these variations. This was done by applying a Gaussian filter the images to smooth out the laser intensity. The Gaussian filter was applied to the image before the contour was applied and also when the final analysis was conducted. Different intensities of the filter were tested to see which combinations would provide the best signal with the smallest standard deviation. For the tests, the initial code was run without the filter for baseline results. Then five different tests were conducted for varying intensity combinations. The results of the test are summarized in Table 2.1 below.

Table 2.1 Results from different Gaussian smoothing filters applied to the ratio analysis with the numbers representing the intensity of the filter

All	**Initial**	**Crop – 2, Ratio – 0**	**Crop – 2, Ratio – 1**	**Crop – 0, Ratio – 1**	**Crop – 0, Ratio – 2**	**Crop – 0, Ratio – 3**
Average	7.43	6.34	6.12	6.28	5.61	5.12
Range	3.45	0.94	1.10	1.58	1.01	0.88
Stand Dev	1.3092	0.3613	0.4338	0.5997	0.4008	0.3210

From the tests, it was concluded that the best combination able to maintain a high average signal for the overall ratio, but minimize the standard deviation within the data was when a filter of intensity 2 was applied to obtain the contour, but then no filter was applied when determining the actual ratio. This was potentially due to the filter making it easier for the contour to determine the location of the laser profile through its smoothing of the entire image, but the ratio remained high from the actual analysis not being filtered. Regardless, with this combination applied the analysis was able to decrease the standard deviation of the data points by close to 1. Figure 2.6 below shows the test case before and after the selected combination was applied.

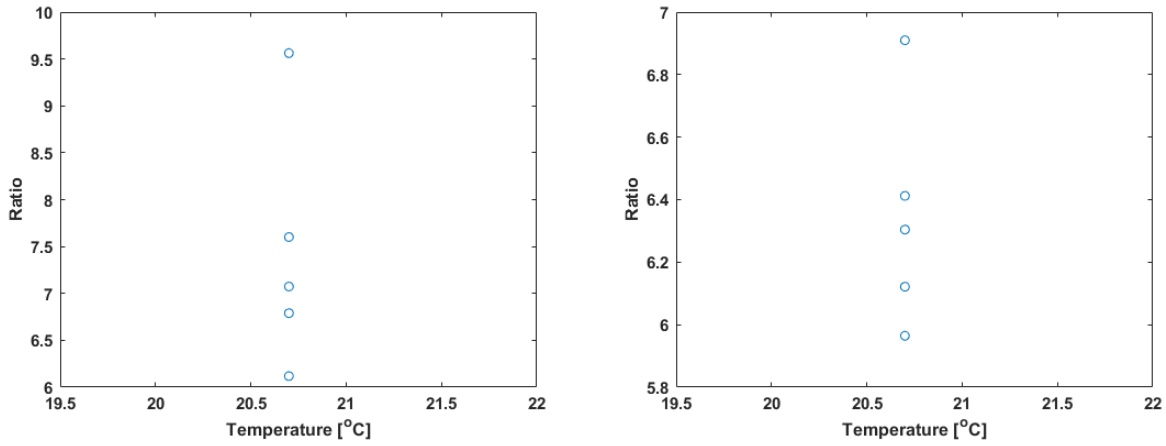

(a) (b)

Figure 2.6 Example test to show the decrease in variation between different tests at the same temperature for the double loading sample with (a) being the initial data and (b) being the data after the selected gaussian filter was applied

2.5 Drop Weight Tests

Once the drop weight testing was ready to be conducted, a similar setup was created to the test with the IR camera. For all experiments, the same general setup was used with some small changes that will be mentioned within the test in which the change was implemented. Overall, the drop weight setup consisted of the drop weight apparatus, a high-speed camera, an image doubler with filters, a laser pointer, a photodiode, an oscilloscope, and a delay generator. A 355 nm laser, produced by QuasiModo, was used to excite the samples. As with the IR camera, the high-speed camera was placed on a rail on the ground with optical access to the sample using a mirror. The camera was able to image the bottom side of the sample through a sapphire window. Attached to the high-speed camera was a 105 mm UV lens that was focused onto the sample. In front of the lens was the image doubler with the filters attached. Above the sample, the laser pointer was directed through the center of the drop weight apparatus into the photodiode. To initiate the tests, the mass was magnetically disengaged from its pinnacle location and began falling. During its fall and before contact with the sample, the mass interrupted the laser pointer's path, blocking signal to the photodiode. The loss of signal to the photodiode then triggered the oscilloscope, which was attached to the delay generator. The delay generator then triggered the laser, which was also used to trigger the camera. In the end, the laser was able to excite the sample during its impact, which was also able to be caught on the high-speed camera. Determining the proper delays to use was

the most important part of the testing setup because testing was reliant on knowing the impact was being captured. The different repetition rates required different timing as well, but that will be further discussed below. An image of the drop weight apparatus can be seen in Figure 2.7

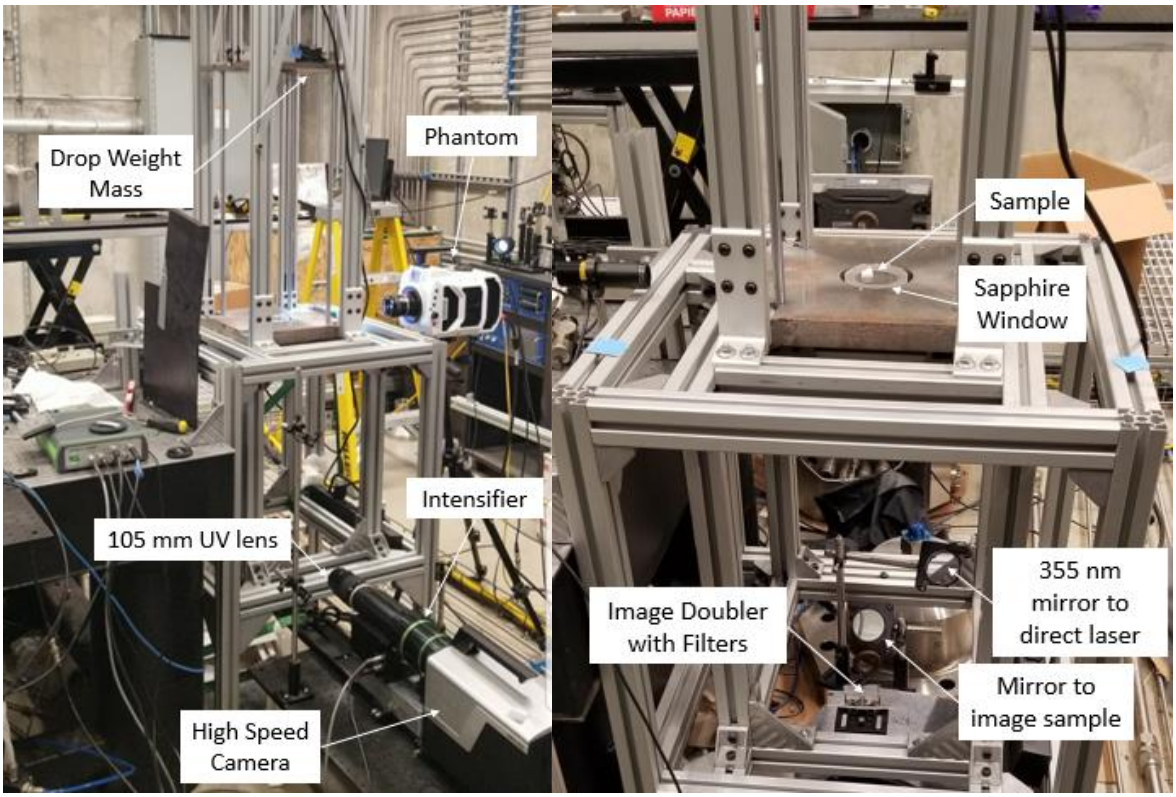

(a) (b)

Figure 2.7 (a) Drop weight apparatus set up for the 500 kHz tests (b) Under side of drop weight with the sample placed on the sapphire window

2.5.1 500 kHz Drop Weight Tests

In order to properly test at 500 kHz, some further editions to the setup described above were made. As was done with the calibration, the Shimadzu high-speed camera was used to capture the images with an intensifier attached. However, a Phantom was also used to take images of the drop weight as it fell and impacted the sample. The Phantom was not able to take images at 500 kHz, but 100 kHz was used to capture the impact event. This video was taken in order to improve the accuracy of the timing for the laser and Shimadzu. Due to the Shimadzu being able to take a short duration of data, comparison with the Phantom video helped determine which part of the impact was being imaged. Even with the Phantom taking video concurrently with the drop, the

drop weight was not always consistent in its drop timing. Therefore, when the tests occurred, the delays for the Shimadzu and the laser were slightly varied between tests to try and capture different portions of the drop. Testing happened on two different occasions with the first one consisting of 20 different tests with only the normal loading sample and the second one consisting of a total of 15 tests, five for each solids loading. The first 20 tests were performed to find the delay and filter set that offered the best readings for the tests. Therefore, both filter sets were used with a variety of delays. The second round of testing was performed for each solids loading under five different delays. Only one filter set (E/D) was chosen for the duration of this testing, based on the results of the normal loading calibration and the prior 20 drop weight tests. Even though the half and double loading samples had not yet been calibrated, these tests were done to see if one solids loading offered more signal than the others.

2.5.2 50 kHz Drop Weight Tests

When the repetition rate was reduced to 50 kHz, the setup was once again changed as was done with the 50 kHz calibration. To reduce the number of variables that could influence the results and to mimic setup used in the calibration, the intensifier was removed from the setup and the Shimadzu was replaced with a Phantom. Additionally, the second Phantom was not required, as the timing became easier at this repetition rate. The Phantom was able to capture the entire laser burst and the burst was able to excite the sample for the entire impact event. Therefore, testing different delays was not necessary, for as long as the laser and camera were triggered slightly before impact, the impact was going to be captured. The last alteration made to the drop weight setup was the addition of the diffuser and additional focusing optics. Similar to the calibration, an initial focusing lens was applied to the setup that was able to focus the laser onto a portion of the diffuser that was not damaged. After the diffuser, another focusing optic was used to refocus the laser onto the sample. However, due to some spatial limitations inherent to the drop weight apparatus, the focusing lens could not be as close to the sample as it was with the calibration. This led to a smaller final laser spot on the sample as compared to the calibration. The rest of the triggering aspects of the 50 kHz drop tests remained the same. When testing began, all solids loadings were tested with each solids loadings being put through five tests. Testing occurred on one occasion with only one filter set used (A/D), as was determined from the calibration. An initial

test was also conducted to make sure enough signal was produced, leading to a total of 16 tests. The final testing setup for the 50 kHz drop tests can be seen below in Figure 2.8.

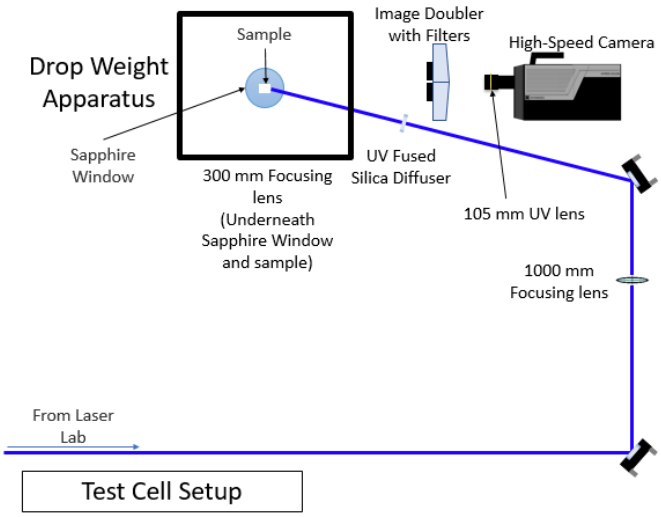

Figure 2.8 Final drop weight testing setup for the 50 kHz drop tests

3. RESULTS/DISCUSION

3.1 ZnO:Ga Characterization and Filter Selection

When the spectrum of the ZnO:Ga was collected, the intensity of the emitted wavelengths were recorded as the temperature was increased. After the first and second test, at room temperature (25 °C) and 110 °C, the laser energy was increased to obtain a greater signal on the spectrometer. However, this resulted in the tests at and above 110 °C having a larger signal than if the energy was kept the same. In order to check to see if this altered any results, two corrections of the data were made. When the data was examined, it was noticed that all the spectrums taken at the same energy converged on the right side around 420 nm. Therefore, to correct the intensity of the first two temperatures, their intensity was increased to a point where convergence was obtained at the same point as the other plots. The initial collected data can be seen in Figure 3.1 below with the corrections seen in Figure 3.2 and 3.3.

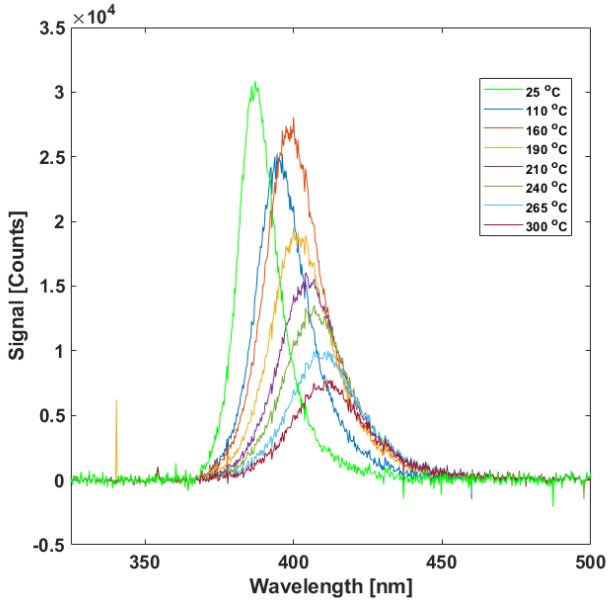

Figure 3.1 Initial intensity data collected for ZnO:Ga emission spectrum

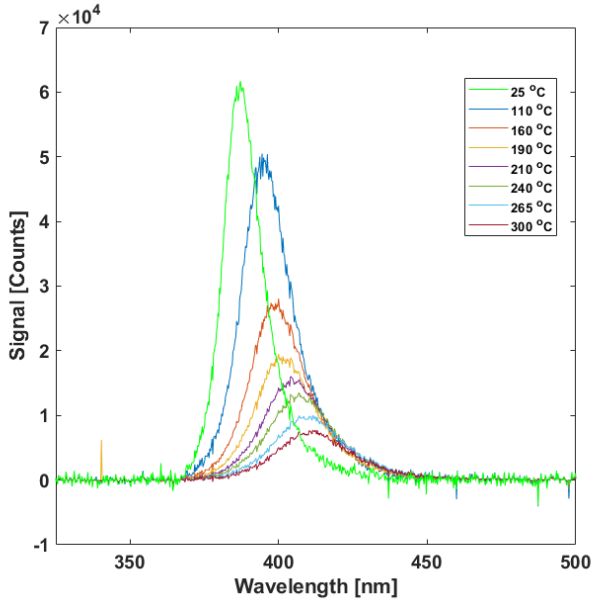

Figure 3.2 Intensity data for the ZnO:Ga spectrum with the 110 °C test corrected to converge on the right side of the spectrum

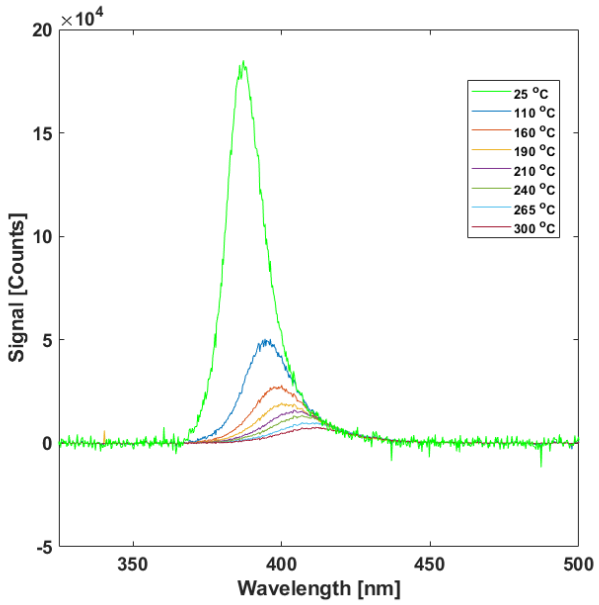

Figure 3.3 Intensity data for the ZnO:Ga spectrum with both the 25 °C and 110 °C tests corrected to converge on the right side of the spectrum

With the data from the spectrum above, different combinations for the prior filters mentioned were artificially applied to the spectrum. Then using this filter data, ideal ratios were

created for different filter combinations. The following ratios were calculated: A/D, A/B, A/E, C/B, C/D, and E/D. After testing all these different ratios, filter sets A/D and E/D were chosen because they offered a clear trend with temperature with a distinct change in the ratio present. Figure 3.4 shows filter sets A/D artificially applied to the uncorrected spectrum with the intensity ratios associated with each temperature. Figure 3.5 shows the same information as Figure 3.4, but for filter set E/D.

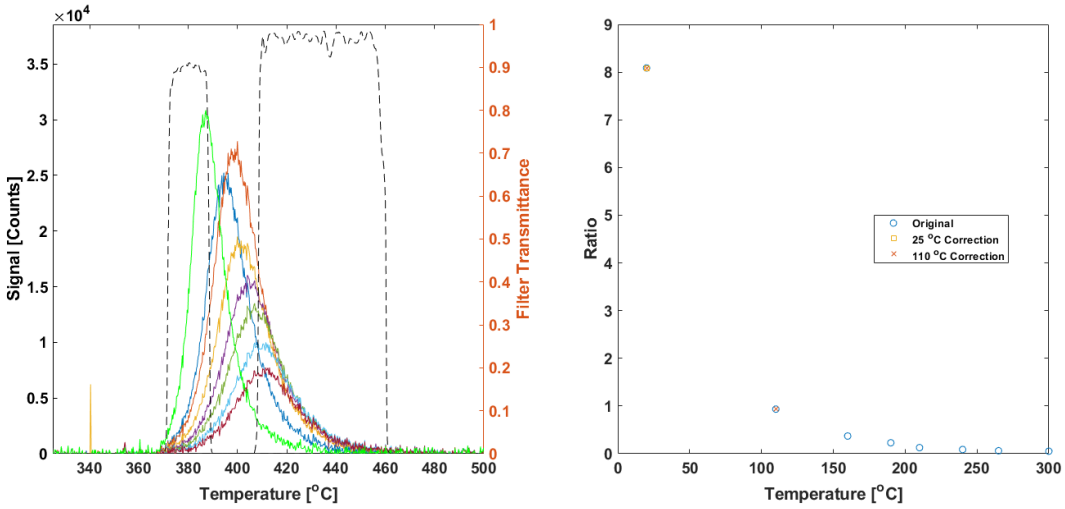

(a) (b)

Figure 3.4 Filters A/D artificially applied to the uncorrected ZnO:Ga emission spectrum in (a) and the intensity ratios exhibited by all three ZnO:Ga emission spectrums in (b)

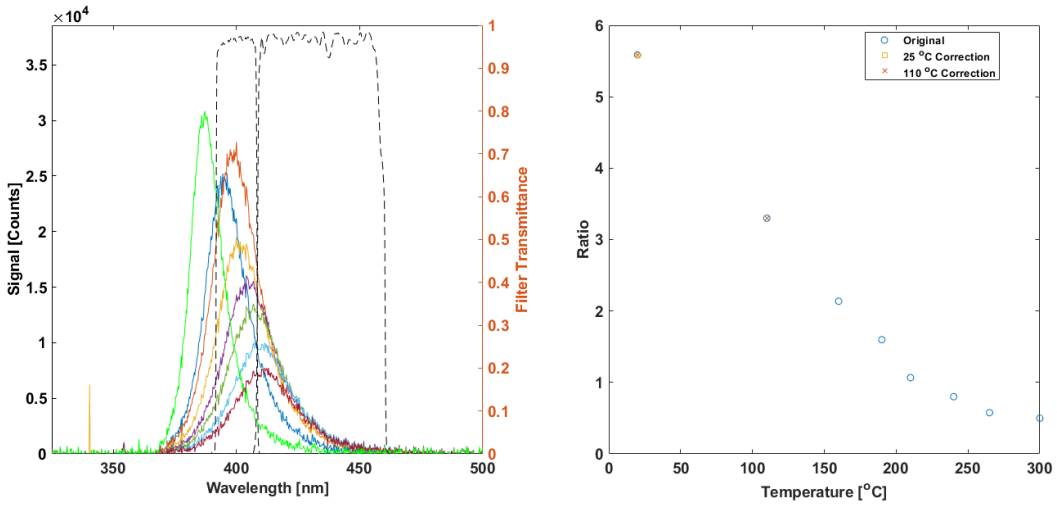

(a) (b)

Figure 3.5 Filters E/D artificially applied to the uncorrected ZnO:Ga emission spectrum in (a) and the intensity ratios exhibited by all three ZnO:Ga emission spectrums in (b)

For the A/D filter set, there was an exponential decrease from 25 °C to 200 °C with the largest ratio decrease, from 8 to 1, occurring from room temperature to 110 °C. After 200 °C, it began to level out. On the other hand, filter set E/D showed more of a linear decrease in ratio with temperature all the way to 265 °C, from a ratio of around 5.6 to 0.5. Both of these filter sets showed a sensitive ratio from room temperature to 200 °C, making them appropriate for impact tests that were not expected to reach extreme temperatures.

Even though these filters are only shown applied to one of the spectrums, they were applied to all three. When the corrections were applied, there resulted in no change to the overall ratios present. This can be seen in the ratio plots in Figures 3.4 and 3.5 because the points lie directly on top of one another. For both corrections, the ratios for both spectrums overlap at the room temperature and 110 °C case. Therefore, the ratios obtained remained unchanged, despite a change in overall intensity collected by each filter. The reason for this being that the intensity collected by each filter increased by the same ratio, not causing any alterations to the final ratio. As was stated in the introduction, the division of one emission band by the other results in the elimination of many variables that would influence the overall intensity collected, one of those variables being laser power. With the proper filters now selected, it was possible to apply these filters to the different calibrations and drop tests.

3.2 Infrared Camera Drop Test

In relation to the IR camera data, the IR counts over time were able to be collected. Time zero was in reference to when the laser signal to the photodiode above the sample was cut off, triggering the IR camera. However, due the necessity of imaging the impact through a sapphire window and a mirror, some of the IR signal was cut out, so the signal collected from the IR video was inaccurate. Regardless of the accuracy of the IR camera, this part of the experiment was performed to determine the expected behavior of the temperature during the impact of the sample, rather than to obtain a completely accurate temperature reading. The results of the IR camera drop test can be found below in Figure 3.6.

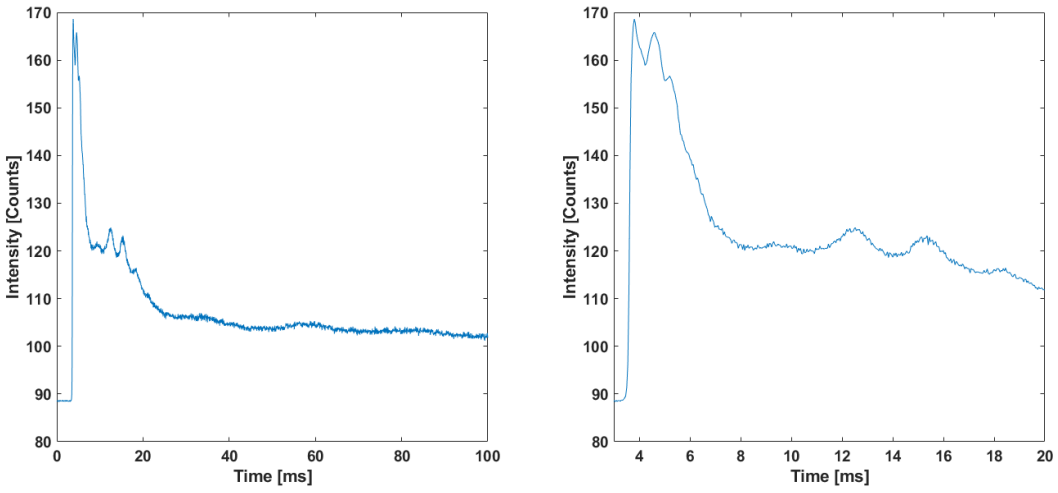

(a) (b)

Figure 3.6 IR counts collected for preliminary drops in the drop weight apparatus with (a) showing the IR intensity over the entire drop and (b) showing the first area of the drop

From this data, there was a noticeable initial temperature increase over a short time frame, around 0.5 ms. After the initial rise, there was a drop in the IR counts, signifying some slight cooling for another 0.4 ms. The last part of the data showed a final increase in the IR counts for 0.4 ms followed by a decrease in counts for the rest of the plot. Due to the temperature readings being inaccurate, the trend was focused on rather than the significance of the IR counts. Additionally, unlike the laser and high-speed camera, the IR camera was unable to capture only the IR counts of the sample and instead captured the IR counts of the whole apparatus imaged through the mirror. Therefore, both the intensity and time frame were inaccurate in reference to

the impact event of the sample. Despite these two errors in the setup, the reason for this testing was to determine if there was some degree of noticeable temperature rise that could be capitalized upon to take temperature measurements. Based on the data, there was the definitive presence of a temperature rise that could be captured from underneath the sample. The exact magnitude and time scale of such a rise within the sample was still unknown, but that was to be further investigated with the subsequent tests.

3.3 500 kHz Calibrations

Collection of calibration data for the 500 kHz samples occurred on two occasions due to the selection of the two filter sets. As mentioned before, some problems were initially experienced with the temperature-controlled oven, which occurred during the E/D calibration. Therefore, only 19 tests (one every 10 °C) were conducted from 71 °C to 250 °C. Conversely, the A/D calibration contained 23 data points (one every 10 °C) all the way from 25 °C to 250 °C. In Figure 3.7, the data for all of the fames is shown for both tests. Figure 3.8 contains the associated temperature calibration lines with a 95% confidence interval above and below the calibration line. In both figures, the left image is the data and calibration for the E/D filter set and the right image is for the A/D filter set.

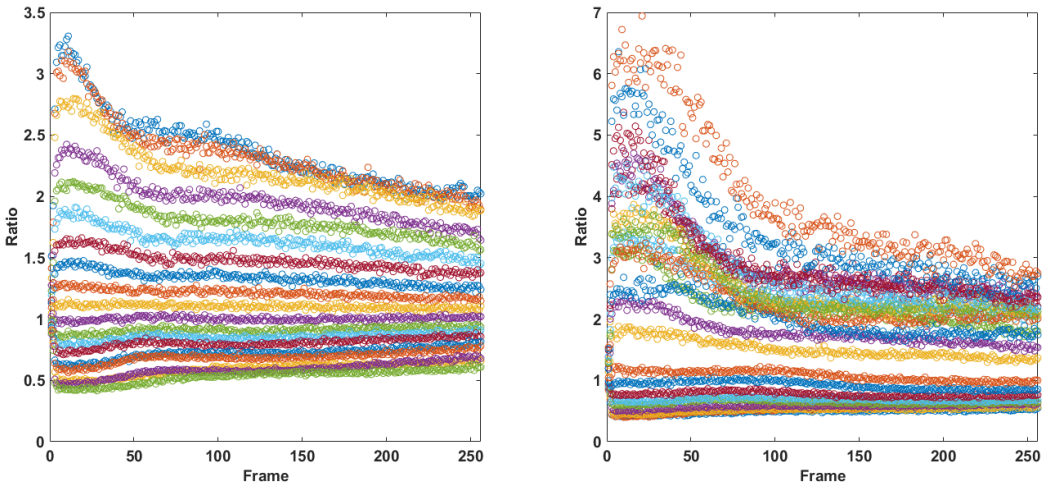

(a) (b)

Figure 3.7 500 kHz frame-by-frame ratios at each temperature for the E/D filter set in (a) and the A/D filter set in (b). Each color represents a different test

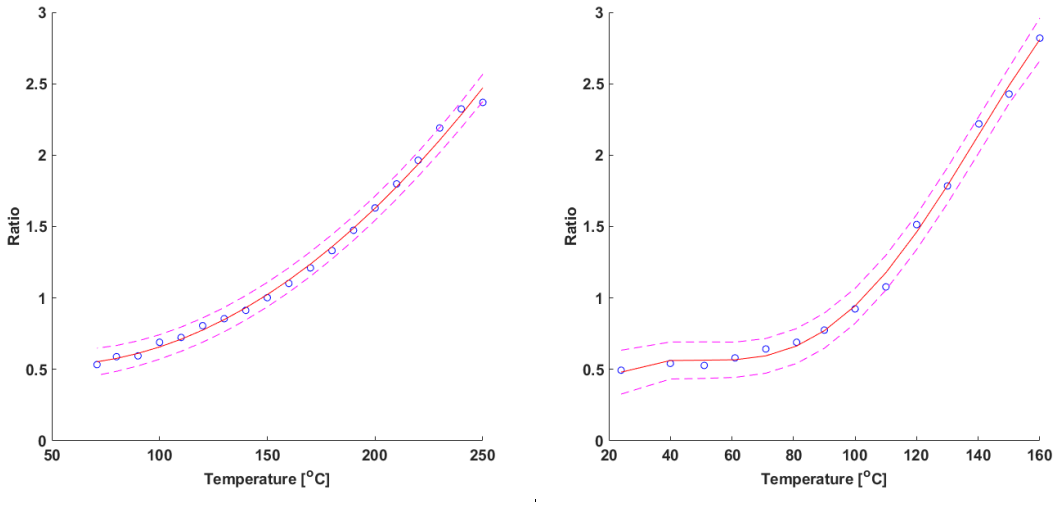

(a) (b)

Figure 3.8 Final 500 kHz temperature correlation plots with a 95% confidence interval for the E/D filter set in (a) and the A/D filter set in (b)

Both of these plots exhibited a clear trend with temperature, as expected. From 70 °C to 250 °C the E/D filter set increased from a ratio of 0.5 to 2.5 and from 25 °C to 160 °C the A/D filter set increased from 0.5 to around 2.75. They both exhibited an almost quadratic best fit line with a tight 95% confidence interval, meaning the trend had little deviation. Just as a note, the reason the plots show an opposite trend than the spectrum plots was because the ratio was taken for the D filter intensity over the A and E intensities. As discussed prior, this was not an issue as long as the same ratio was performed for the testing. An increasing ratio with temperature was consistent with the inverse of the ratios found from the spectrum. However, above 160 °C, the A/D plot completely altered its correlation, making the calibration only useful until 160 °C. Additionally, the A/D filter set remained rather horizontal until around 80 °C or 90 °C, further decreasing its useful range from there to 160 °C. Even though the E/D calibration started at 71 °C, it did not break trend at the higher temperatures and exhibited an increase in ratio over the whole range collected. For these reasons, the E/D filter set was the favored of the two calibrations, but as it did not span all the way to room temperature the A/D filter set was still tested in the drop weight.

3.4 500 kHz Drop Tests

3.4.1 Initial Testing – Normal Loading Sample

Due to much difficulty timing the camera and laser with the drop weight, the first 20 tests at 500 kHz were performed as an investigation into if the determined delay would capture a part of the impact that exhibited a noticeable ratio change and therefore change in temperature. The delay was the length of time until the camera started recording after the photodiode lost signal. Time zero was then when the camera began recording. Using the Phantom video, a delay of 7.6 ms was determined to usually capture the start of the impact event. However, the uncertainty inherent to the drop weight timing brought about some unreliability with the chosen delay. Therefore, several tests were captured at this delay and the delay was also varied to see if catching a different part of the impact was more beneficial. Even though the E/D filter set provided the better calibration, both filter sets were used to see if there was a noticeable difference between the two sets. The specifics for each test are listed in Table 3.1 below with Figure 3.9 showing the ratio change of the related test. For the figure, the top left test represents test 1 with the tests increasing sequentially moving to the right. The second line begins with test 5 and follows the same pattern.

Table 3.1 Testing Notes for the initial 500 kHz drop tests

Test	Filter Set	Notes	Test	Filter Set	Notes
1	A/D	No drop, just laser	11	E/D	No drop, just laser
2	A/D	7.6 ms delay	12	E/D	7.6 ms delay
3	A/D	7.8 ms delay	13	A/D	No drop, just laser
4	A/D	7.6 ms delay	14	A/D	Laser misfire
5	E/D	No drop, just laser	15	E/D	No drop, just laser
6	E/D	7.6 ms delay	16	E/D	7.6 ms delay
7	E/D	No drop, just laser	17	E/D	No drop, just laser
8	E/D	7.6 ms delay	18	E/D	10 ms delay
9	A/D	No drop, just laser	19	E/D	12 ms delay
10	A/D	7.6 ms delay	20	E/D	11 ms delay

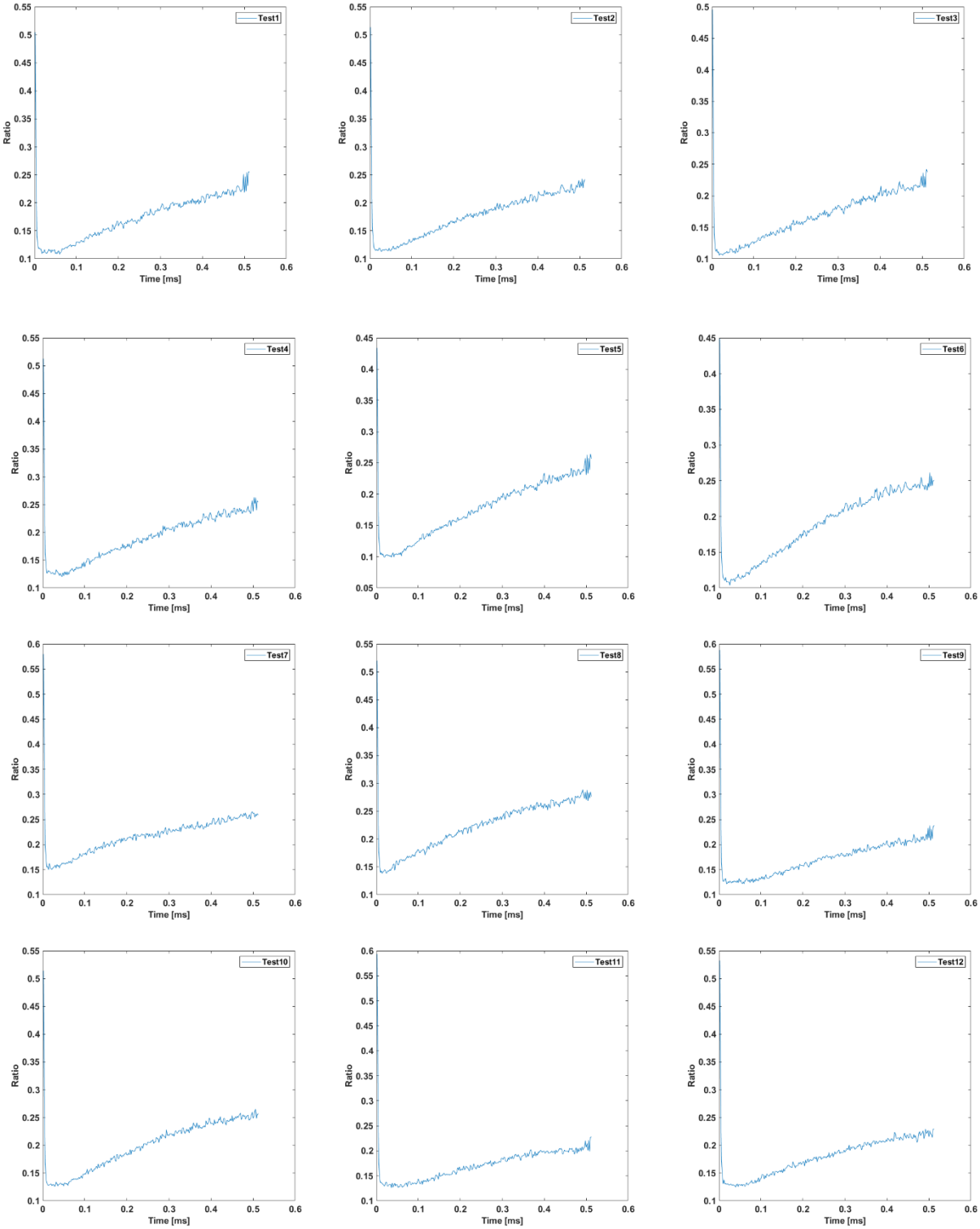

Figure 3.9 Tests 1-20 for initial drop weight testing at 500 kHz with the change in ratio over the laser burst plotted

Figure 3.9 Continued

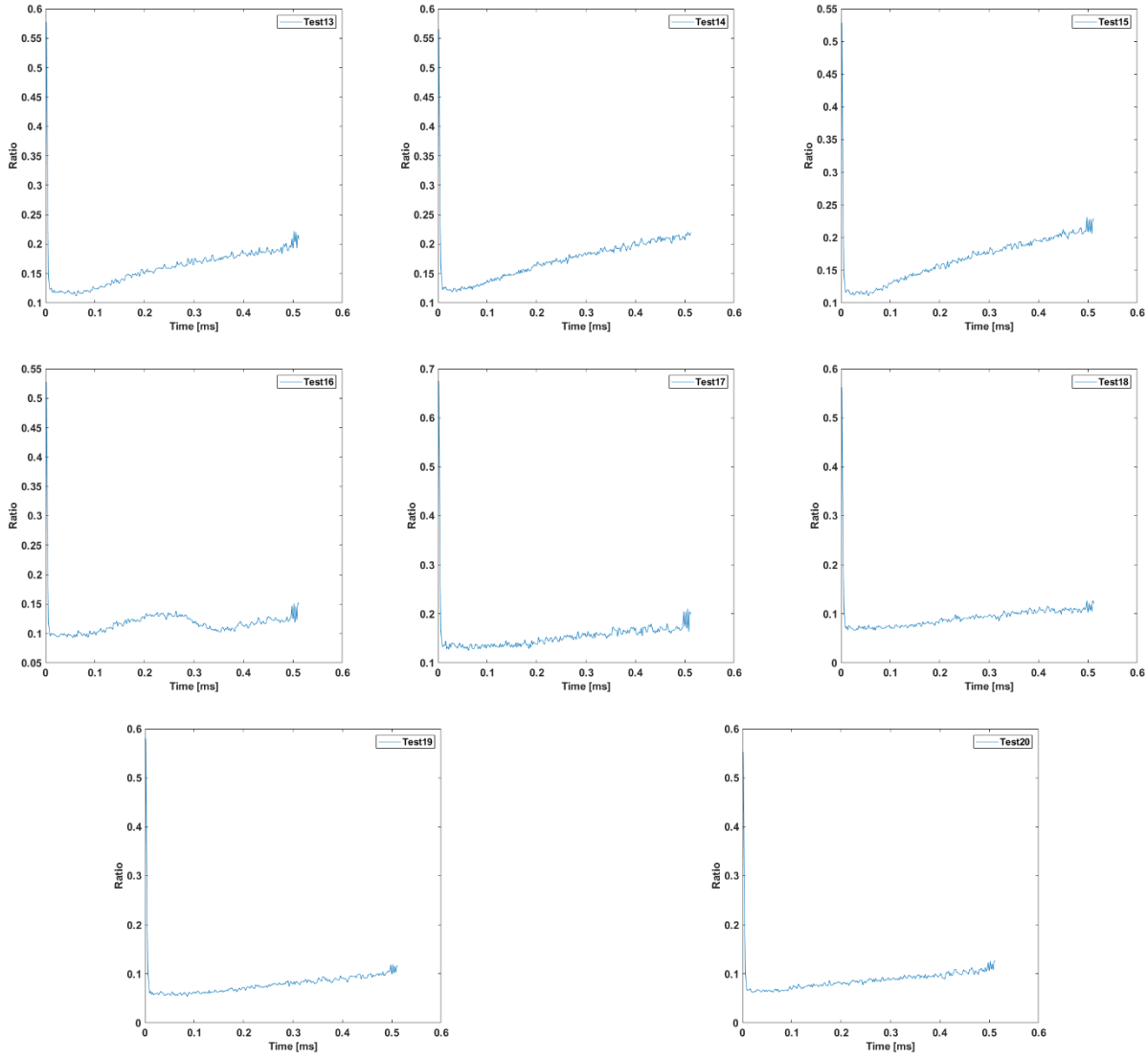

In the figure above, no one test was emphasized because none revealed anything of note for the impact. From the 20 tests, most showed the same general trend of a linear increase in ratio in the duration of the laser pulse. However, since this trend was also exhibited when no drop was involved, it was clear that this was not heating of the sample, but rather a trend inherent to the testing. Therefore, there did not seem to be any type of impact caught on the high-speed camera for a majority of the test, except for one. Test 16 was the most promising of the drop tests because it exhibited an initial ratio increase that was interrupted by a small ratio decrease and then another ratio increase, which was a similar trend to what was seen in the IR camera. However, the other tests done under the test conditions that were the same as 16 did not exhibit this type of behavior,

either showing the lack of repeatability of the setup or that test 16 was not actually capturing an impact, but some other phenomenon. Due to this increased uncertainty in the reliability of the data, no weight was placed on the information gathered from this test and the testing proceeded as was initially planned. One piece of information learned from this testing was that neither filter set showed a distinct advantage in the data collected. When choosing a set for the next drop tests, the one that provided the better calibration would be more useful when final temperature correlations needed to be determined. Since the E/D filter set showed the better calibration, this was the set used on the next drop test.

3.4.2 Final Drop Tests – All Samples

After the E/D filter set was chosen, the next drop tests involved collecting data for each solids loading. Since the prior 20 tests did not help reveal which delay was the most appropriate, the delay was once again altered over the tests. During this new round of testing the Phantom video was used to find an area further into the impact, so a delay of 11 ms was used, as opposed to 7.6 ms for the prior 20 tests. Some difference in delay was caused tearing down and setting up the triggering system between these two occasions, but mostly the later delay allowed for imaging of an impact in progress. An initial test was taken for each sample without a drop and then five other tests were taken with different delays. The initial test with no drop was used to determine the most appropriate settings for the intensifier, but it was also used to divide out the behavior of the sample without a drop. This way it would be more noticeable if any of the drop tests varied from a baseline test with no drop. Table 3.2 shows the test conditions used for each sample. From these tests Figures 3.10, 3.11, and 3.12 show the ratios collected and no drop corrected ratios for the half, normal, and double loading samples, respectively.

Table 3.2 Test conditions for the final drop tests conducted at 500 kHz for varying solids loadings

Test	Notes
Room Temp	No drop – Baseline Test
1	Delay 12.5 ms
2	Delay 11 ms
3	Delay 11.5 ms
4	Delay 12 ms
5	Delay 11.25 ms

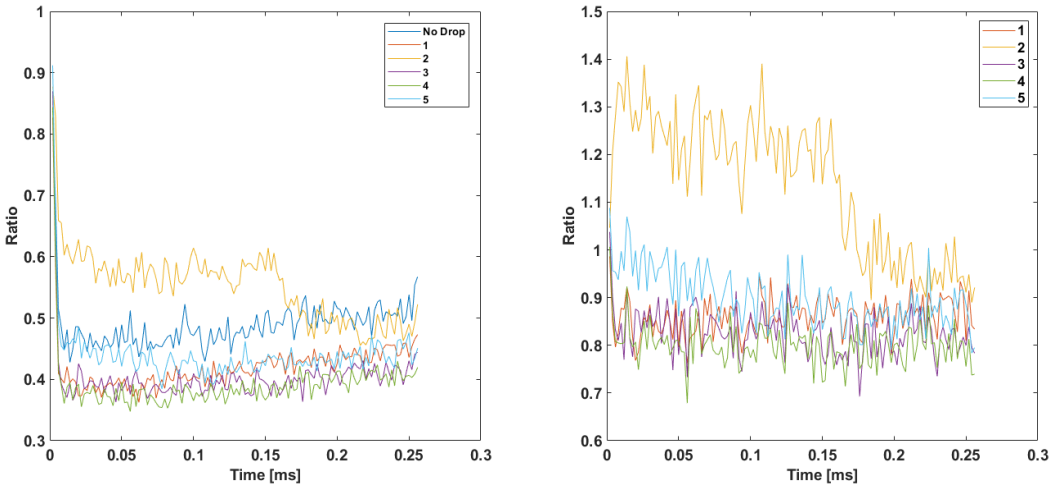

(a) (b)

Figure 3.10 Drop tests at 500 kHz for the half solids loading sample with (a) showing the absolute ratios and (b) showing the no drop corrected ratios

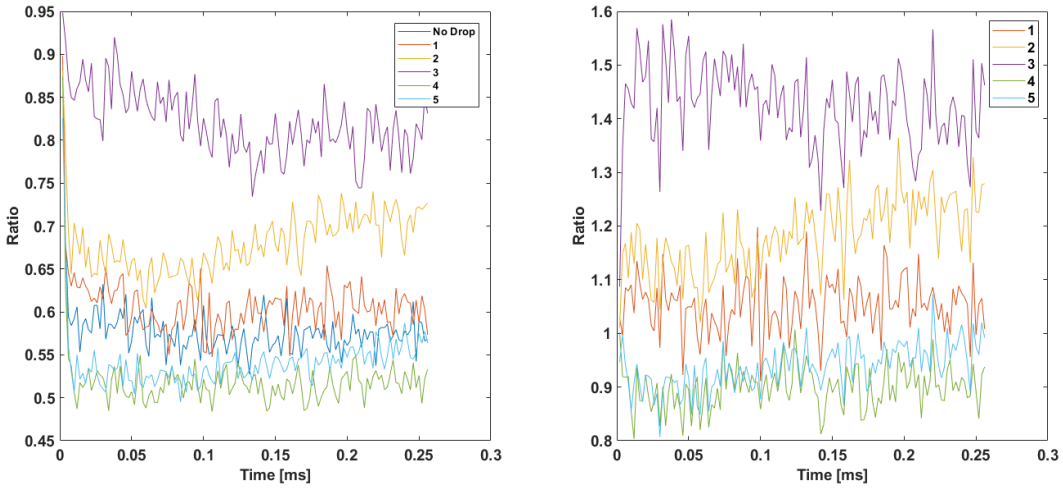

(a) (b)

Figure 3.11 Drop tests at 500 kHz for the normal solids loading sample with (a) showing the absolute ratios and (b) showing the no drop corrected ratios

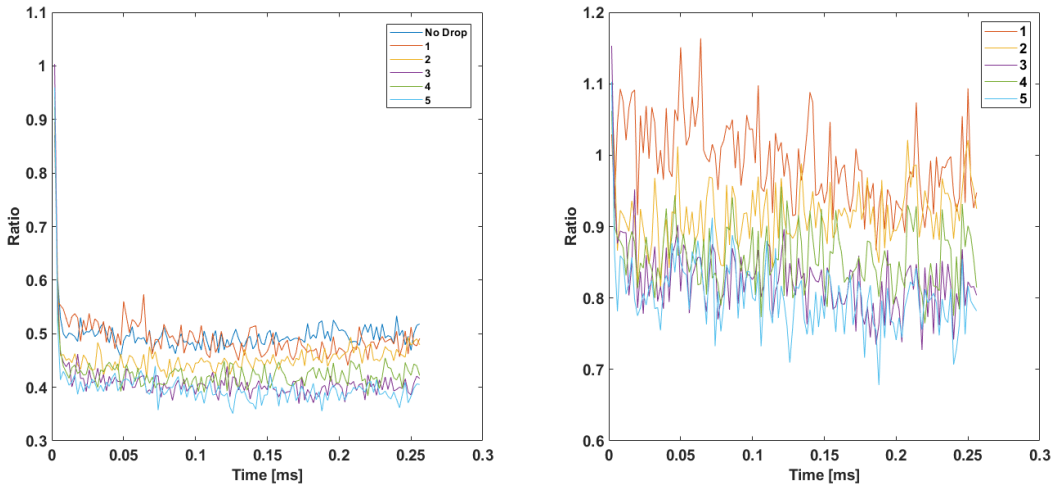

(a) (b)

Figure 3.12 Drop tests at 500 kHz for the double solids loading sample with (a) showing the absolute ratios and (b) showing the no drop corrected ratios

Based on this group of drops, a few variations were seen on some tests, but nothing distinct enough to be associated with an impact event. The half and double loading samples exhibited a ratio increase on the second test, but this presented itself just as a falling ratio in the half loading sample and a relatively horizontal ratio on the double loading sample. Additionally, the double loading sample test was only slightly raised above the others and above the no drop case. The normal loading sample exhibited a raised ratio on the third test and towards the end of the second test. This raised ratio was also relatively horizontal on the third case. In all of these tests, there was no clear increase in ratio during the test, only some tests that had elevated ratios over the others. Similarly, no two tests with the same delay for the different solids loading showed similar trends to each other. Therefore, these ratio differences could have been from capturing part of the impact event, but there was also doubt as to whether the impact was being captured. To be able to trust any temperature measurements extracted from the impact event, it had to be definitive that the event was being imaged. Working with such a high repetition rate, combined with the inexact timing of the drop weight apparatus and a small camera exposure time lent itself to much speculation as to what part of the drop was going to be captured on any given test. A setup such as this needs prior knowledge about the part of the impact that needs to captured on camera, due to its limited exposure time. For the current purposes, it was important to be able to capture the whole impact event, such that any small changes in the drop timing would not change the quality of the

captured data. With this thought in mind, the 500 kHz tests were halted in favor of a slower repetition rate (50 kHz) that was capable of capturing the entire impact event.

3.5 50 kHz Calibrations

3.5.1 Initial Calibration

Since the repetition rate was decreased, the calibrations were performed again. In the first calibration, the E/D filter set was still used to collect the data based on the information gathered from the 500 kHz experiments. At first, it was assumed that the calibration trend would continue for the slower repetition rates. Also, a more thorough calibration was conducted for every 5 °C from 25 °C to 120 °C. The frame-by-frame data collected for the half and normal loading samples can be seen in Figure 3.13 with the left image being the data for the half loading sample and the right image being the data from the normal loading sample. From this data, the associated calibration curves were created in Figure 3.14.

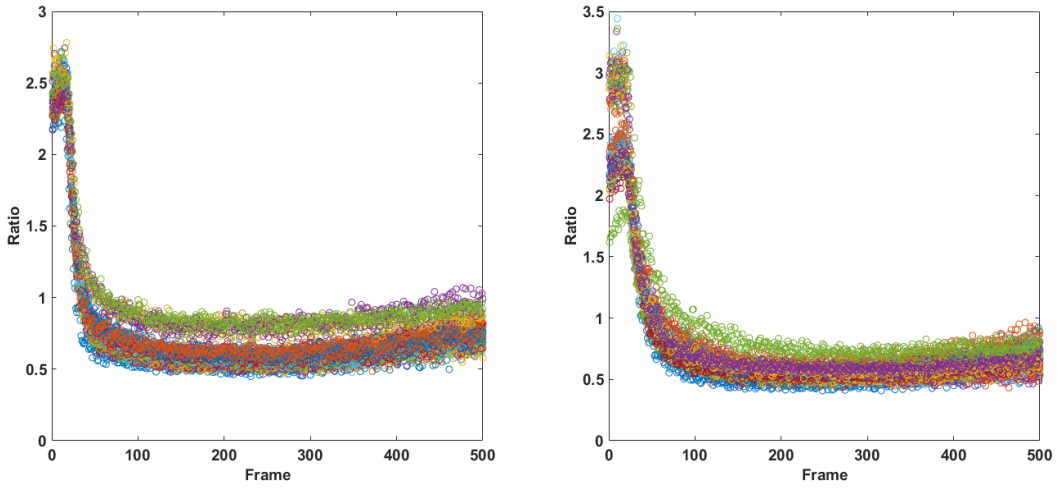

(a) (b)

Figure 3.13 Frame-by-frame 50 kHz calibration data collected for the half loading sample (a) and normal loading sample (b). Each color represents a different test

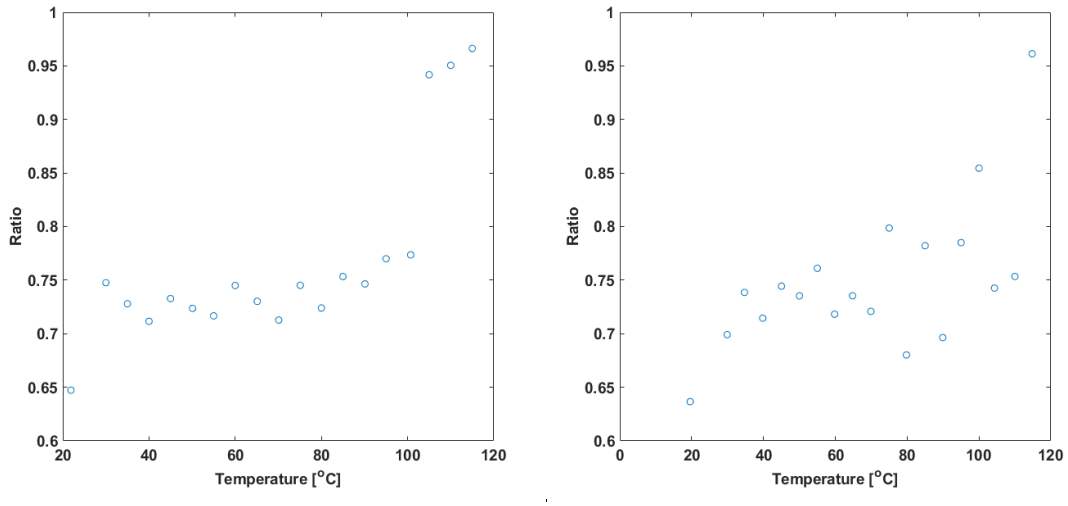

(a) (b)

Figure 3.14 Initial 50 kHz temperature correlation for the half (a) and normal (b) loading sample

One of the first observations from the frame-by-frame data was the interesting action for the first 50 frames where an initial spike in ratio was present, followed by a steep drop and then relatively horizontal action for the remaining frames. This was from the lack of presence or ramping up of the laser at these points. Therefore, there was not an entire laser pulse from which to extract a proper ratio measurement. After this point, the contour edit was added to eliminate most of these initial frames, allowing only those frames with a complete laser profile to be counted in the ratio analysis. Moving on to the actual calibration plots, it was noted that these plots showed poor temperature correlations. Calibration plots for both the half and normal loading samples showed almost horizontal relationships from 30 °C to 100 °C, which would be incapable of correlating a temperature to an intensity ratio. As a further check on this data, the analysis was focused onto an area of the frame-by-frame data clearly exhibiting a horizontal relationship (frames 225-275). This was done to see if the initial frames were altering the final ratios in any way. The calibration curve for the normal loading sample for this select area of data can be seen in Figure 3.15.

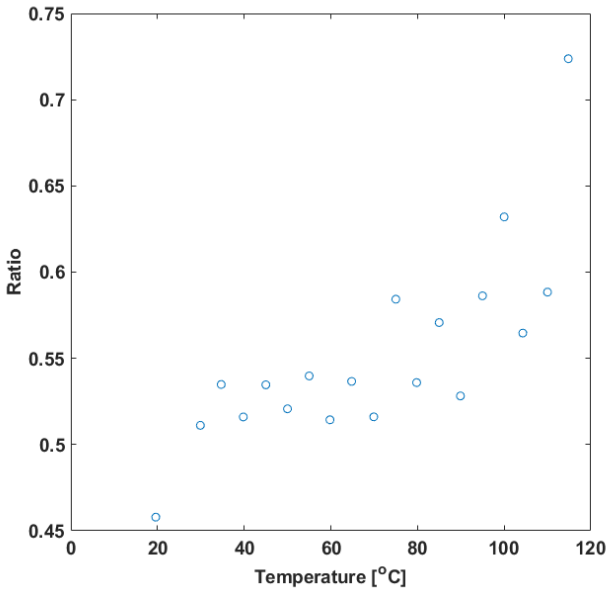

Figure 3.15 Initial 50 kHz temperature correlation for select part of the data from the normal loading sample

Based on this check of the data, it was clear that the lack of trend was not from the strange action of the initial frames. Therefore, the change in repetition rate required a more complete calibration than what was completed. The next calibration conducted was to retest for the most sensitive filter set over the desired temperature range so that one could be implemented into the actual drop testing. Due to much of the variation seen in the above data, the repeatability of the sample ratios at each temperature was also tested.

3.5.2 First Recalibration – Repeatability Testing

A complete recalibration was performed for each sample with each filter set. As stated, this was completed in order to reevaluate if there remained a clear temperature correlation at a lower repetition rate. Five data points were collected every 20 °C from 25 °C up to 300 °C for a total of 70 tests. The frame-by-frame data for this analysis can be seen in Figures 3.16 and 3.17. Plots of the half, normal, and double loading samples for the A/D filter set are presented first followed by the same tests for the E/D filter set.

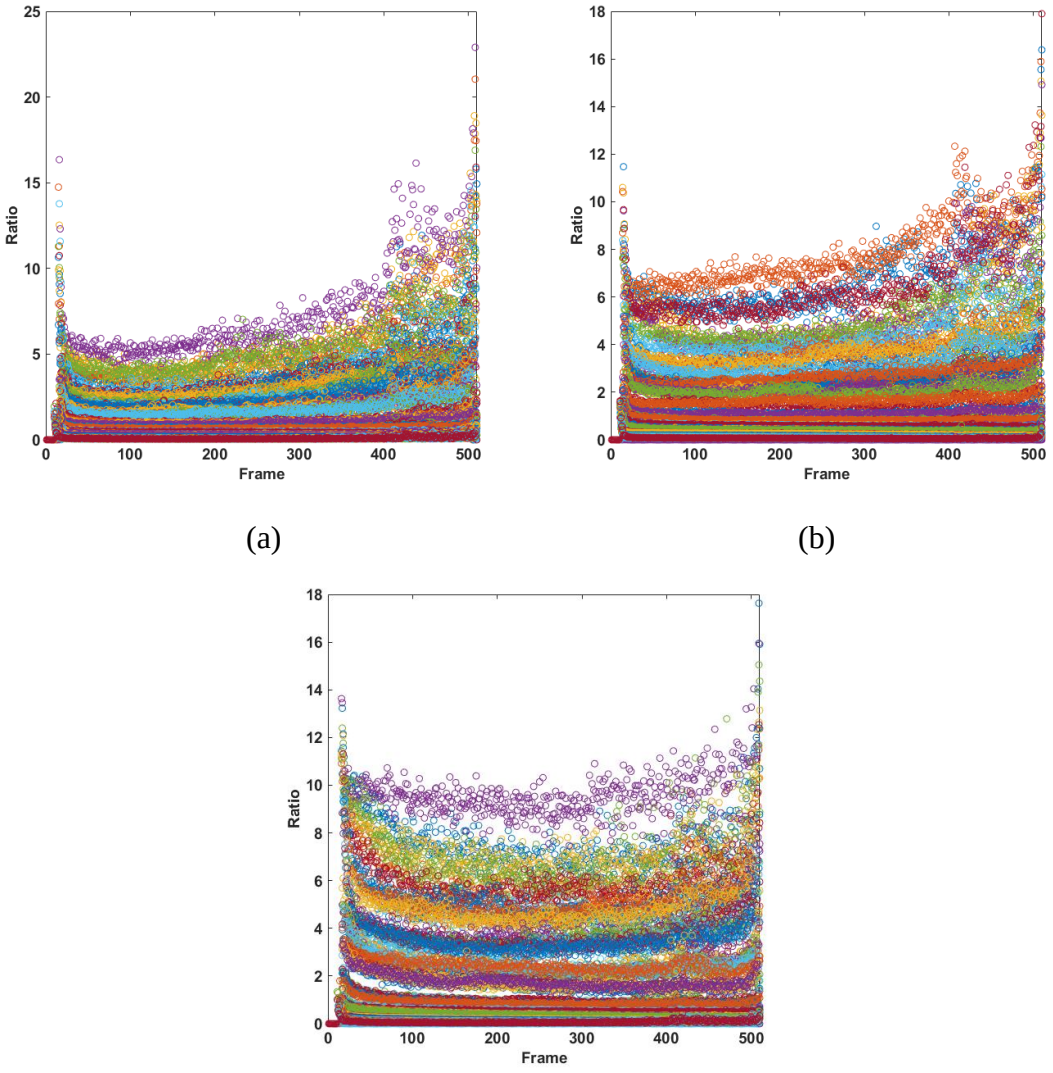

Figure 3.16 Frame-by-frame data for the 50 kHz repeatability calibration for the half (a), normal (b), and double (c) loading samples for the A/D filter set

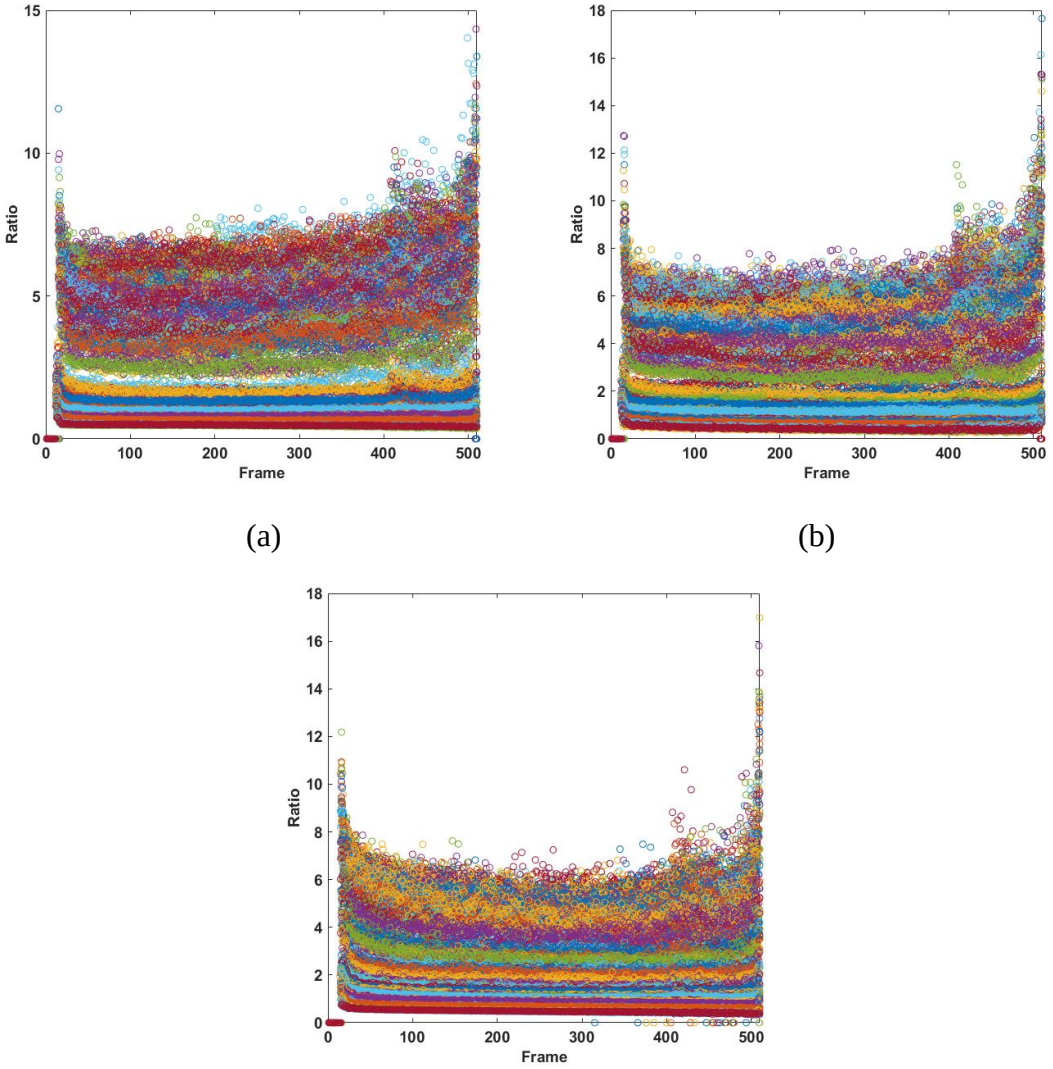

Figure 3.17 Frame-by-frame data for the 50 kHz repeatability calibration for the half (a), normal (b), and double (c) loading samples for the E/D filter set

Based on the information gathered from the initial calibration, the analysis of these tests implemented the contour code into its analysis. Therefore, the first part and last part of the laser burst were eliminated from the ratio calculation. Without this part of the burst there was less of a chance that the final ratio would become skewed due to the ramping up and down of the laser. Other than that note, the frame-by-frame data did not present any immediate information. Using the frame-by-frame data from Figures 3.16 and 3.17, the calibration plots were created in Figures

3.18 and 3.19. As before, the calibration of the half, normal, and double loading samples for the A/D filter set are presented first followed by the E/D filter set.

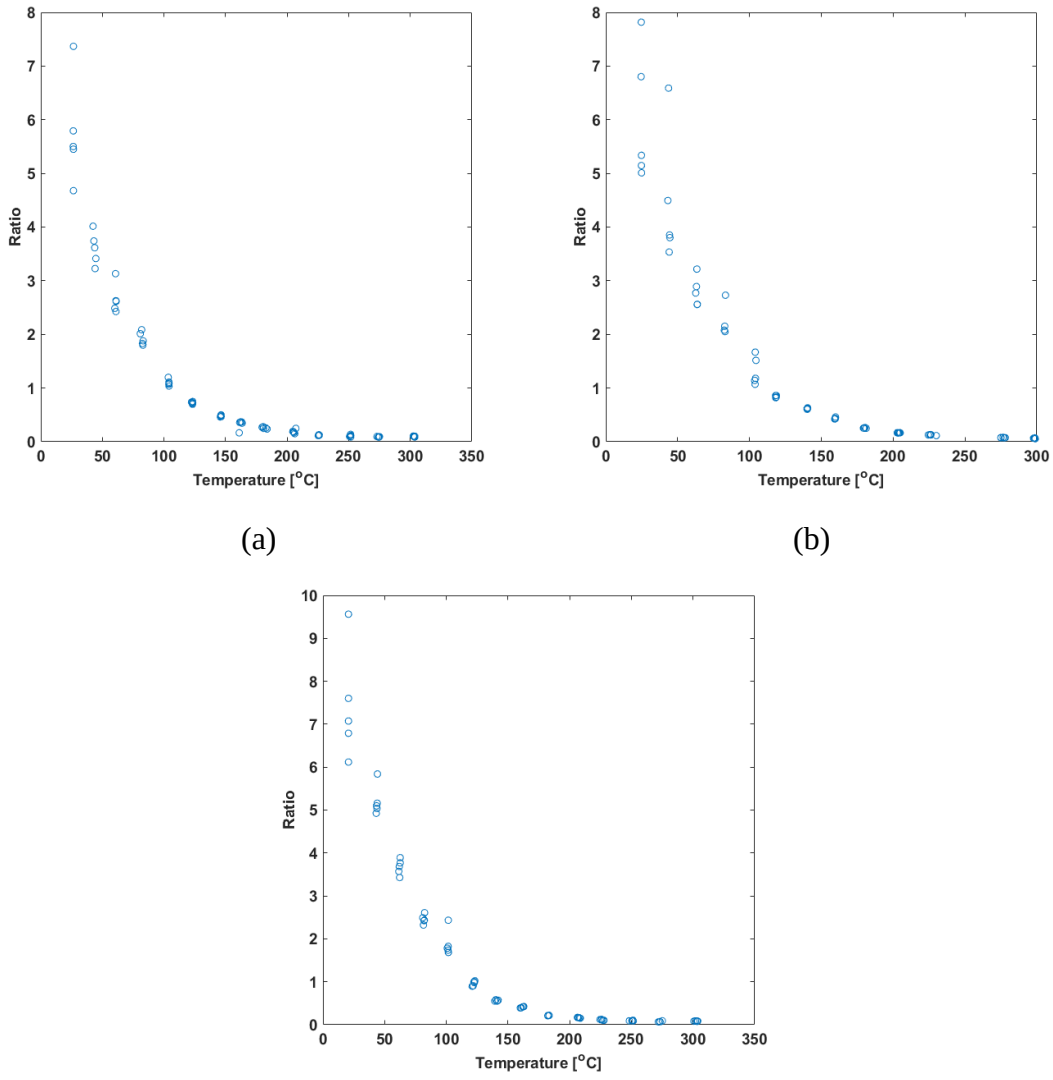

Figure 3.18 Temperature correlations for the 50 kHz calibrations with the A/D filter set for the half (a), normal (b), and double (c) loading samples

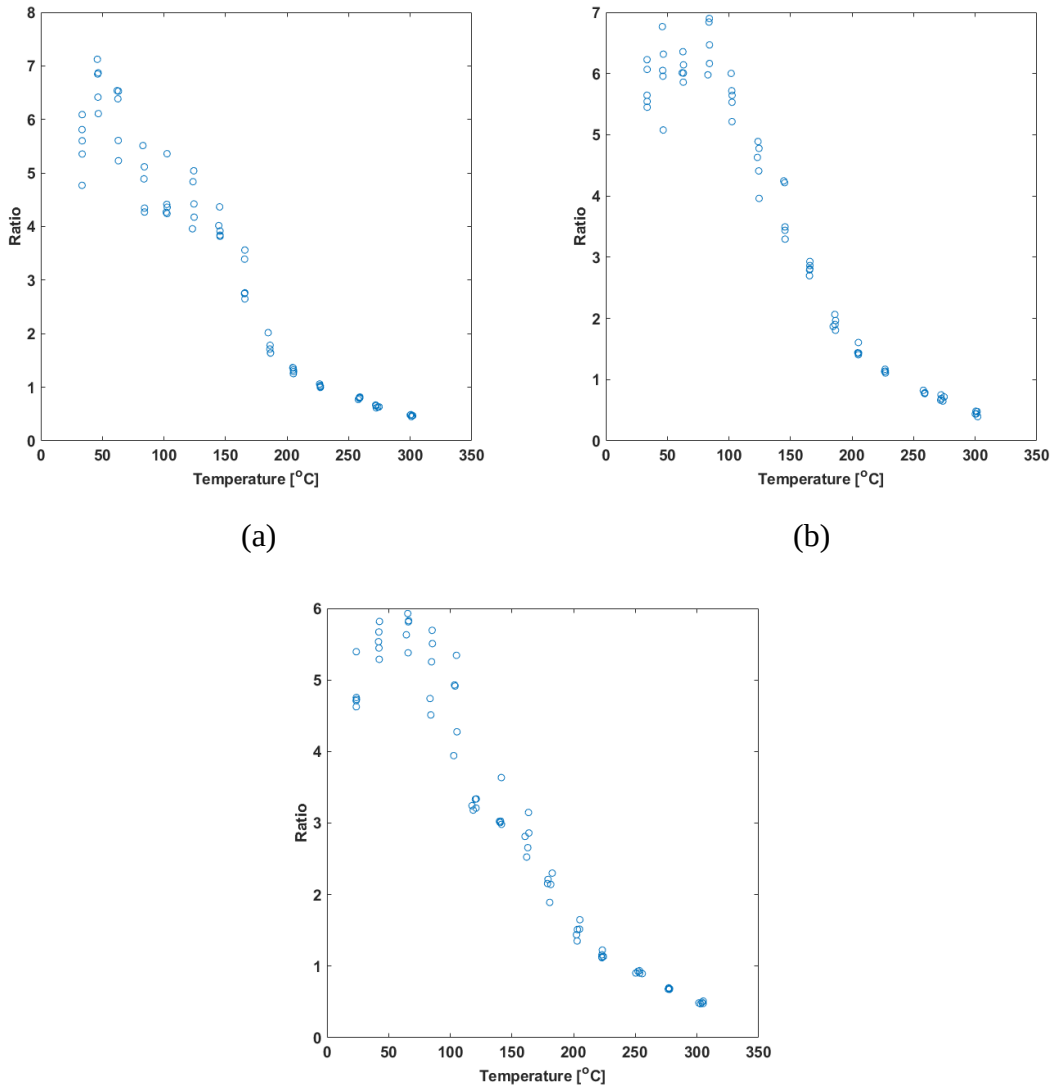

Figure 3.19 Temperature correlations for the 50 kHz calibrations with the E/D filter set for the half (a), normal (b), and double (c) loading samples

Upon first analysis of the calibration curves, there was a clear trend present in the A/D data that was not as evident in the E/D data. While the A/D filter set showed an exponential decrease in ratio, from a ratio of around 5-6 to a ratio of close to zero over the entire temperature range, the E/D set only showed a rough trend starting around 60 °C. With this idea in mind, the A/D filter set was chosen to be implemented in the drop weight testing and will be the only filter set discussed from here on. This initial data also demonstrated much variation between some of the tests at the same temperature. At lower temperatures, all samples exhibited larger variations, which were not

present as the temperature increased. Room temperature variations were between 1-3 for the ratio, but at higher temperatures the variation dropped to essentially zero. As this was the first run of the ratio analysis with the contour applied, the variation minimizations had not yet been implemented in the analysis. However, this correction was performed for the final calibrations comparisons presented later. Even with this large variation at lower temperature, the overall trend of the calibration was clear for each of the samples and similar between all samples. Therefore, each sample would be able to be tested in the drop weight apparatus because there presented a clear correlation from which to extract temperature.

3.5.3 Second Recalibration

As mentioned before, the laser underwent unscheduled maintenance, requiring another calibration to be conducted. However, this presented an opportunity to investigate how important the laser burst profile was to the ratio and correlation, along with the repeatability of the whole calibration. Since the first calibration showed the A/D filter set had a more ideal correlation than E/D, the A/D filter set was the only one tested in this calibration. Additionally, the prior calibration showed the most sensitivity for 25 °C to 200 °C with the ratio decreasing from 5-6 to 0.14-0.16. With this information, that temperature range was chosen as the area of focus for this calibration. Once again, five tests were taken every 20 °C for a total of 45 data points. The frame-by-frame data for this recalibration can be seen in Figures 3.20 with the half, normal, and double loading data presented. Also, their associated final ratios are shown in Figure 3.21.

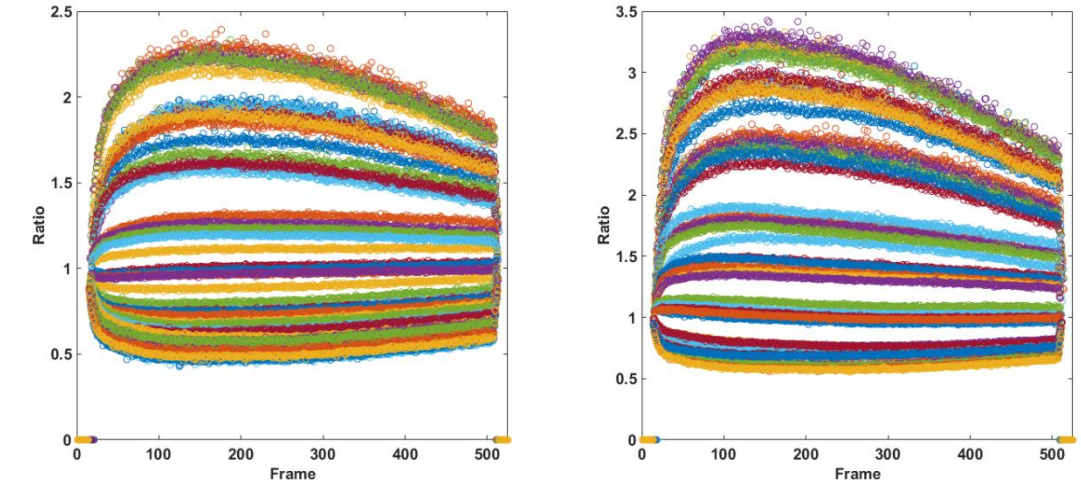

(a)

(b)

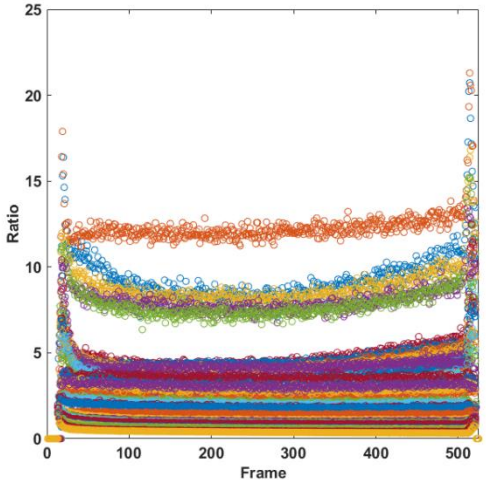

(c)

Figure 3.20 Frame-by-frame data for the 50 kHz recalibration for the half (a), normal (b), and double (c) loading samples for the A/D filter set

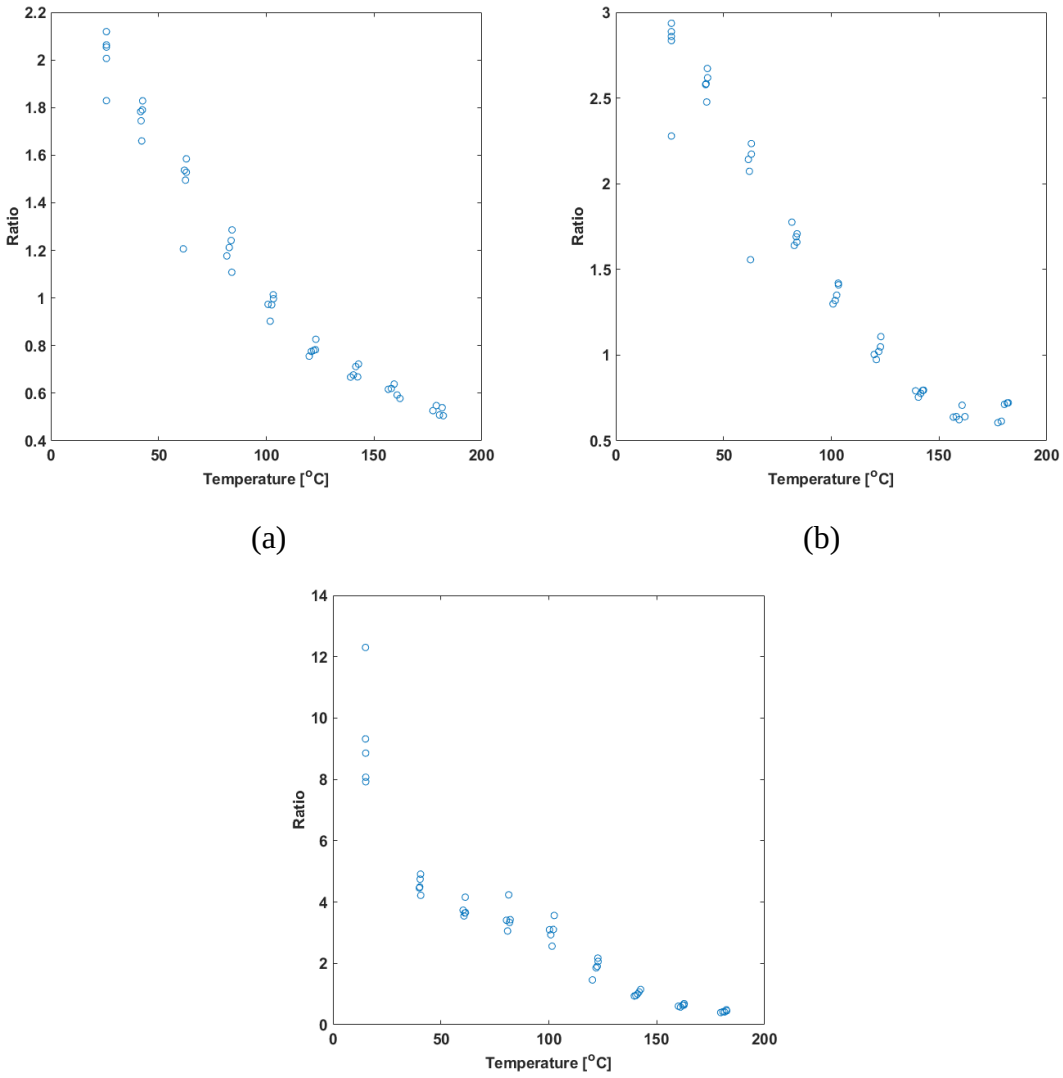

Figure 3.21 Temperature correlations for the 50 kHz recalibrations with the A/D filter set for the half (a), normal (b), and double (c) loading samples

Upon first looking at the frame-by-frame data there was a clear difference in laser burst from the prior calibration, but there was also a difference in laser burst profile between the test with the double loading sample and the tests with the normal and half loading samples. However, a clear overall correlation was still present within all the data. While the laser profile itself was altered, this did not hurt the ability of the samples to demonstrate a temperature correlation. The influence that these burst profiles had on these specific correlations obtained will be discussed in the next section.

Another test performed on this data was a check as to whether the way the analysis was performed influenced the final ratio. Therefore, instead of overlapping the images first to determine a matrix of the ratios and then finding the average of these ratios, the intensity of the laser pulse was first averaged for the left and right images and then the ratio was determined for each frame from the left and right averaged intensities. The data analyzed using this method can be seen below in Figure 3.22 with the half, normal, and double loading data presented. Once again, the associated final ratio plots are then included in Figure 3.23.

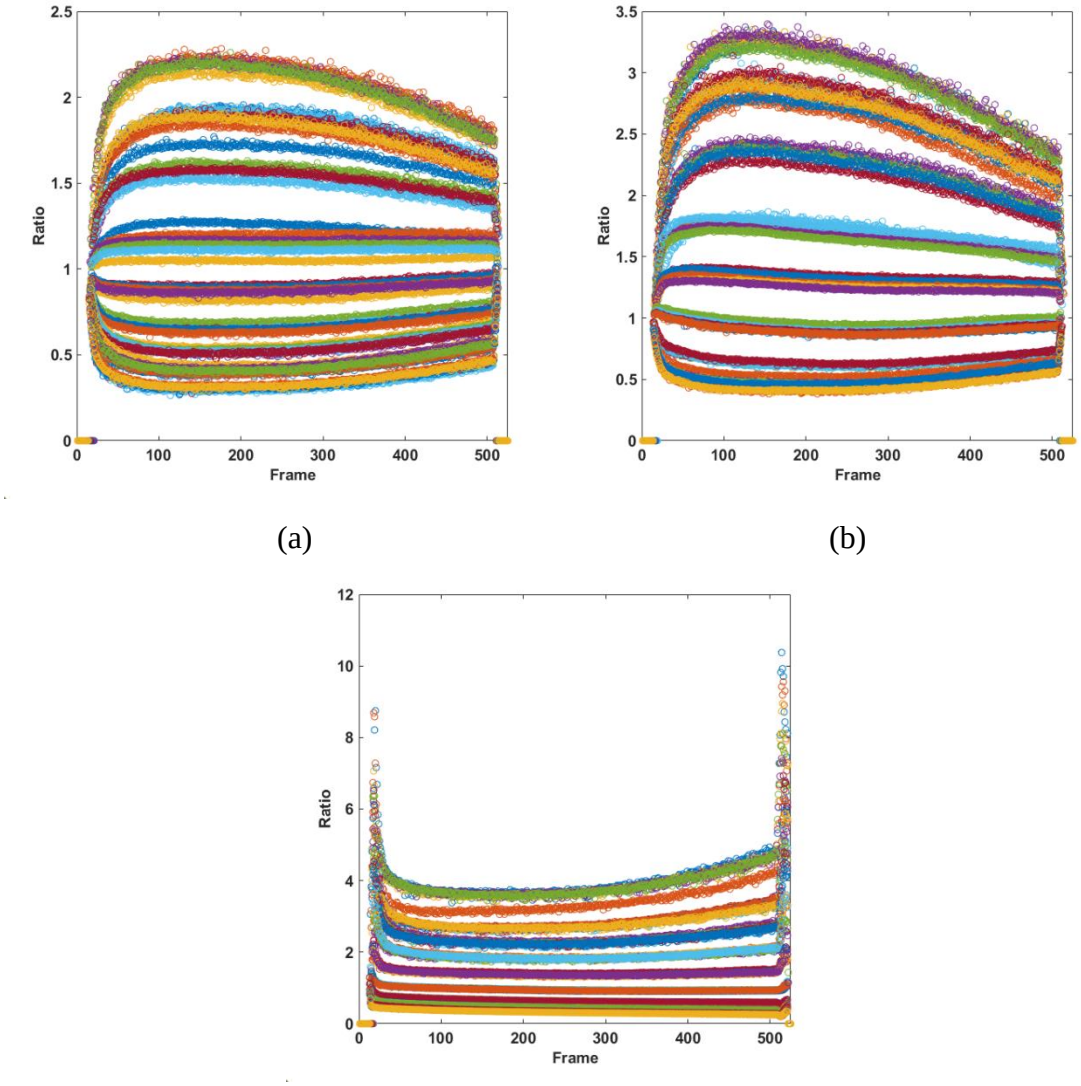

(a) (b)

(c)

Figure 3.22 Frame-by-frame data analyzed with another method for the 50 kHz recalibration for the half (a), normal (b), and double (c) loading samples for the A/D filter set

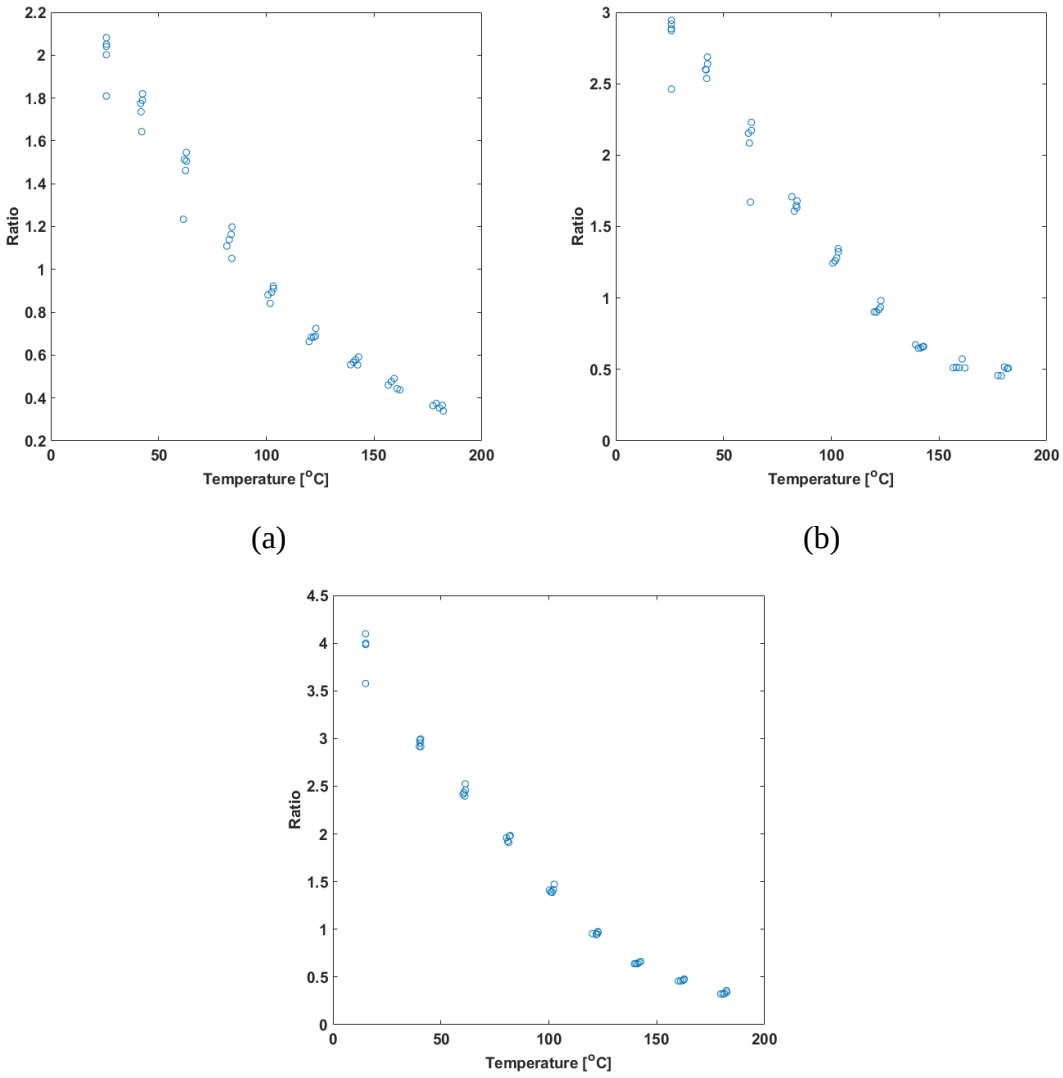

Figure 3.23 Temperature correlations using the other analysis method for the 50 kHz recalibrations with the E/D filter set for the half (a), normal (b), and double (c) loading samples

Initial comparison between the two methods of analysis did indicate that the analysis had some influence into the final ratios obtained. This influence will be further elaborated upon in the subsequent section.

3.5.4 Calibration Comparison

With two calibrations completed covering a similar range, a comparison could be conducted between the two. This would provide information regarding the importance of certain

characteristic in relation to the temperature correlation produced. Overall, a comparison of three calibrations is presented below with the third calibration being created from the different method of analysis. After this point, the first calibration, which was taken before the laser maintenance, will be referred to as calibration 1, the calibration taken after laser maintenance will be referred to as calibration 2, and calibration 3 is the same data as calibration 2, except analyzed with the different method.

Solids loading was one of the main variables of interest within these calibrations. The combined solids loading plots are shown below in Figure 3.24. Within the figure, calibration 1 is on the left followed by calibration 2 and 3.

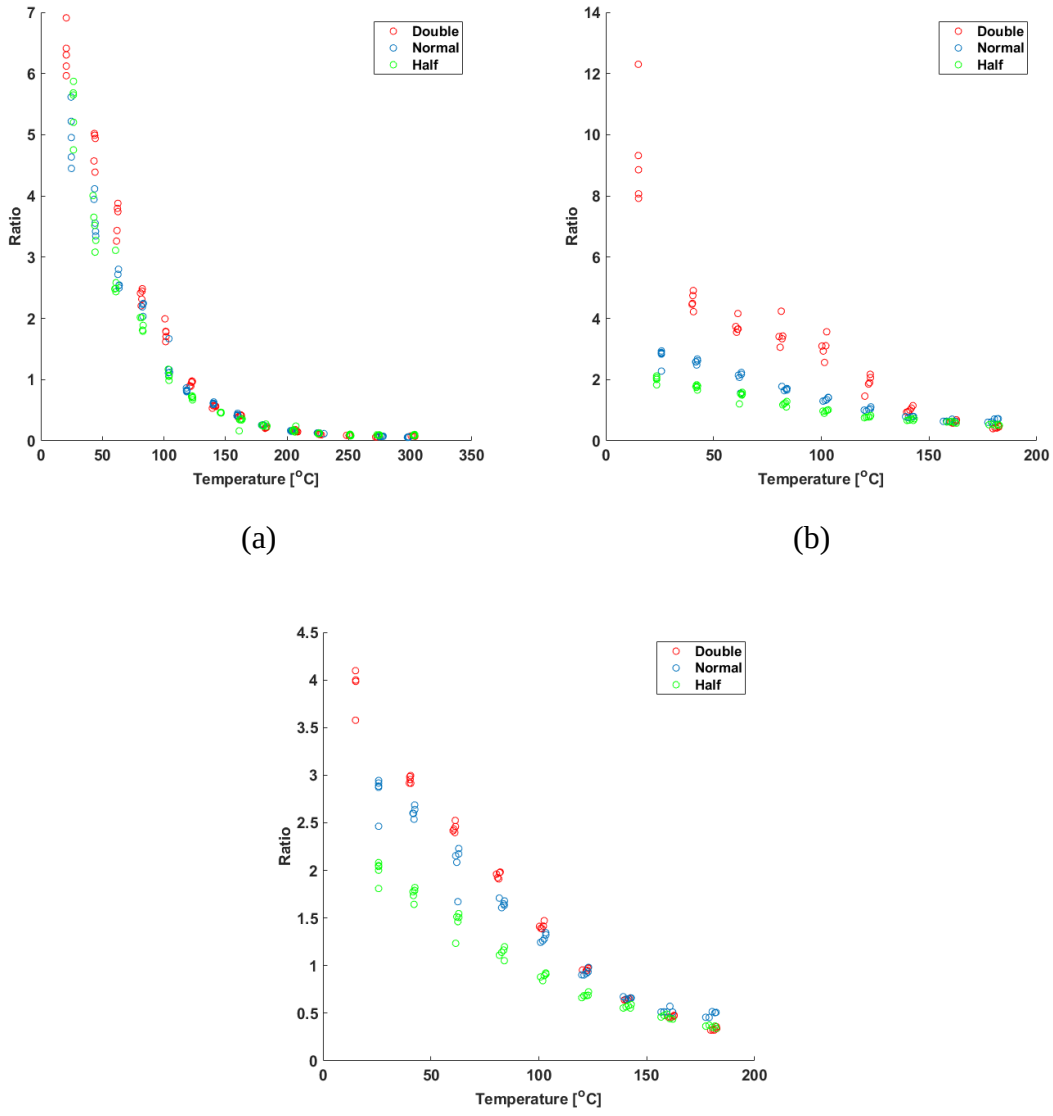

Figure 3.24 Comparison of the final calibrations ratios determined for calibration 1 (a), calibration 2 (b), and calibration 3 (c)

Between these three plots, the most noticeable difference was the magnitude of the ratio present in the different samples. It was much more noticeable in calibrations 2 and 3, but the double loading sample reached higher ratios over the entire temperature range than other samples. The normal loading sample had the next highest ratios and the half loading had the smallest magnitude ratios. These differences in magnitude were also most prevalent at the lower temperatures, until the ratios merged around 140 °C. This difference between the samples was attributed to the different concentrations of phosphor in each sample. Since the double loading sample had the

highest concentration of phosphor, its luminescence was strongest, attributing to the higher ratio. Then, as the solids loading was decreased, the luminescence slightly decreased. However, regardless of how the ratio changed, a correlation was present for each sample. Using this data, a room temperature (25 °C) correction was also applied based on the line of best fit from the data. This correction was determined by finding the ratio at 25 °C and dividing the whole calibration line by this value. This was a way to normalize all of the data by one common point. These corrected plots can be seen below in Figure 3.25.

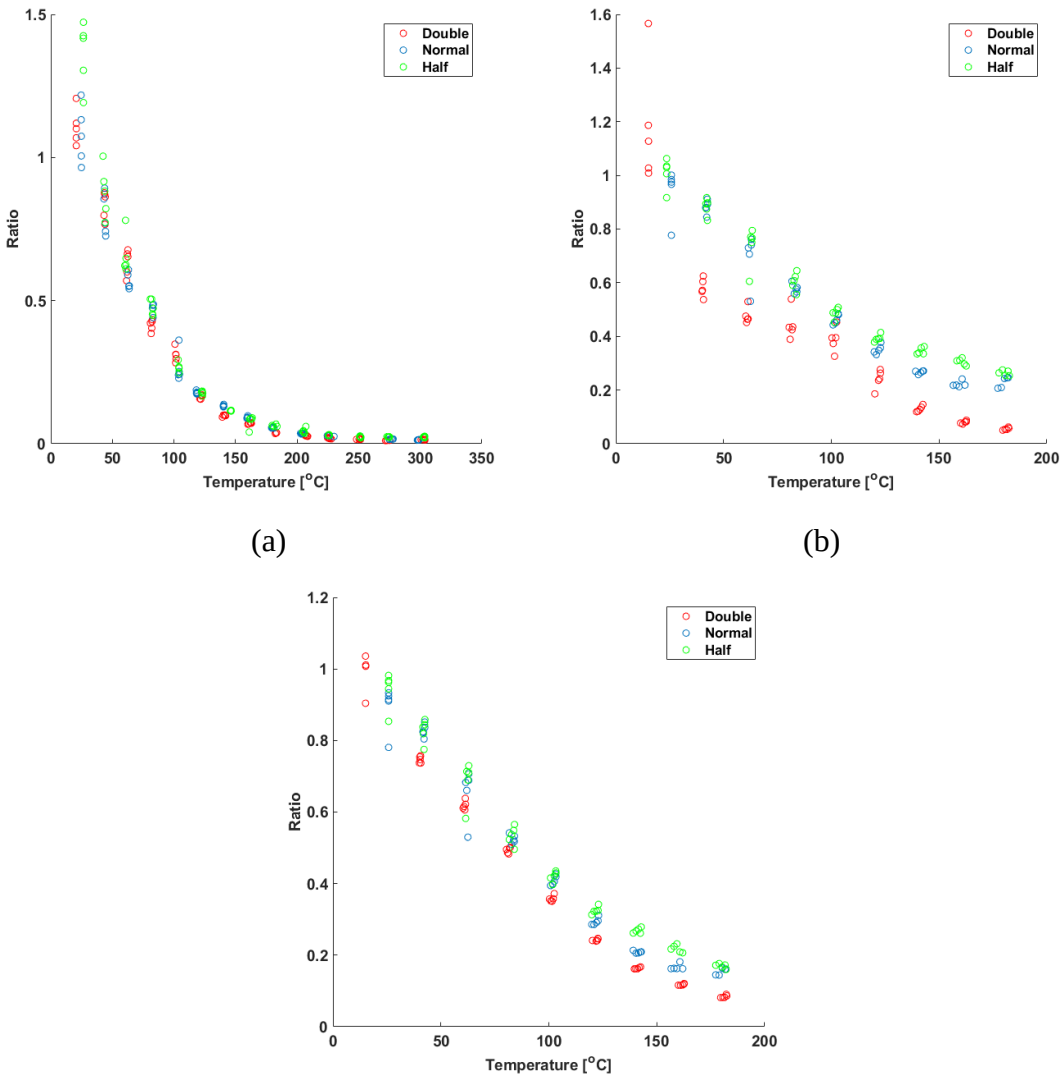

Figure 3.25 Comparison of the final calibrations ratios corrected to room temperature determined for calibration 1 (a), calibration 2 (b), and calibration 3 (c)

When the correction was applied, these plots did demonstrate something interesting in the fact that they all came much closer to the same trend. Calibration 1 and 3 had all of the solids loadings essentially overlapping. This means that even though the magnitude of the overall data was different, when corrected for this magnitude difference, all of the data presents a similar trend. All of which still show a strong correlation to temperature. Therefore, all three solids loading samples would be acceptable to use to correlate an intensity ratio to a temperature with no one sample showing a large advantage over the others.

Another area of interest in within the calibrations was how the laser itself influenced the calibrations. This was determined through comparison of the calibrations before and after the laser was fixed, but also by comparison of the laser burst profile within a test. When the laser underwent unscheduled maintenance, it was able to produce more power under lower settings, but regardless of that fact, the power that excited the sample was similar between the calibrations with a similar beam profile. Therefore, the main factor was the difference in burst profile. As seen in the frame-by-frame data in Figures 3.17 and 3.20 from calibrations 1 and 2, respectively, the action of the laser burst changed dramatically between the calibrations. Specifically towards the end of the laser burst, the calibration became much smoother for all samples after the laser was fixed. A comparison of the ratios obtained for each solids loading is presented below in Figure 3.26.

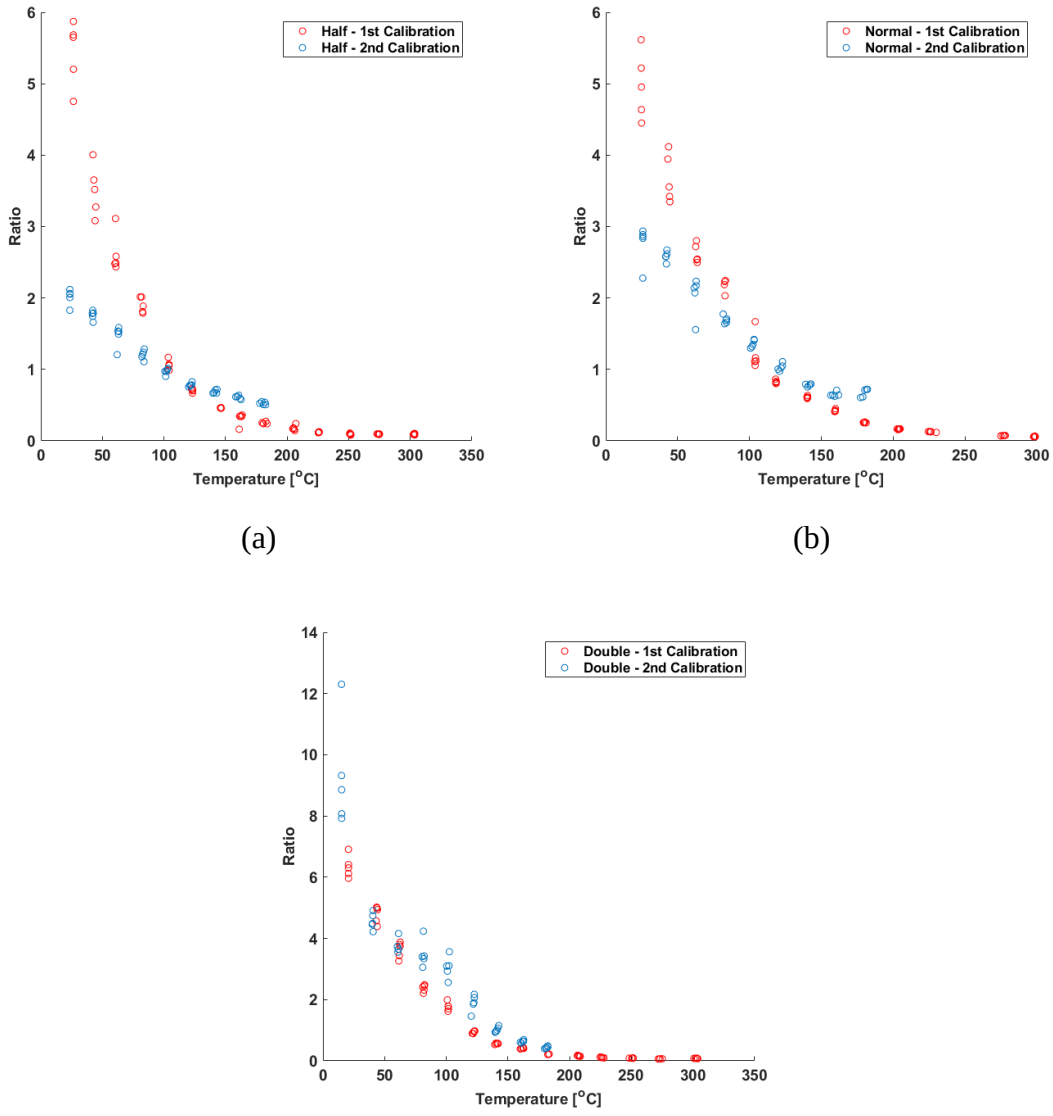

Figure 3.26 Comparison of the ratios determined for calibration 1 and 2 for the half (a), normal (b), and double (c) loading samples

When looking at this data, there was a clear influence the laser burst had on the final ratios collected. The only sample's calibration that remained relatively the same was the double loading sample. On the other hand, the normal and half loading samples showed large differences in shape between the two calibrations. Due to this trend alteration for these two cases, the laser burst also has more of importance as the solids loading was decreased. The more dispersed phosphor particles make the differences in the burst more prevalent, which can be seen from the trend deviation

becoming more extreme as the solids loading was decreased. Even attempting a room temperature correction did not help make the trends any more similar, as can be seen in Figure 3.27.

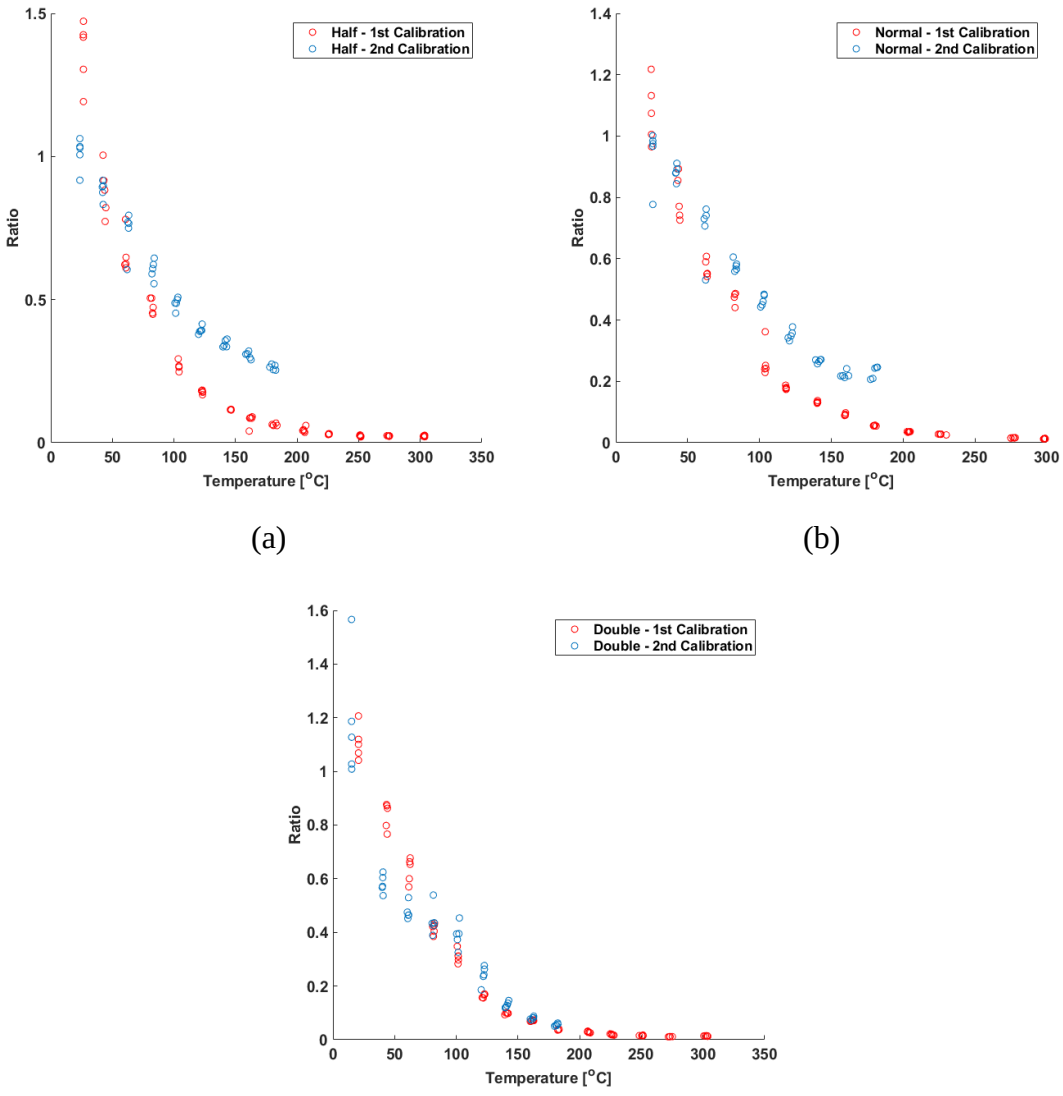

Figure 3.27 Comparison of the room temperature corrected ratios determined for calibration 1 and 2 for the half (a), normal (b), and double (c) loading samples

Based on these trends, the laser burst was an important variable during the calibration process and recalibration of the samples between any adjustments made to the laser burst was necessary. An additional test performed on the laser burst was to determine the influence of calibrating over the whole burst versus over a select part of the burst. In order to test this idea,

frames 100-400 were analyzed and compared to the analysis of the entire pulse, which can be seen in Figure 3.28. The plots in this figure are only for calibration 2 because all of the calibrations showed similar trends.

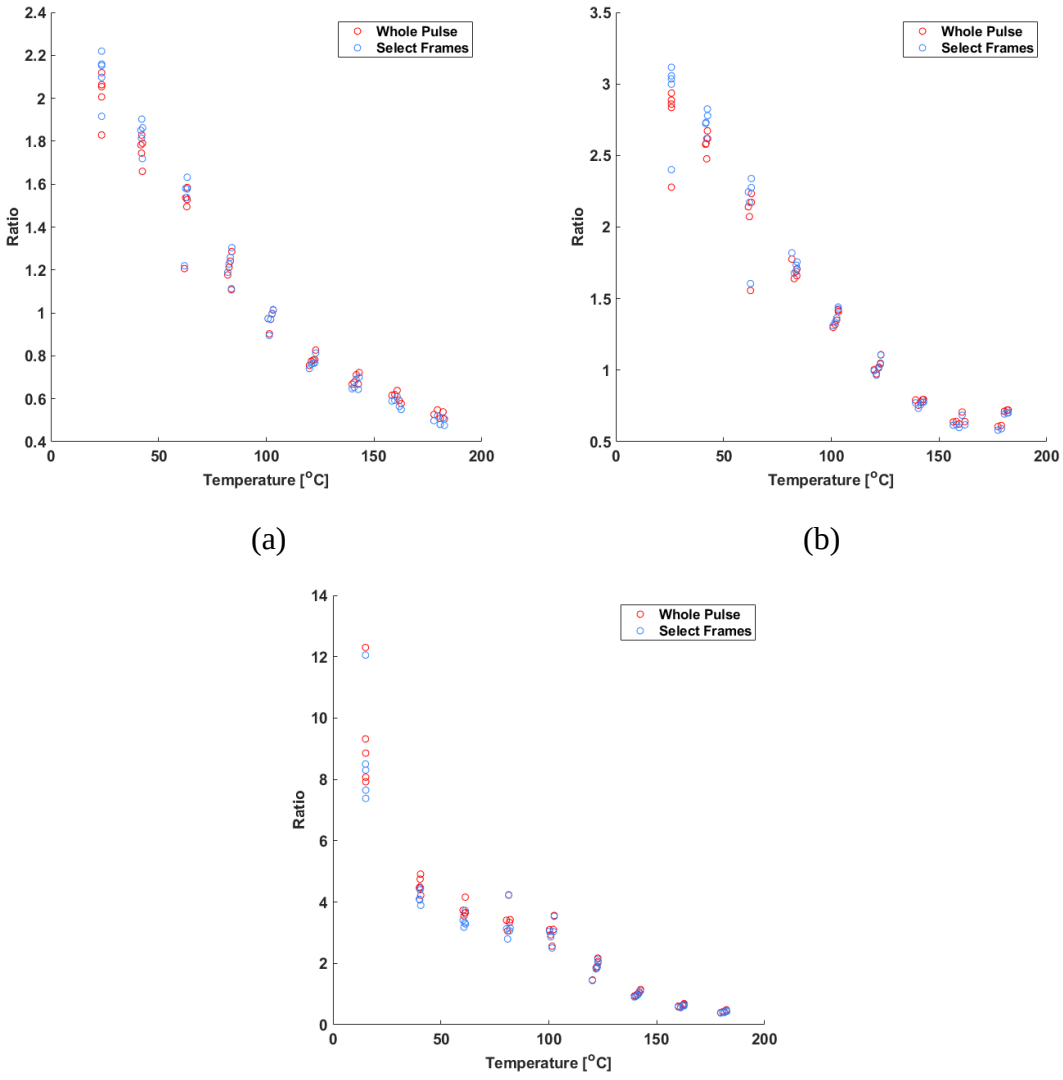

Figure 3.28 Comparison of the ratios determined for calibration 2 in relation to choosing the whole laser burst or a select are of the laser burst for the half (a), normal (b), and double (c) loading samples

In relation to analyzing a select part of the pulse versus the whole pulse, there was little to no difference in the overall trend present. This was partially due to the implementation of the contour code that had already eliminated most of the data points that did not contain important

information. This way there were less skewed data points to change the calibration. Overall, the trend remained consistent regardless of the part of the pulse selected for analysis.

Using the data collected from calibrations, one final comparison was conducted and this was a comparison between the two methods of analysis. As previously mentioned, calibration 2 determined a ratio matrix first and then took the average of this ratio matrix, while calibration 3 took the average of the left and right images individually and then took the ratio. Figure 3.29 shows the calibration curves for all solids loadings created from these two separate methods.

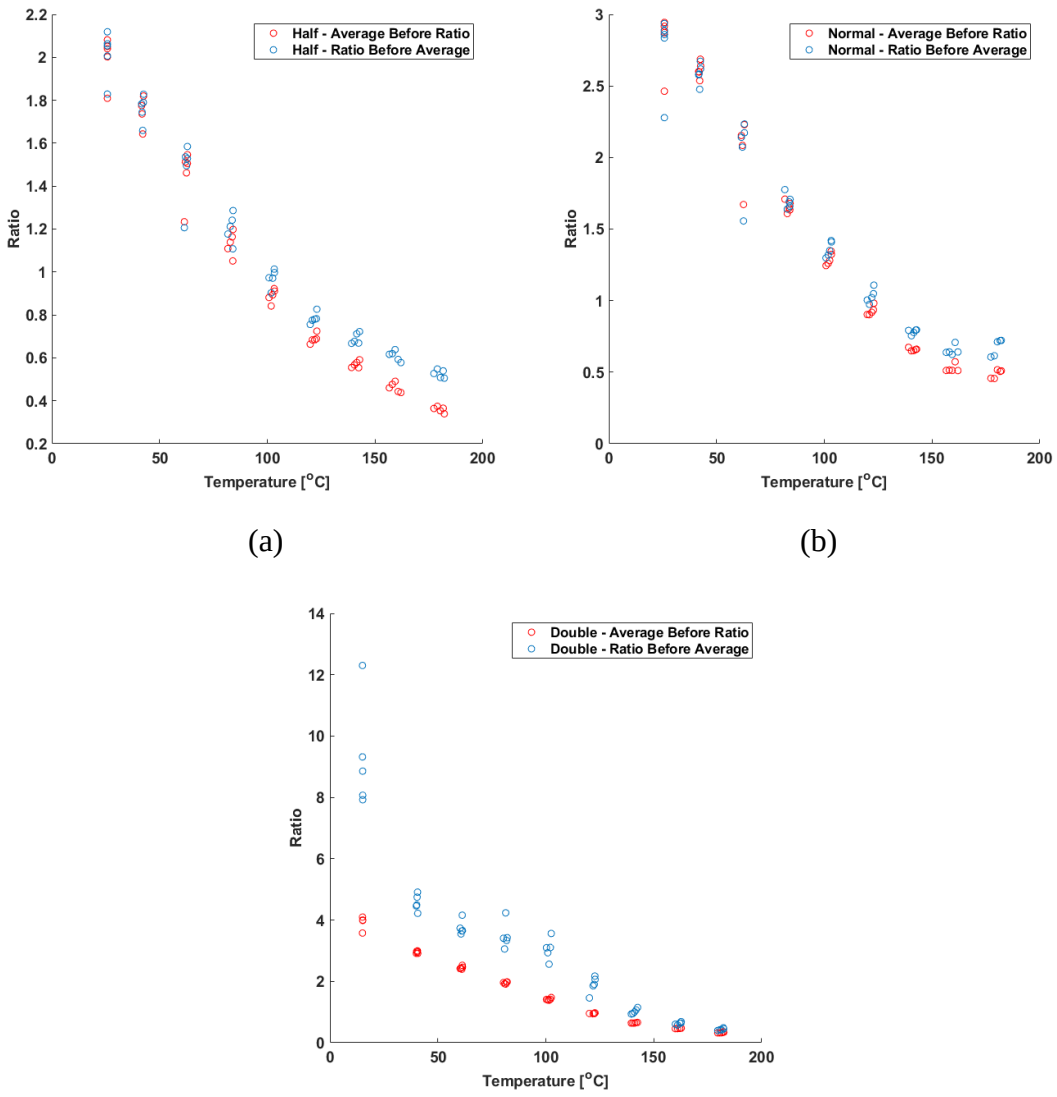

Figure 3.29 Comparison of the final ratios determined for calibrations 2 and 3 for the half (a), normal (b), and double (c) loading samples

When reviewing these plots, the sample that demonstrated the most difference between analysis methods was the double solids loading. Taking the ratio before averaging resulted in much larger ratios than when the average was taken first and the ratio was determined after. However, when the ratios were corrected to the room temperature, the trends became much more similar, as is seen in Figure 3.30. This means that the trend was still similar, even if the magnitude was different. Since the half and normal loading samples already showed similarity between the two analysis methods Figure 3.30 is only shown for the double loading sample.

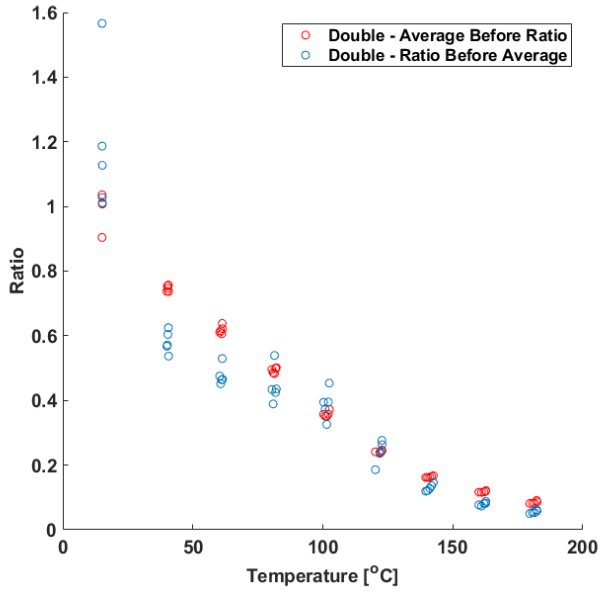

Figure 3.30 Comparison of the corrected final ratios determined for calibrations 2 and 3 for the double loading sample

Another observation of note was the variation difference between the two methods of analysis in the double loading sample. Averaging before taking the ratio resulted in much more consistent ratios for the double loading sample. The cause of this was most likely from a slight shift in the image registration. Since the laser was put through a diffuser, it was rather homogenous throughout, but a slight shift in the image registration could cause some error in several pixels, resulting in ratios that were incorrect. Taking the average before the ratio did not depend on an overlap, so it was not possible for the ratios to be incorrect due to a shift in registration. Rather than revealing a large difference between samples physically, this test showed the quality of the image registration. While the half and normal loading samples did not exhibit much difference

between the methods of analysis, the double loading sample showed large variations in one set of data that was not present in the other, meaning its image registration was slightly off. Due to two slightly different correlations being reached by the different methods of analysis, they were both conducted when analyzing the final drop tests for comparison. However, more focus will be placed on the analysis that takes the average before taking the ratio, as these calibrations showed much less variation and did not have to rely on a perfect registration. The drop tests analyzed in the other way will be mentioned for comparison, but not shown.

3.5.5 Final Temperature Correlations

Before temperature correlations were able to be made for the drop tests, a correlation line first had to be developed for the calibration. To obtain a near linear fit for this data, the log of the ratios was computed and plotted against temperature and then a line of best fit was formed. Using the best fit line, the following calibrations were made. Figure 3.31 shows these calibration lines for the non-corrected ratios with the 95% confidence interval also plotted. These calibration lines were also made for the corrected case, but they are not shown. With these final calibration plots formed, correlations to temperature were finally able to be produced, which will be shown in the next section.

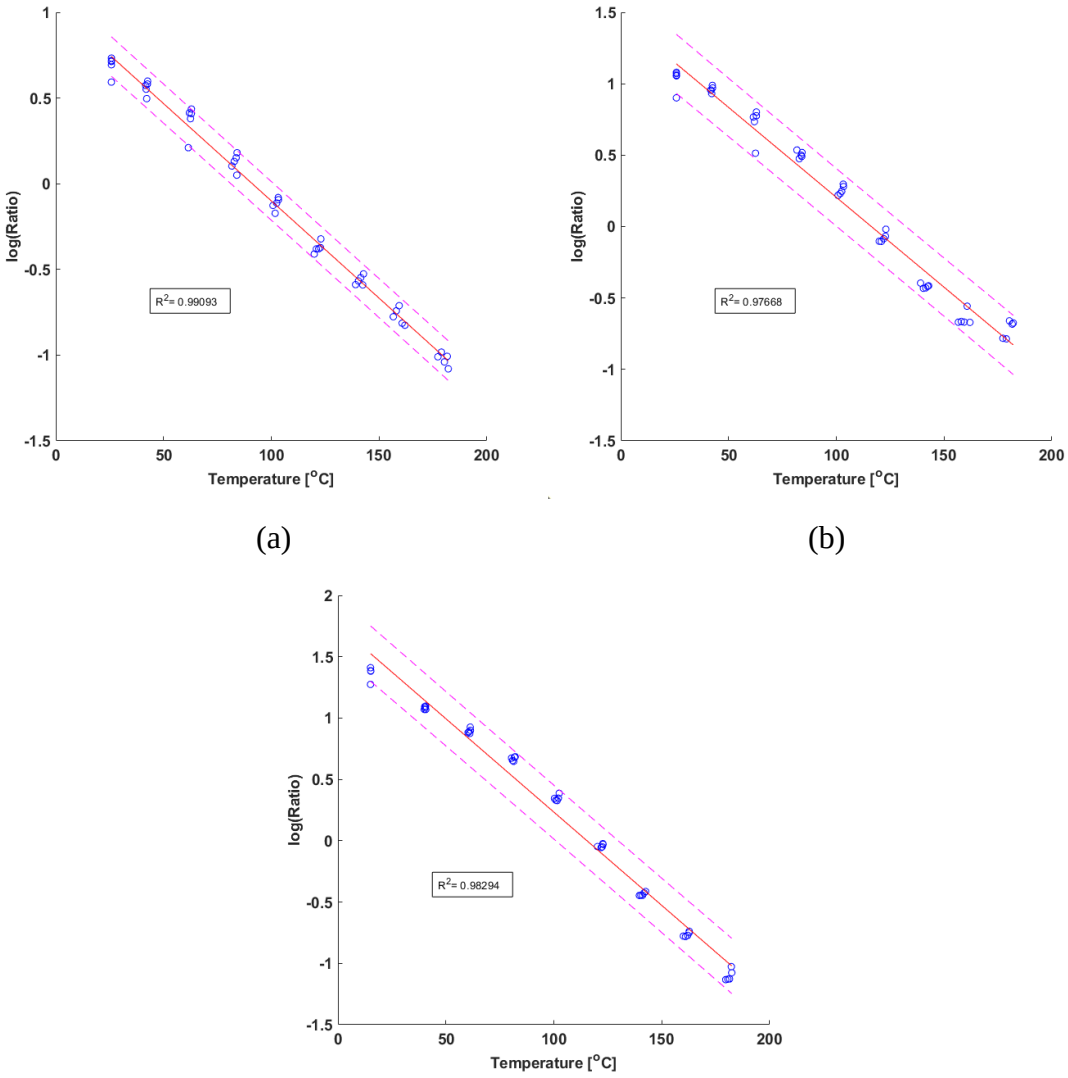

Figure 3.31 Final temperature correlations with 95% confidence interval used for the half (a), normal (b), and double (c) loading samples

3.6 50 kHz Drop Tests

When the drop tests commenced, five tests were conducted for each solids loading. One initial test was first conducted for the double solids loading case to ensure that enough signal was being captured by the camera. In all of the tests, the delay was set so that the start of impact on the sample began in the 1.5 ms to 2.5 ms range after the camera was recording. The frame-by-frame data for the three solids loadings can be seen below in Figure 3.32 with the double solids loading shown on the left, followed by the normal and half solids loadings.

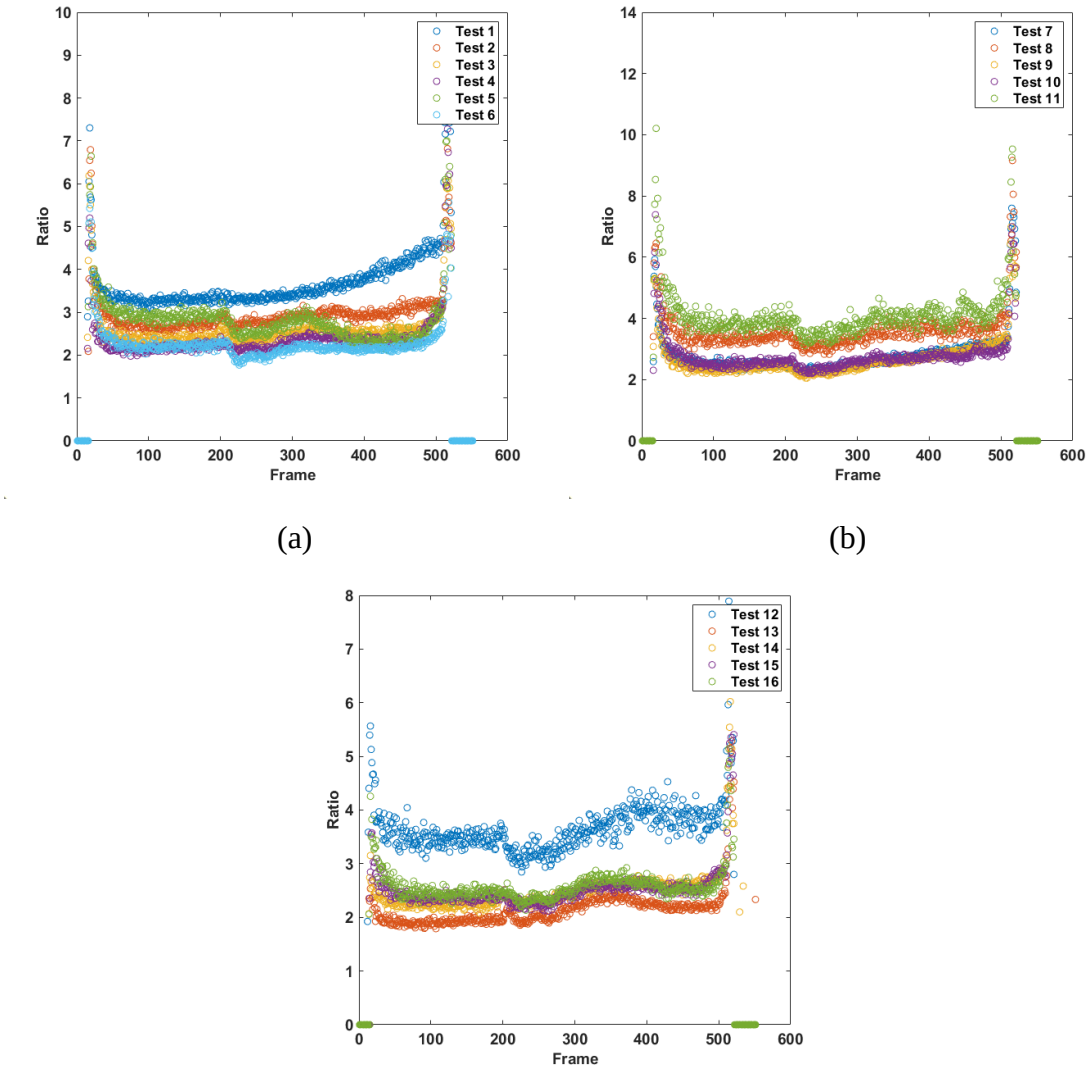

Figure 3.32 Frame-by-frame data for the 50 kHz drop tests conducted with the double (a), normal (b), and half (c) loading samples

During initial analysis of the frame-by-frame data, there were some distinct properties noticed. The first property was an increase of the ratio towards the end of the pulse for the test that did not involve a drop. This would artificially decrease the final temperature measurements, so in order to correct this behavior of the laser burst, all the rest of the tests were divided by this test. Additionally, even though all tests were supposed to be starting at the same temperature (room temperature), which was 15 °C, most of the starting ratios varied from each other. With initial ratios varying in such a way, the temperature correlations would yield inaccurate temperatures, but

changes in temperature could be determined. These changes in temperature were calculated for comparison with the final temperature correlations. To find the change in temperature for the tests, the entire test was corrected to the first section of the plot at room temperature, bringing the initial section of the data to zero temperature change. The rest of the data was then related back to the absolute calibrations, not the corrected ones and changes from zero were plotted. However, an actual temperature was also to be determined for the data. Since each test was beginning at room temperature, a second correction was applied. Each test was divided by the ratio over its initial frames that were assumed to be at room temperature (around time 2 ms). This yielded corrected ratios, which was able to correlate back to a temperature using the room temperature corrected ratios from the prior calibrations. Two temperature plots came from each set of data and they will both be discussed in the sections below.

Besides determining the temperature from the intensity ratio method, calculations were performed for an ideal case. Using conservation of energy and assuming no losses in energy to the environment, an ideal temperature rise was able to be calculated from the material properties of the samples. The material properties used for each sample, along with its ideal temperature rise can be seen in Table 3.3 below.

Table 3.3 Material properties used and ideal temperature rise of each sample

Property	**Double Loading**	**Normal Loading**	**Half Loading**
Sylgard Heat Capacity [21] (J/g-C)	1.624		
ZnO Heat Capacity [22] (J/g-C)	0.495		
Combined Heat Capacity (J/g-C)	1.4902	1.320	1.1798
Sylgard Density [21] (g/cc)	1.03		
ZnO Density [23] (g/cc)	5.6		
Mass (g)	0.6819	0.5723	0.5122
Ideal Temperature Rise (°C)	**71.7**	**82.0**	**89.7**

These were not the expected temperature rises for the samples because of energy losses due to friction and deformation of the sample, among other things. There would also be the presence of a temperature difference between the side of the sample that experiences the impact

and the side that was being imaged. This difference was caused by thermal conductivity through the sample itself. With these ideas in mind, the calculated ideal temperatures would serve as an upper bound of the determined temperature.

Before discussing the results, the final point of discussion involved the ratios determined from the other analysis method. This method resulted in much more variation in the data, along with ratios that were much larger, around 15. The variation in the data was to be expected as that was demonstrated in the prior calibrations. On the other hand, the high ratios were not expected since these types of ratios were not present in the calibrations or the other analysis method. As discussed prior, this action could have been caused by a small shift in the registration, but it also could have been an impact of the change in laser fluence. When testing, the laser burst had a smaller profile because of constrictions in the setup, so there was more energy focused in a localized area. This increase in energy over a smaller area could have increased the ratios determined. Due to this strange behavior in the data specific to this method of analysis and not a result of the data itself, the data from this analysis will not be discussed below.

In all the tests, there were three distinct areas present, an initial heating, a cooling, and a secondary heating section, so the presented data will be broken down as such. The initial heating area consistently began around 4 ms, lasting until around 5 ms. This was assumed to be the heat associated with the initial impact of the drop weight on the sample. Next, came the cooling section, which lasted from 5 ms to around 6 ms to 7 ms. During this section, the sample was still being compressed, but the energy from the drop weight was going towards deforming the sample, rather than heating it up. Lastly, the secondary heating occurred from 7 ms until around 9.5 ms. This last section was when the sample was fully compressed and the energy from the drop weight could once again go towards heating the sample. This section was usually the greatest heat rise as well because all of the energy from the drop weight was transferred into the sample at this point. After 9.5 ms, there was consistently a steep drop in temperature. This was possibly due to cooling from the termination of the impact event. However, at this time, the laser was also completing its burst, so the decrease in temperature could have been caused by the ramping down of the laser. In reference to the IR video taken in Figure 3.6, there was also a similar heating, cooling, and reheating seen, but on a much different timescale than what was described above. Since the laser was able to focus on the sample, unlike the IR video, more focus was placed on the data collected

from the high-speed camera. Further discussion about the IR video can be found in the improvements section.

Within each plot, a moving average was fit to the data points, which was the line to which the temperature measurements were referenced. Above and below each moving average line is the 95% confidence interval from the calibration plot.

3.6.1 Double Phosphor Loading

In Figure 3.33, the plots of the change in temperature are shown for all five tests. Following those plots, Figure 3.34 shows the temperature determined for the different tests. All of the results are summarized in Table 3.4 for the change in temperature plots and Table 3.5 for the actual temperature plots. In Table 3.4 the change in temperature is related back to an initial room temperature of 15 °C.

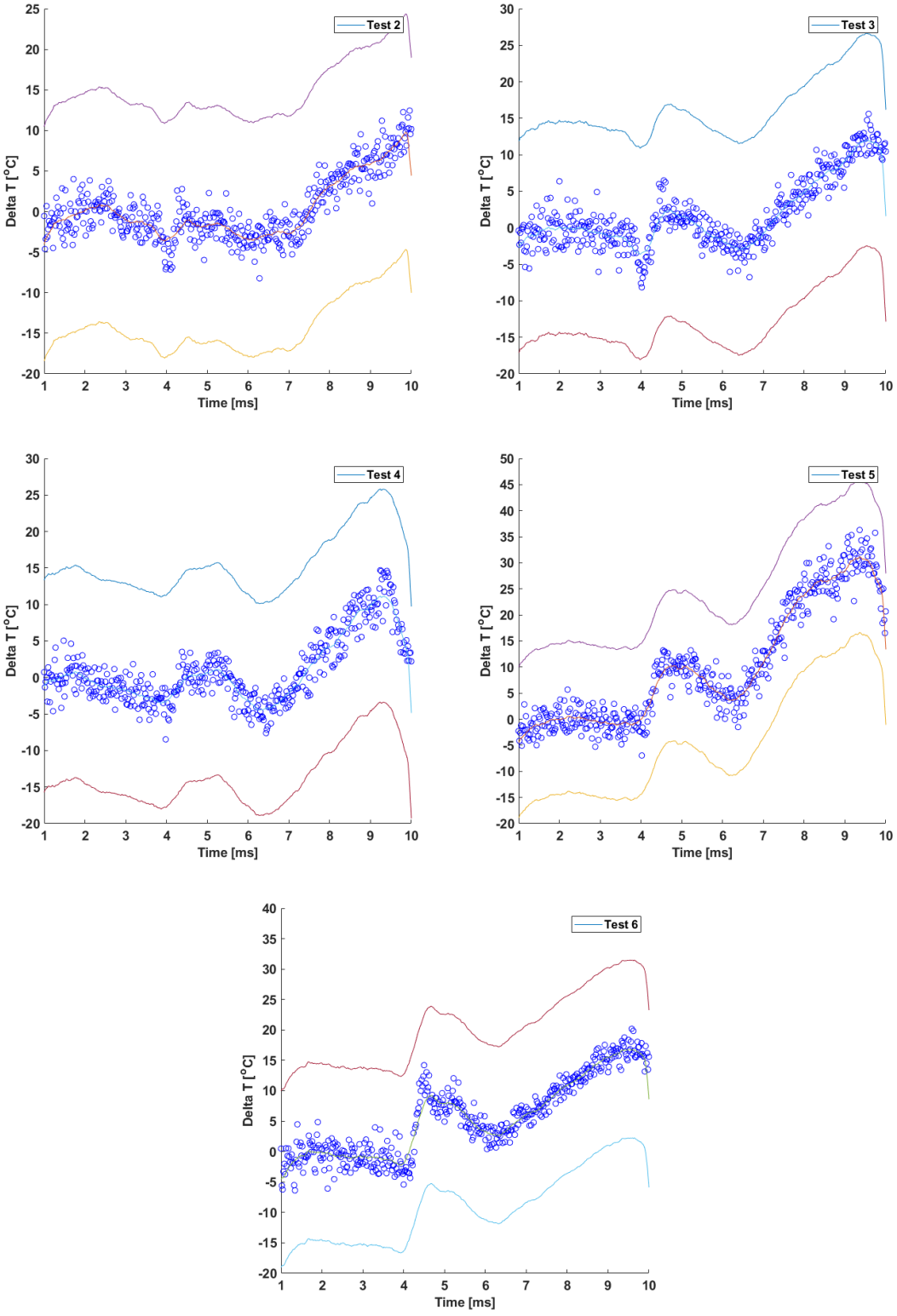

Figure 3.33 Frame-by-frame data for the change in temperature over the drop weight impact of the double loading samples

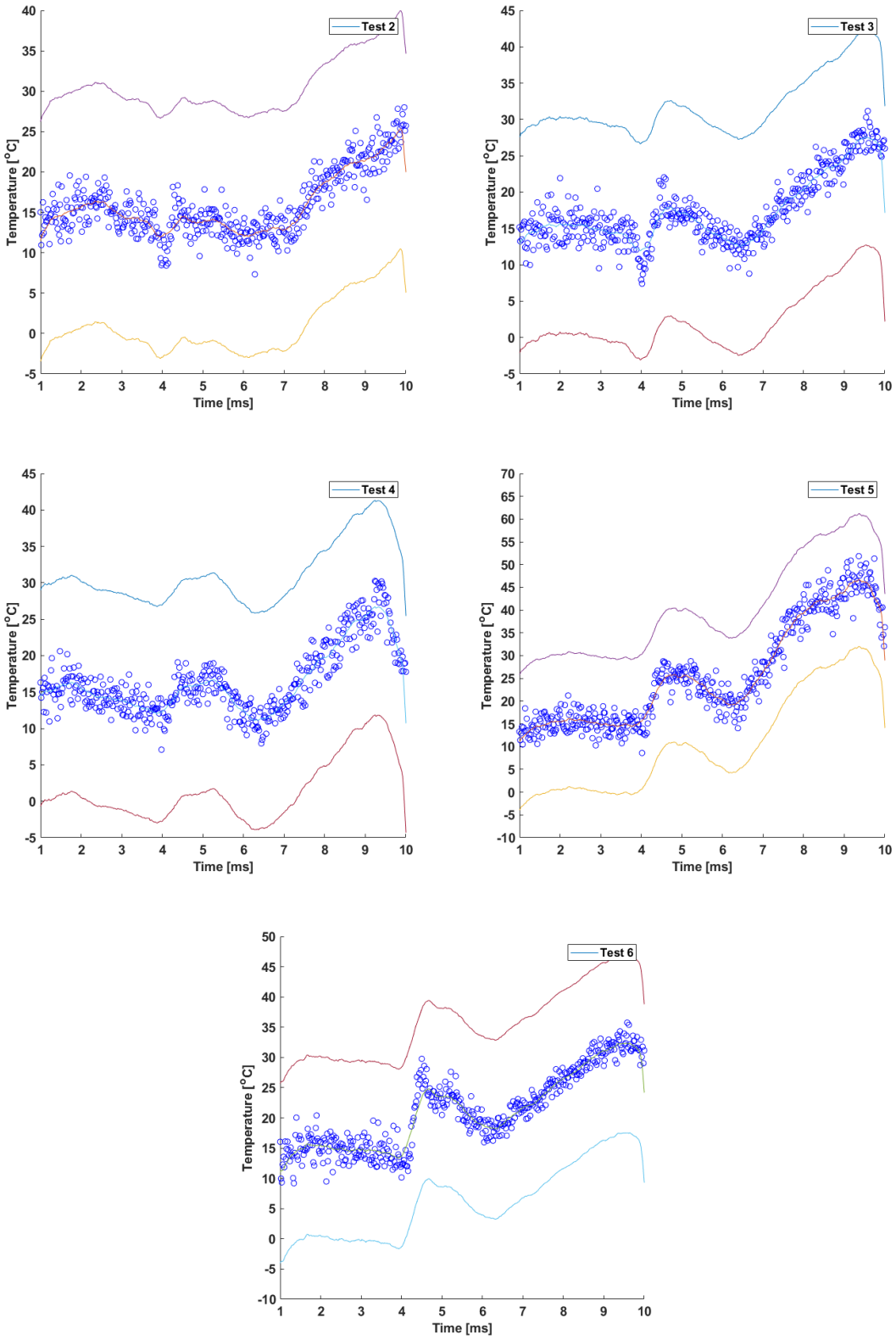

Figure 3.34 Corrected frame-by-frame temperature data for the drop weight impact of the double loading samples

Table 3.4 Change in temperature of the double loading samples for different sections of the impact with the associated actual temperature assuming a start at 15 °C

Test	Initial Heating (Delta T [°C])	Cooling (Delta T [°C])	Secondary Heating (Delta T [°C])
2	-1 (14)	-4 (11)	10 (25)
3	2 (17)	-3 (12)	12 (27)
4	1 (16)	-4 (11)	11 (26)
5	10 (25)	4 (19)	31 (46)
6	9 (24)	3 (18)	17 (32)

Table 3.5 Actual temperatures of the double loading samples for different sections of the impact with the average and standard deviation

Test	Initial Heating (Temperature [°C])	Cooling (Temperature [°C])	Secondary Heating (Temperature [°C])
2	15	12	25
3	18	13	28
4	17	11	27
5	26	19	47
6	25	18	32
Avg	**20.2**	**14.6**	**31.8**
STD	**4.969909**	**3.646917**	**8.871302**

Results for the change in temperature and actual temperature correlations led to similar conclusions. All the tests agreed within one or two degrees of one another. Therefore, for the other tests, all the results will be shown in tables, but only the plots for the actual temperature correlation will be displayed. The results above exhibited an initial average temperature increase to 20.2 °C, a cooling back down to 14.6 °C, and a secondary heating to 31.8 °C. All of the tests for this sample roughly agreed with each other over the three sections of the impact. The only test that deviated greatly from the rest was test 5 because it exhibited a 15 °C increase in the last section of the impact over the next closest test (test 6). However, test 5 did match closely to test 6 over the first two sections. Some of the variation could have been inherent to the setup as seen during the calibration. The greater temperature rise could have also been the result of a change in the sample itself, such as size or thickness, or a faster speed reached by the drop weight because the sample exhibited a higher temperature over the entire impact. Regardless of this one test, the results agreed well with one another in relation to the temperature rises and trends within the double loading sample.

3.6.2 Normal Phosphor Loading

Results for the normal loading samples are shown below in Figure 3.35. Table 3.6 displays the results for the change in temperature and Table 3.7 for the actual temperature.

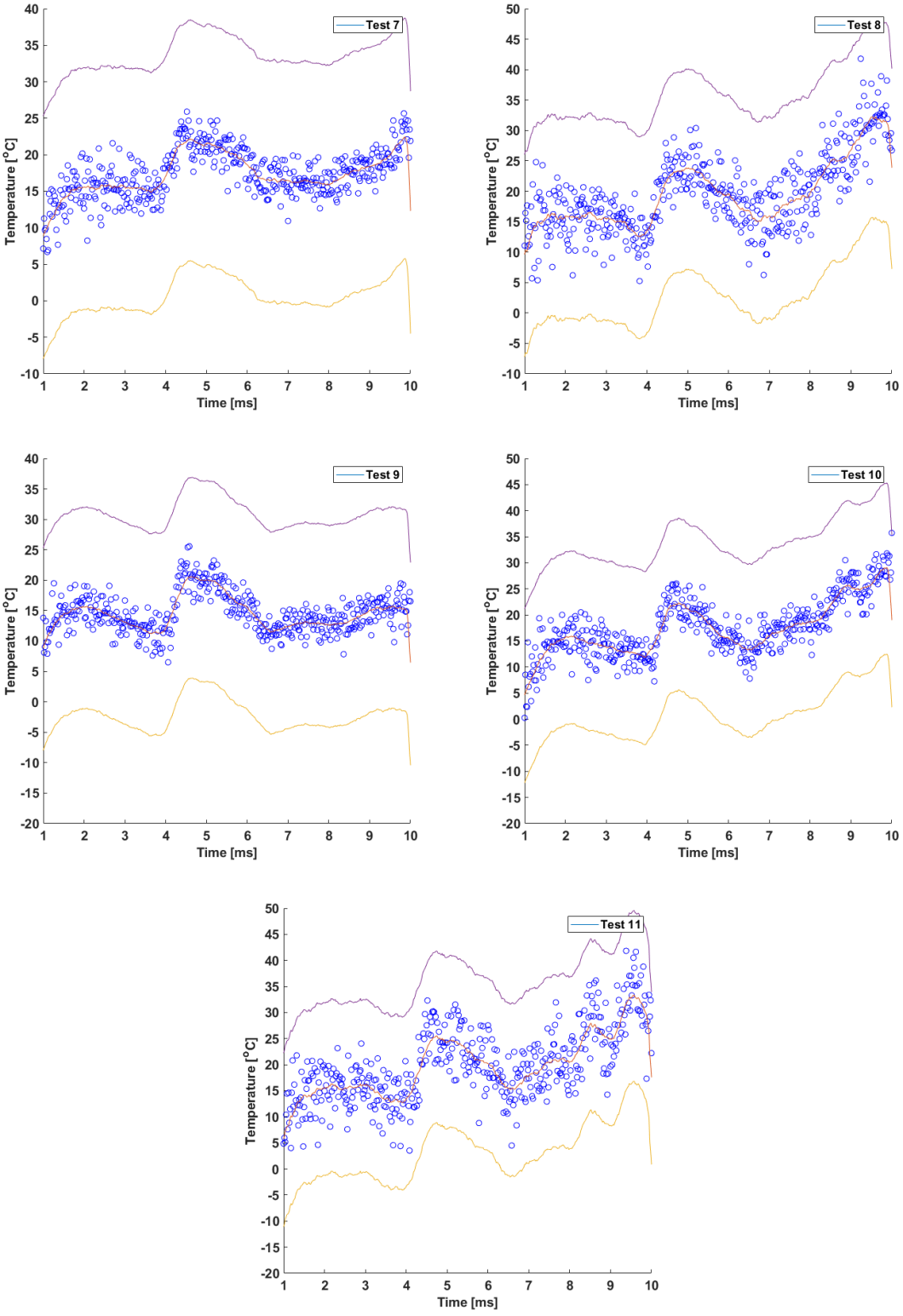

Figure 3.35 Corrected frame-by-frame temperature data for the drop weight impact of the normal loading samples

Table 3.6 Change in temperature of the normal loading samples for different sections of the impact with the associated actual temperature assuming a start at 15 °C

Test	Initial Heating (Delta T [°C])	Cooling (Delta T [°C])	Secondary Heating (Delta T [°C])
7	7 (22)	0 (15)	7 (22)
8	8 (23)	0 (15)	17 (32)
9	5 (20)	-4 (11)	0 (15)
10	7 (22)	-2 (13)	14 (29)
11	10 (25)	0 (15)	18 (33)

Table 3.7 Actual temperatures of the normal loading samples for different sections of the impact with the average and standard deviation

Test	Initial Heating (Temperature [°C])	Cooling (Temperature [°C])	Secondary Heating (Temperature [°C])
7	22	16	22
8	24	15	32
9	20	11	16
10	22	13	29
11	25	15	33
Avg	**22.6**	**14**	**26.4**
STD	**1.949359**	**2**	**7.231874**

As shown in the table above, these samples demonstrated an average initial heating to 22.6 °C, followed by cooling to 14 °C, and then heating again to 26.4 °C. Similar to the double loading sample, the normal loading sample showed good agreement between tests, except on one occasion. Test 9 exhibited similar behavior during the first two sections and then deviated during the secondary heating. While the other tests reached temperatures of around 30 °C, this test only reached 16 °C. Once again, this could have been action inherent to the sample because none of the other tests demonstrated this type of behavior. In general, the majority of the tests exhibited similar action during impact.

3.6.3 Half Phosphor Loading

Final results collected for the half loading sample are shown below in Figure 3.36. As in the prior sections, the numerical results for the change in temperature plot are shown in Table 3.8 with Table 3.9 showing the results for the actual temperature plots.

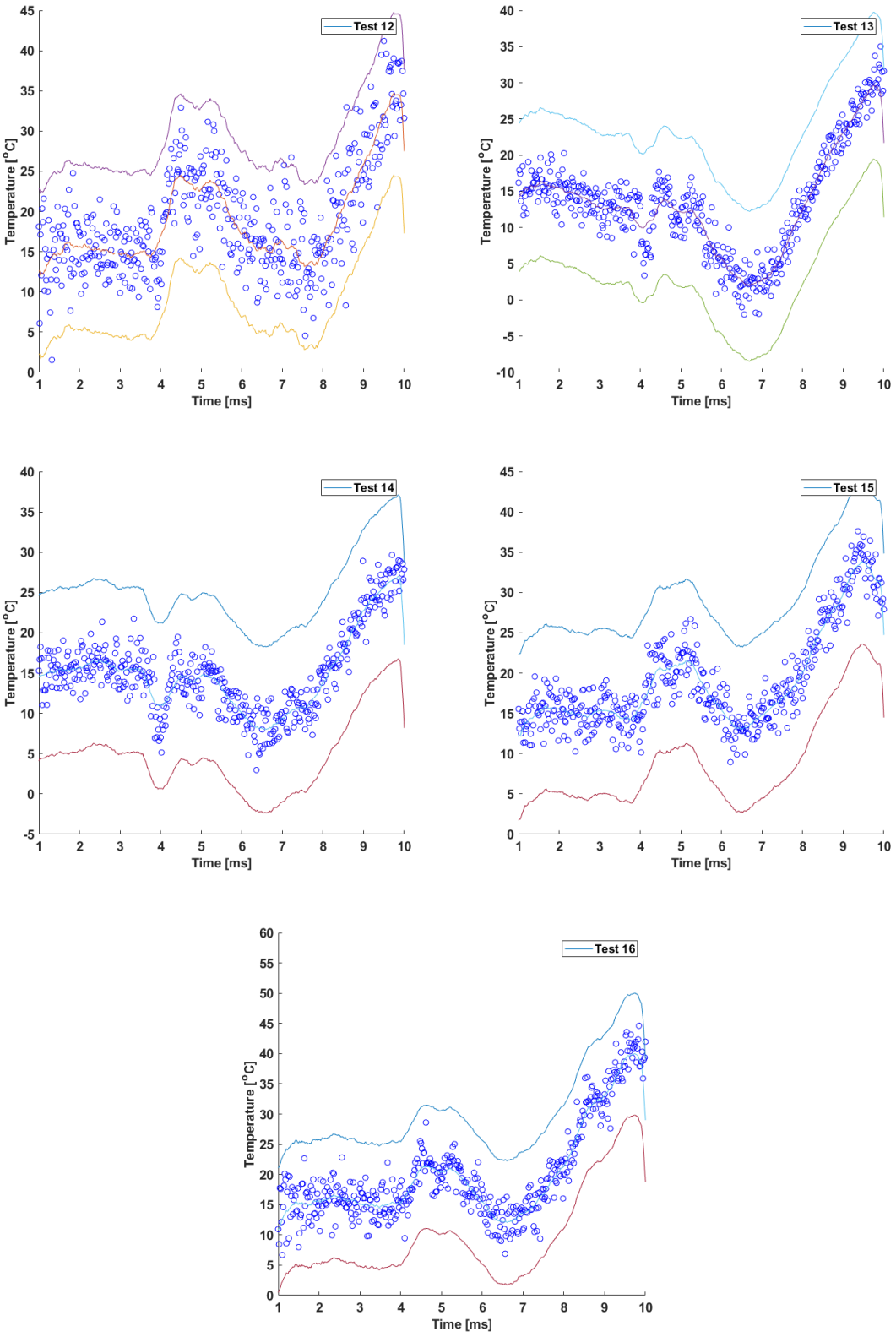

Figure 3.36 Corrected frame-by-frame temperature data for the drop weight impact of the half loading samples

Table 3.8 Change in temperature of the half loading samples for different sections of the impact with the associated actual temperature assuming a start at 15 °C

Test	Initial Heating (Delta T [°C])	Cooling (Delta T [°C])	Secondary Heating (Delta T [°C])
12	9 (24)	-2 (13)	19 (34).
13	-2 (13)	-14 (1)	14 (29)
14	-1 (14)	-7 (8)	11 (26)
15	6 (21)	-2 (13)	18 (33)
16	6 (21)	-3 (12)	24 (39)

Table 3.9 Actual temperatures of the half loading samples for different sections of the impact with the average and standard deviation

Test	Initial Heating (Temperature [°C])	Cooling (Temperature [°C])	Secondary Heating (Temperature [°C])
12	24	13	35
13	14	2	30
14	15	8	27
15	22	13	34
16	21	12	40
Avg	**19.2**	**9.6**	**33.2**
STD	**4.438468**	**4.722288**	**4.969909**

These results displayed an average initial rise to 19.2 °C, a decrease to 9.6 °C, and then an increase in temperature to 33.2 °C. Unlike the other samples, no one test showed a large difference from the other in relation to the final temperature rise. However, test 13 showed a decrease to 2 °C in the cooling section of the impact. While all of the samples showed a degree of cooling of the sample below room temperature, this one test was around 8 °C to 10 °C below the rest of the tests. Its initial and final heating also demonstrated an outcome that was 8 °C to 10 °C below the others. Therefore, this result was most likely caused by the correction methods used rather than something different within the sample itself. This test showed different action from the rest of the tests over its first couple milliseconds of data because it was not exactly horizontal during the first section of data. Action like this made the data difficult to correct because the exact frame that was at room temperature was unknown. Even with this test deviating slightly due to the correction method used, the rest of the results agrees with each other.

3.6.4 Summary

Among each sample, the results showed good agreement in regards to the changes in temperature for each section. Only some variation was seen in a few tests, but even the outlier tests did not show completely different action than the other tests. The only main point of different between tests was the degree of temperature rise, but the same trends were exhibited throughout all tests. One point to mention was that even though some of the temperatures demonstrated a cooling below room temperature that was not believed to actually occur. These deviations below room temperature were either due to variations inherent to the camera and setup or caused by the correction method used. Some of the test showed strange action during the first segment of the data, making it hard to correct to room temperature as the action was not initially horizontal. There was also the presence of a slight dip in some of the data before the first temperature increase, artificially decreasing the temperatures reached. The exact reason for this dip was unknown, but as it did not show up in all of the tests, it was not accounted for in the correction. Therefore, the corrections applied were not perfect for all of the data, but worked for a majority of it. The instanced when the corrections were not as beneficial, the data was exhibiting some type of action that was specific to its test. Whether that was due to variation in the laser pulse or in the sample was not known, but it slightly changed the results of the specific test.

Looking at the average results, the half loading samples were able to reach the highest temperatures after the secondary temperature increase, followed by the double loading sample and the normal loading sample. Based on the calculations conducted prior, the half loading was expected to reach the highest final temperature due to its higher ideal change in temperature. However, the normal loading sample was supposed to be the next highest, and the double loading was supposed to be the lowest. This deviation from the calculations was influenced by the two outliers in the double and normal loading tests mentioned earlier. Those being test 5, which was higher than average, and test 9, which was lower than average. When those two tests were removed from the data set, the normal loading sample had a higher average than the double loading sample, as predicted. Despite these outliers, none of the tests came close to exceeding the calculated temperature increase, which was appropriate since the calculated temperature change was the maximum and ideal case.

Over the first two sections, the temperatures reached tended to agree between the different samples, except for the cooling section of the half solids loading sample. On average, this one

reached substantially lower temperatures than the rest, but this was once again mainly due to the action of an outlier that was far below the rest. As discussed before, the middle section in test 13 reached 2 C, which was far below the average. Therefore, other than this point, the data tended to agree with the temperatures reached for the other two solids loadings within 1 or 2 °C.

The last observation within this data was that the tests with the normal and half loading samples varied more from frame to frame than the double loading sample. This can be seen in the double loading sample having a much smoother trend in its tests. While the normal and half loading samples do exhibit the same trend, their trend was generally choppier than the double loading sample. This could be the result of a greater particle dispersion in the sample that also led to the laser burst profile having a greater influence over the data, as mentioned in the calibration section earlier. Despite the variation present, the data points fell within the 95% confidence interval as determined from the calibration.

Despite some slight differences within the result of the data, all of the solids loadings showed the ability to determine the temperature of the impact event. All samples demonstrated the same trend in the data, along with similar temperatures reached, usually agreeing within a few degrees of each other. Therefore, when used with the intensity ratio method, ZnO:Ga embedded samples are able to be employed to detect high-speed temperature rises during impact. As this was the preliminary investigation into these types of samples, further improvements and research can be conducted to increase the knowledge surrounding these embedded phosphors. A discussion about improvements and areas of future work is presented below.

3.6.5 Improvements

After testing, it was clear that some improvements could be made to the setup and analysis. The first improvement is in relation to what data is collected in the experiment. In order to correct for the laser burst variation in the data, the initial profile taken when no drop occurred was divided out in all of the data. However, there is no guarantee that the laser will remain this way throughout the whole testing. To mitigate the potential error caused by this, a test with no drop could be collected for each sample before its actual drop test. This could correct for the laser burst, but also any possible differences in luminescence between the samples.

Another improvement that could be made is to film the impact from the side, as was done with the 500 kHz tests. Some questions arose in relation to the different parts of the impact being

captured when the timescale of the IR video and action of the ratios did not match. More weight was placed on the ratios because the laser was able to focus on the sample, but an extra camera would allow for imaging of the whole impact sequence from the initiation of impact to when the drop weight comes to a rest. Then, syncing the two cameras would allow for a certain temperature to be correlated to a specific part of the collision. Adding this camera to the setup would allow for more data to be extracted from the impact, fixing the disparity between the collected ratios and the IR video. Overall, this would allow for a more detailed explanation of the heat transfer process occurring within the sample.

4. CONCLUSION

Within this research, three different solids loading of ZnO:Ga embedded in a sylgard binder were evaluated for use during high-speed impacts. To measure the temperature of impact in a drop weight apparatus, the intensity ratio method was employed with two different filter sets. A/D and E/D filter sets were the most sensitive combinations near room temperature with A being 373-387 nm, D being 415-455 nm, and E being 394-406 nm. Due to the short lifetime of the phosphor, high repetition rates were able to be implemented, starting with 500 kHz. After an initial calibration that demonstrated a trend with temperature in the data, the drop tests were performed. However, at repetition rates this high, combined with the imprecise timing of the drop weight, these tests provided no consistent data from which conclusions could be draw about the drop weight.

With these high repetition rate tests proving unreliable, the repetition rate was decreased to 50 kHz. At this repetition rate, the entire impact was able to be imaged, resulting in the collection of useful information. After another calibration, drop tests were again conducted for the ZnO:Ga samples. Some data correction was required once it was collected, but these tests showed the impact presented in three distinct section. There was an initial heating of the sample from the first impact of the drop weight on the sample, a cooling stage where the energy was being put towards deformation of the sample rather than heating, and then a final temperature rise where the sample was fully compressed and temperature was able to increase again until the impact was complete. All three solids loadings demonstrated this trend with each achieving similar temperature increases. Starting at 15 °C, the first heating stage was accompanied by an average temperature increase to 19.2 °C-22.6 °C, followed by the cooling stage reaching 9.6 °C-14.6 °C, and then a final heating to between 26.4 °C and 33.2 °C. Some of the data was slightly skewed in the second stage, resulting in temperatures below room temperature, but most likely the sample came back to room temperature at the point and not below. Even with that slight skew in results, all three solids loadings demonstrated similar trends in results with temperature agreement within a few degrees of one another. Therefore, all three solids loadings samples exhibited the ability of embedded ZnO:Ga to make high-speed temperature measurements during impact, using the intensity ratio method.

5. FUTURE WORK

While performing this analysis for ZnO:Ga, there are a few more areas that could be analyzed within the samples to provide further insight into its application to impact studies. These variation include alterations to the experimental setup or the samples themselves.

5.1 Fluence Variations

One variable of interest for future testing would be the laser fluence. This variable involves the size of the laser pulse that is exciting the sample. The smaller the fluence, the more the laser energy is localized. This was seen to possibly have an influence on the absolute ratio obtained during the analysis of the data, but it was able to be corrected through dividing by the room temperature ratio. However, varying the fluence could develop further knowledge about the interaction of the phosphor particles within the sylgard binder. As was seen in the testing above, calibration at the same fluence caused the double loading samples to form larger ratios. This could be because of the increased solids loading of the phosphors resulting in more signal being produced. The variable to interest would be how adjusting the fluence would influence all of the samples. Another question would be whether there exists one ideal laser fluence for each individual solids loading to obtain the most sensitive temperature correlation.

5.2 Sample Size and Thickness

Another important variable to isolate in these experiments would be the sample characteristics, such as size and thickness. During the above experiments, the samples were all kept roughly the same size and shape. However, because they were cut by hand, there was some degree of variation between each sample. This could be the cause of some of the differences in temperature rise within the samples. Not only was there possible size variations, but also the thickness could vary slightly from sample to sample. These were not extreme variations, but when dealing with temperature change of a few degrees, every small variation could influence the final result. Therefore, to ensure that the sample geometry does not have influence over the final result, a specific mold could be created for the samples. This was they are all the same geometry and thickness, eliminating this factor. Additionally, the sample geometry could be altered to see how

making a smaller, thinner sample impacts the temperature readings. Similar to coating thickness, an ideal sample size and thickness could be determined to increase the signal and therefore the accuracy of the temperature readings.

5.3 Binder Variation

In relation to changes to the sample, not only could the sample geometry be changed, but also the binder material within the sample. During his research, Jason Wickham studied the role that elastic modulus and work of adhesion had on the sensitivity of plastic bonded explosives [24]. This research found that decreasing the elastic modulus of the binder had a correlation to a decrease in the impact sensitivity of the samples [24]. Since the binder elastic modulus had a noticeable impact on the sensitivity of the explosive samples, this could potentially be seen within the temperature readings. A higher elastic modulus results in a stiffer material, therefore, more of the energy would go towards heating the object, rather than its deformation. Much of the energy was most likely lost in the deformation of the sylgard samples in the above experiments, resulting in a lower temperature rise than the ideal case. Due to the elastic modulus already demonstrating a clear influence over the impact sensitivity of an explosive sample, it would be of interest to see if the temperature rise is influenced in a similar way.

5.4 Energetic Material Addition

While altering sample size and thickness would be beneficial to determine their influence on the temperature increase, another sample variation that could be made would be to add some energetic material to the sample. Similar to what Casey did in his experiment [18], the sample could be imaged to see if it is efficient at tracking hot spot formation. Since the sample would be achieving much higher temperatures with the energetic material, its usefulness over a wider range of temperatures would be able to be determined, as well. Unlike Casey's experiment, the sample would be in impact and not under mechanical vibration, so the action of hot spot formation during impact would be able to be tracked using these samples. The main difference between these two tests would be the timescale. Evolution of the hot spot in Casey's experiment occurred on the order of seconds, while the impact would occur on the order of milliseconds. Therefore, with the addition of an energetic material, the effectiveness of the sample could be determined in relation to its

ability to resolve a hot spot over a short time frame. In addition, further information could be determined about the evolution of a hot spot for an energetic material during impact.

5.5 Repetition Rate

Moving on from alterations to the sample, the repetition rate could also be varied during testing to determine if it has any influence on the temperature correlation. With ZnO:Ga having such a short lifetime, on the order of nanoseconds, the repetition rates would be able to be increased without worry about the sample being excited repeatedly before its complete decay. This way it could be determined whether the repetition rate used on the sample had any influence over its calibration behavior. Calibrating at different repetition rates would also allow for testing at these rates. However, timing would need drastic improvements when increasing the repetition rate in order to confirm the part of the impact event being imaged. Increasing the repetition rate could allow for more details about specific parts of the impact event. Conversely, not only could the repetition rate be increased, but it could also be further decreased to attempt and image more of the impact event, based on a longer burst. This way the laser could be triggered much sooner to record the baseline action of the sample, then the impact could be captured, along with the decrease in temperature after the impact event. Overall, the entire action of the impact event could be captured, including the action of the sample before and after impact. Being able to alter the repetition rate in such a way is an advantage of having a phosphor with such a short lifetime.

5.6 Kolsky Bar Measurements

One of the last alterations that can be made to this experimental setup would be the substitution of the drop weight apparatus for the Kolsky bar. While the drop weight was simple, the Kolsky bar allows for much more control of the impact. In addition, the Kosky bar can provide more detail about the impact event itself through its data acquisition devices. Different strain rates could be tests with a variety of samples to better characterize them. The Kolsky bar could be used in conjunction with some of the other alterations above to add to the information about the samples. However, the bar will require some adjustment to accommodate the softer sylgard samples. This would include some, if not all, of the alterations mentioned in the introduction. Once the Kolksy bar is properly set up to accommodate a softer sample, the data collected would also provide

information about how the temperature changes within the sample from a side view. With the drop weight apparatus, the bottom face of the sample was able to be imaged, therefore, the temperature change on the underside of the sample was able to be imaged. This temperature was the final temperature after the heat was conducted through the sample, causing this temperature to be smaller than on the side in contact with the drop weight apparatus. A side view of the sample would allow viewing of the whole sample at once, developing some insight on the change in temperature from one side of the sample to the other. This would provide much more detail about the samples themselves based on how the temperature changes from the impact area through the sample.

REFERENCES

[1] Nie, Y.. *Dynamic Deformation and Temperature Field Measurement of Metallic Materials*. 1, Purdue University Graduate School, 22 Nov. 2019, doi:10.25394/PGS.10711244.v1.

[2] Brübach, Jan, et al. "On surface temperature measurements with thermographic phosphors: a review." *Progress in Energy and Combustion Science* 39.1 (2013): 37-60.

[3] Aldén, Marcus, et al. "Thermographic phosphors for thermometry: a survey of combustion applications." *Progress in energy and combustion science* 37.4 (2011): 422-461.

[4] Khalid, Ashiq Hussain, and Konstantinos Kontis. "Thermographic phosphors for high temperature measurements: principles, current state of the art and recent applications." *Sensors* 8.9 (2008): 5673-5744.

[5] Allison, S. W., and G. T. Gillies. "Remote thermometry with thermographic phosphors: Instrumentation and applications." *Review of Scientific Instruments* 68.7 (1997): 2615-2650.

[6] Abram, Christopher, et al. "High-speed planar thermometry and velocimetry using thermographic phosphor particles." *Applied Physics B* 111.2 (2013): 155-160.

[7] Särner, Gustaf, Mattias Richter, and Marcus Aldén. "Investigations of blue emitting phosphors for thermometry." *Measurement Science and Technology* 19.12 (2008): 125304.

[8] Jaque, Daniel, and Fiorenzo Vetrone. "Luminescence nanothermometry." *Nanoscale* 4.15 (2012): 4301-4326.

[9] Ranson, R. M., C. B. Thomas, and M. R. Craven. "A thin film coating for phosphor thermography." *Measurement science and Technology* 9.12 (1998): 1947.

[10] Allison, S. W., et al. "Nanoscale thermometry via the fluorescence of YAG: Ce phosphor particles: measurements from 7 to 77 C." *Nanotechnology* 14.8 (2003): 859.

[11] Glais, E., et al. "Luminescence properties of ZnGa 2 O 4: Cr 3+, Bi 3+ nanophosphors for thermometry applications." *RSC Advances* 8.73 (2018): 41767-41774.

[12] Zhou, Yonghui, Jun Lin, and Shubin Wang. "Energy transfer and upconversion luminescence properties of Y2O3: Sm and Gd2O3: Sm phosphors." *Journal of Solid State Chemistry* 171.1-2 (2003): 391-395.

[13] Chong, Joo-Yun, et al. "Co-precipitation synthesis of YAG: Dy nanophosphor and its thermometric properties." *Journal of alloys and compounds* 581 (2013): 484-487.

[14] Vu, Nguyen, et al. "Photoluminescence and cathodoluminescence properties of Y2O3: Eu nanophosphors prepared by combustion synthesis." *Journal of Luminescence* 122 (2007): 776-779.

[15] Sharma, Prashant K., Ranu K. Dutta, and Avinash C. Pandey. "Performance of YAG: Eu 3+, YAG: Tb 3+ and BAM: Eu 2+ plasma display nanophosphors." *Journal of Nanoparticle Research* 14.3 (2012): 1-9.

[16] Pandey, A., et al. "Thermoluminescence properties of nanocrystalline K2Ca2 (SO4) 3: Eu irradiated with gamma rays and proton beam." *Nuclear Instruments and Methods in Physics Research Section B: Beam Interactions with Materials and Atoms* 269.3 (2011): 216-222.

[17] Sahoo, Subhanarayan, et al. "Frequency and temperature dependent electrical characteristics of CaTiO 3 nano-ceramic prepared by high-energy ball milling." *Journal of Advanced Ceramics* 2.3 (2013): 291-300.

[18] Casey, Alex D., et al. "Dynamic imaging of the temperature field within an energetic composite using phosphor thermography." *Applied optics* 58.16 (2019): 4320-4325.

[19] Chen, Weinong W., and Bo Song. *Split Hopkinson (Kolsky) bar: design, testing and applications*. Springer Science & Business Media, 2010.

[20] Song, Bo, and Weinong Chen. "Split Hopkinson pressure bar techniques for characterizing soft materials." *Latin American Journal of Solids and Structures* 2.2 (2005): 113-152.

[21] Stevens, Ralph Robert. *Modeling of Sylgard adhesive strength*. No. LA-UR-15-20757. Los Alamos National Lab.(LANL), Los Alamos, NM (United States), 2015.

[22] "Standard Thermodynamic Properties of Chemical Substances," in CRC Handbook of Chemistry and Physics, 101st Edition (Internet Version 2020), John R. Rumble, ed., CRC Press/Taylor & Francis, Boca Raton, FL.

[23] "Physical Constants of Inorganic Compounds," in CRC Handbook of Chemistry and Physics, 101st Edition (Internet Version 2020), John R. Rumble, ed., CRC Press/Taylor & Francis, Boca Raton, FL.

[24] Wickham, J. A., S. P. Beaudoin, and S. F. Son. "The role of adhesion and binder stiffness in the impact sensitivity of cast composite energetic materials." *Journal of Applied Physics* 128.21 (2020): 214902.